UNIVERSIDAD NACIONAL AUTÓNOMA DE MÉXICO

POSGRADO EN CIENCIA E INGENIERÍA DE MATERIALES
CENTRO DE FÍSICA APLICADA Y TECNOLOGÍA AVANZADA

"PHYSICOCHEMICAL CHANGES OF HYDROXYAPATITE FROM BOVINE BONES DURING CONTROLLED CALCINATION PROCESSES"

TESIS
QUE PARA OPTAR EL GRADO DE:
DOCTORA EN CIENCIA E INGENIERÍA DE MATERIALES

PRESENTA
M. en C. SANDRA MILENA LONDOÑO RESTREPO

TUTOR
Dr. Mario Enrique Rodríguez García
Centro de Física Aplicada y Tecnología Avanzada, UNAM

MIEMBROS DEL COMITÉ TUTOR
Dr. Eric Mauricio Rivera Muñoz
Centro de Física Aplicada y Tecnología Avanzada, UNAM

Dra. María de los Ángeles Aguilera Barreiro
Facultad de Ciencias Naturales, UAQ

MÉXICO, FEBRERO DE 2020

AKNOWLEDGMENTS

I wish to express my sense of gratitude and indebtedness to my tutor, Dr. Mario E. Rodríguez García who has led this research and, by the way, has taught me not only how being a researcher, but also how being a better person.

I want to express my gratitude to the committee members, Dr. Eric Mauricio Rivera Muñoz and Dra. María de los Ángeles Aguilera Barreiro for their valuable suggestions that improve this work. I would like to thank the jury members of this thesis: Dra. Beatriz Marcela Millán Malo, Dr. Julio Gregorio Mendoza Álvarez, Dr. Mario Enrique Rodríguez García, Dr. Rafael Ramírez Bon, and Dra. Criseida Ruiz Aguilar for generously offering their time, support, guidance, and goodwill throughout the review of this document.

I am also thankful for Consejo Nacional de Ciencia y Tecnología (CONACyT) for the financial support for my Ph.D. thesis (Scholarship No. 433379); Programa de Apoyo a Proyectos de Investigación e Innovación Tecnológica (PAPIIT; Project No. IN112317), Programa de Apoyo a los Estudios de Posgrado (PAEP), and SEP-CONACyT (A1-S-8979) for the financial support.

I am so thankful to Mexico, Universidad Nacional Autónoma de México (UNAM), and Centro de Física Aplicada y Tecnología Avanzada (CFATA) for the chance they gave me to improve my knowledge by doing postgraduate studies, and thanks a lot to Dr. José Luis Aragón Vera for his magnificent management as director of CFATA. Thanks to M. en IQ. Alicia del Real López, Dra. Beatriz Marcela Millán Malo, Dra. Antonieta Mondragón Sosa, Dra. Carmen Leticia Peza Ledesma, and M. Carolina Muñoz for the technical support.

I feel a deep sense of gratitude for my parents María Giomar Restrepo Rivera and Walter Londoño Cárdenas, who have supported me every day of my life. I could not have better ones than them.

Last but not least, to my friends and laboratory coworkers who have extended all sorts of help for accomplishing this undertaking, especially to my academic brother and dear friend Dr. Cristian Felipe Ramírez Gutiérrez.

*-To my lovely **parents** for accepting the painful sacrifice of distance…*

"If we wait until we're ready, we'll be waiting for the rest of our lives."

— Lemony Snicket, The Ersatz Elevator

ABSTRACT

Hydroxyapatite is one of the most ceramic materials used for promoting bone regeneration when is required. Although there are a bunch of synthesis routes, no one has managed to have similar properties like human hydroxyapatite. The best way to obtain it is by obtaining from mammalian bones, but this method commonly involves calcination processes that modify the physicochemical properties of hydroxyapatite.

This work followed as a continuation of the research made during master in which the effect of low heating rates on physicochemical properties of hydroxyapatite was evaluated (Londoño-Restrepo *et al.*, 2016). This second part aimed to determine the same effect but now for high heating rates (7.4, 9, and 11.1 °C/min); however, a more in-depth analysis was necessary to explain the hydroxyapatite behavior during calcination.

In this way, the effect of the high heating rates on the physicochemical properties (Chapter 4) was complemented with the study of the trabecular bone (Chapter 5), the effect of the crystallite size on X-ray diffraction patterns (Chapter 6) and Raman e infrared spectra (Chapter 7). Finally, in-situ analysis of three heating rates (Chapter 8) was carried out but now considering the aforementioned effects.

The used techniques were X-ray diffraction, High-Temperature X-ray diffraction (HT-XRD), scanning electron microscopy (SEM), High-Resolution scanning electron microscopy (HR-SEM), High-Resolution transmission electron microscopy (HR-TEM), inductively coupled plasma-optical emission spectroscopy (ICP-OES), infrared and Raman spectroscopies, differential scanning calorimetry (DSC), and Thermogravimetric analysis (TGA).

This work provides a new interpretation of physicochemical properties of calcined and no calcined hydroxyapatite from mammalian bones, mainly those belonging to cattle, but also some results were correlated to porcine and human bones. Calcination process involves several changes in hydroxyapatite; therefore, choosing the thermal profile of the process is imperative to guarantee the complete organic phase removal but avoiding the loss of tertiary porosity because of crystal growth and morphological changes. Although calcinations until 1400 °C are commonly reported, the dehydroxylation process starts around 900 °C, in which hydroxyapatite turns into a mix of calcium phosphates; thus, it is not recommended reaching that temperatures. Even though calcination at 900 °C assures complete phase removal, at this temperature, tertiary porosity is lost and MgO is formed; thus, this temperature is neither recommended. There is a narrow range of temperatures in which there is only hydroxyapatite and its tertiary porosity is still present: 540-700 °C.

CONTENT

TABLE OF FIGURES

LIST OF TABLES

CHAPTER 1

INTRODUCTION

It is well known that many countries as Mexico have serious problems associated to illnesses, disorders, and traumatisms which affect the musculoskeletal system that generates disability because of their magnitude and transcendence (Punnett & Wegman 2004; Clark *et al.*, 2018). Although these are evident public health problems, there is a lack of prevention, diagnosis, treatment, rehabilitation, and corrective actions. Until now, Ti-Co-Ni and Fe-Cr alloys are commonly used for bone substitution and repairing due to their mechanical properties, but undesirable effects are present by host tissue. Therefore, metallic alloys must be coated with bioactive materials as hydroxyapatite (HAp) is. That is why tissue engineering research has focused on biocompatible ceramic materials.

HAp plays a crucial role in this problem since it promotes guided bone regeneration (GBR) which is one of the most effective processes for repairing bone structures that have been lost because of the above-mentioned reasons. Regarding dental field, health bone is created through GBR to fill bone periodontal bone defects or having suitable alveolar processes for dental implants applications. In Mexico, hydroxyapatite is also widely used as filling material after enucleation of oral or facial bones tumors, dentofacial and craniofacial trauma, cleft palate, and congenic oral and facial deformations (Aldazábal Martínez *et al.*, 2013). Nevertheless, Mexico has a strong dependence on foreign countries for HAp importing which increases costs and most of the Mexican people cannot obtain it.

Hydroxyapatite (HAp) is a widely used ceramic material in the medical field due to its compatibility with living human tissue and because of it is the main inorganic material in human bones, teeth, and dentine. Synthetic HAp has a general chemical formula $Ca_5(PO_4)_3OH$ whose Ca/P atomic ratio is 1.67; it is not only used in the medical field but also for chromatography and catalysis (Siano *et al.*, 2018; Usami *et al.*, 2019). Synthesizing is not the single route to obtain HAp but also obtaining from biowaste as eggshells, corals, fishbones, mammalian bones, and whatever calcium and phosphorous source in nature (Sadat-Shojai *et al.*, 2013; Akram *et al.*, 2014). HAps obtained from biogenic sources are commonly known as biogenic hydroxyapatites or BIO-HAps, and those from mammalian bones are growing in interest since whose stoichiometry proportion is lost due to the presence of replacement ions as Na, Mg, K, Zn, Si, among others (Giraldo-Betancur *et al.*, 2013; Londoño-Restrepo *et al.*, 2016).

Although there are an enormous amount of methodologies reports for BIO-HAps obtaining, the most used is by calcination, but the thermal history hardly ever is reported. Physicochemical properties of BIO-HAp obtained by this method strongly depend on the thermal variables that must be controlled: heating rate, annealing temperature, sintering time, and heating rate. In most cases, some fixed thermal parameters are reported, but a systematic study of the influence of them on the physicochemical properties of the material has not been done. Moreover, commercial HAp and BIO-HAp have been designed and fabricated based on erroneous premises regarding crystalline quality and crystal size.

During any calcination processes of mammalian bones, adsorption and lattice water are the first mass losses. After that, organic materials (mainly fat and proteins) are degraded. It is well known that calcination also involves crystal growth. In fact, it has been reported crystallite sizes from 10 to 120 nm at 800 °C, but only the annealing temperature was disclosed (Etok *et al.*, 2007). Therefore, a more in-depth research about the effect of the thermal variables on the crystal growth needs to be do.

The aim of this work was to determine the behavior of hydroxyapatite crystals from bovine bones as a function of thermal variables during a calcination process to analyze changes on their physicochemical properties. Bovine cortical bones from femurs were chosen as the source for BIO-HAp obtaining which were subjected to a cleaning protocol for soft tissue and marrow removal. After that, bone powder was acquired by milling using a vibratory disc mill. Finally, an alkaline hydrothermal process to remove the organic matrix that supports HAp crystals into the bone. Systematic calcinations were conducted varying thermal parameters to study their influence on the physicochemical properties of the bovine BIO-HAp. Differential scanning calorimetry (DSC), thermogravimetry (TGA), X-ray diffraction (XRD), high-temperature X-ray diffraction (HT-XRD), scanning electron microscopy (SEM), high-resolution transmission electron microscopy (HR-TEM), and inductively coupled plasma with optical emission spectroscopy (ICP-OES) were the techniques which allowed the comprehension of the BIO-HAp behavior as a function of the thermal variables and clarifying some common misunderstanding regarding BIO-HAp properties before any calcination processes.

To sum up, this research address biogenic hydroxyapatite obtaining with desirable physicochemical properties for clinical applications based on the human hydroxyapatite properties, and some misunderstandings are clarified in this work such as the widely reported poor crystalline quality and the calcinations without considering thermal variables involved in the process.

CHAPTER 2

BIOGENIC HYDROXYAPATITE FROM MAMMALIAN BONES

2.1. Biomaterials

Biomaterials developing is tied to humanity lookout for improving their quality of life and for living longer. European Society for biomaterials defined them as materials intended to interface with biological systems to evaluate, treat, augment or replace any tissue, organ or function of the body during a specified period. Those materials can replace just a section of the human body or being part of an organ system. Biomaterials can be natural or synthetic subject to compliance with specific characteristics as biocompatibility, bioactivity, non-toxicity, and biodegradability. Biocompatibility is referred to be accepted by a living organism without adverse responses by the immune system such as allergic and inflammatory reaction, while biodegradability is concerning to the ease with a substance is degraded by microorganisms under environmental conditions.

Biomaterials were industrial materials which met certain biological acceptance some decades along. Nowadays, most of them are designed and fabricated with specific purposes in the medical field, and more than 50 million people have a prosthesis. These materials are commonly used as replacing materials for broken, diseased, or inexistent organs, e.g., dental prosthesis. They are also used for healing processes, e.g., screws fixed in bones when there is a fracture. Other of their applications is enhancing human functions in which eye lens are a clear example of it. Additionally, biomaterials have been applied for plastic surgery and medical treatments. Applications for biomaterials are commonly grouped according with the body area in which they play a role: skeletal and cardiovascular systems, organs, and senses. Since hydroxyapatite design is the main focus of this work, it is worth mention that it used as filling material because of its poor mechanical properties.

2.2. Skeletal system

Mammalian bones and teeth are composite materials mainly formed by carbonated calcium phosphate crystals which are immersed in an organic matrix which is composed of collagen Type-I, glycoproteins, proteoglycans, sialoproteins, bone cells, and fat. This last phase supports the mineral crystals in which hydroxyapatite is the main component.

The human skeleton has 206 bones that give support to the human body; it means muscles, ligaments, and tissue are joined to them. Skeletal system has mechanical and physiological functions, it protects organs, facilitates movements, produces bone cells, storages triglycerides in yellow marrow, and mineral homeostasis happens there since bones are a pool of them, including Na, Mg, K, Ca, and P. Axial skeleton is formed by skull, vertebral column, and rib cage while appendicular skeleton by bones from shoulder girdle, arms, hands, pelvic girdle, legs, and feet.

2.2.1. Cortical and trabecular bone

Cortical bone

Human cortical bones contain three major anatomical cavities: Haversian/Volkmann canals, osteocyte lacunae, and canaliculi (see Figure 2.1) (Wang & Ni, 2003). Haversian and Volkmann canals are microscopic tubes in the cortical bone where the blood vessels and nerves travel through the bone with many substances such as sugar, amino acids, fatty acids, inorganic compounds, hormones, neurotransmitters, and coenzymes. The porosity due to the Haversian and Volkmann canals is named vascular porosity (VP) and it is the largest one in the cortical bone (Cardoso *et al.*, 2013). These canals are the major contributors to the total porosity. The Haversian and Volkmann canals have communication with bone cells through connections called canaliculi. Osteocytes are the most abundant kind of cells within the bones, which are in the osteocyte lacunae, and from them leave canaliculi in all directions. These canaliculi allow the communication between the lacunae and the central conducts (Haversian canals). It is important to recall that this branched system provides many pathways for the diffusion of oxygen, blood nutrients, and other elements afore mentioned into the extracellular fluid to the osteocytes, and it also allows for the expelling of cellular waste through the blood vessels. At a hierarchical level, cortical bone has three levels of porosity. The first one is due to the Haversian and Volkmann canals or vascular porosity above mentioned. The second porosity is due to osteocyte lacunae and canaliculi called "lacunar-canalicular" porosity (LCP). Finally, the third porosity is the collagen-apatite porosity (CAP) that is the smallest porosity in the cortical bone (Cardoso *et al.*, 2013).

Figure 2.1 shows the anatomical bone cavities before mentioned. The bone surface is dense but, it has micro-holes of about 30 μm in diameter; these holes are Haversian canals which are the central ducts of the bone (see Figure 2.1 A). A longitudinal view of the bone is shown, where it is possible to identify Haversian canals, lacunae, and canaliculi. It is also possible to see a rough surface composed of collagen nanofibers and hydroxyapatite nanocrystals (see Figure 2.1 B). Inside the Haversian canals, it is possible to see the collagen fibers and a lot of canaliculi connecting the Haversian canal with the lacunae (see Figure 2.1 C). As such, it is possible that the hierarchical structure of the bone influences its mechanical and structural properties.

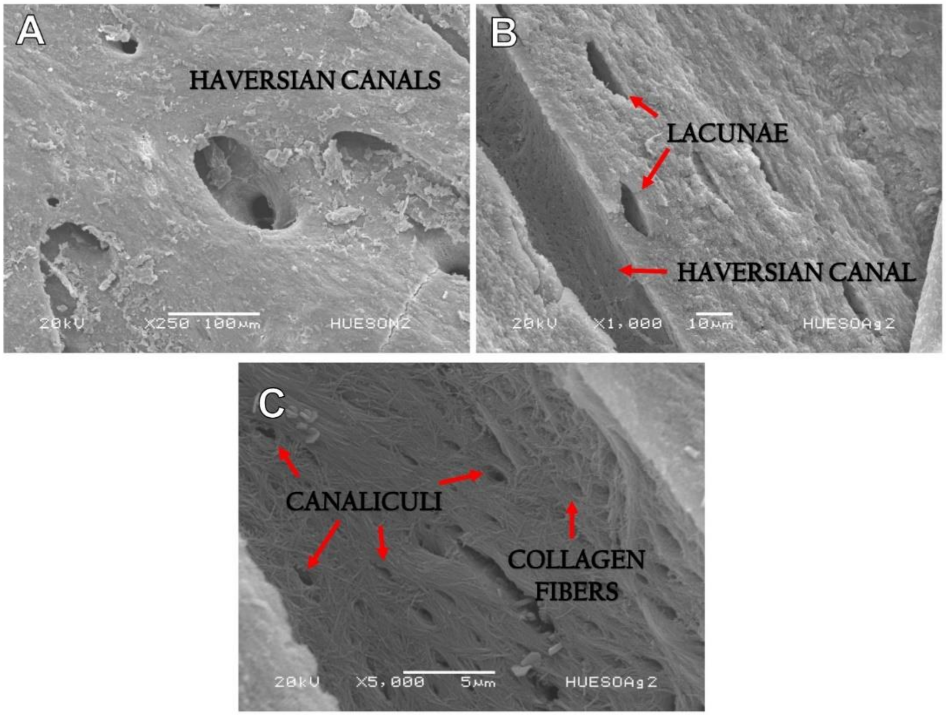

Figure 2. 1 **Bone micro-architecture : primary and secondary porosity.**

Trabecular bone

In large bones like the femur, the trabecular bone is found in the epiphysis and the metaphysis. The femur head distributes the mechanical load to the whole bone, in particular to the cortical region. The mechanical properties of the bone depend on the macro-architecture and crystalline orientation of the trabeculae. It is well known that the spongy bone has higher metabolic activity than the cortical bone, which is one of the reasons to study it in detail. The mechanical resistance is an important parameter to consider for tissue engineering and for clinical applications because this parameter is directly related to the risk of fracture. However, the 3D structure of the natural sponge has not been considered yet.

Wang & Ni (2003) studied human cortical bone porosity and pore size distribution using a low field pulsed NMR approach with human cadaver femurs from donors ranging from 16 to 89 years old. They reported that pore sizes in the bone may be divided into three groups. These three groups have the following porosity ranges 1.3-3%, 4.1-25.5%, and 0.7-9.8%, respectively. They associated the first group with lacunae and the second one with Haversian canals but, they did not associate the third group with anything. According to Rodríguez *et al*., (2011), the porosity increases with the age, which is about 8% for young people and 24-28 % for elderly individuals. Haversian canals tend to increase with age while lacunae porosity decreases. Pore size diameters for Haversian canals vary from 27.1 to 77.5 μm and for lacunae from 3.07 to 4.45 μm. Bone has another porosity associated with trabeculae zone that will be shown in the morphological characterization section. Table 2.1 shows porosities and pore sizes reported in the literature by cortical and trabecular bone; these values can be used as a reference in the case of scaffolds engineering.

Table 2. 1 **Porosities reported for bones.**

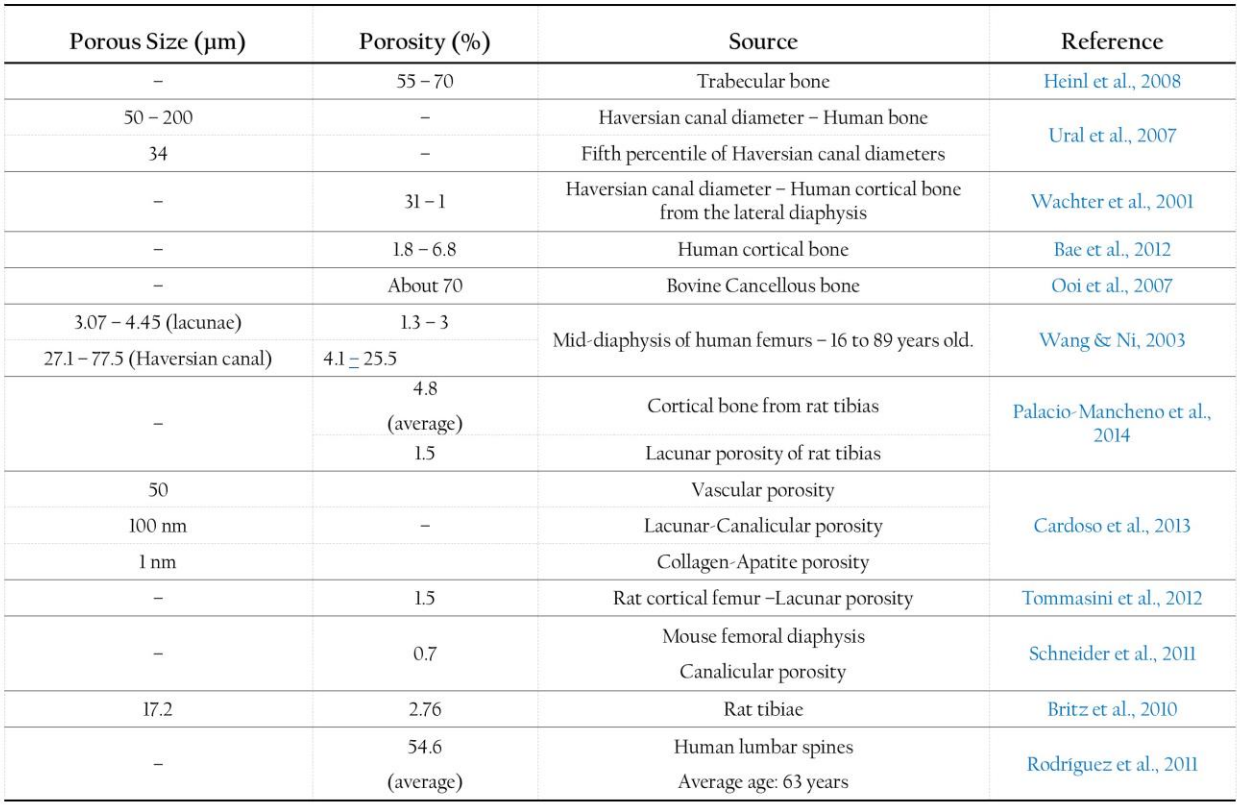

Porous Size (µm)	Porosity (%)	Source	Reference
–	55 – 70	Trabecular bone	Heinl et al., 2008
50 – 200	–	Haversian canal diameter – Human bone	Ural et al., 2007
34	–	Fifth percentile of Haversian canal diameters	
–	31 – 1	Haversian canal diameter – Human cortical bone from the lateral diaphysis	Wachter et al., 2001
–	1.8 – 6.8	Human cortical bone	Bae et al., 2012
–	About 70	Bovine Cancellous bone	Ooi et al., 2007
3.07 – 4.45 (lacunae)	1.3 – 3	Mid-diaphysis of human femurs – 16 to 89 years old.	Wang & Ni, 2003
27.1 – 77.5 (Haversian canal)	4.1 – 25.5		
–	4.8 (average)	Cortical bone from rat tibias	Palacio-Mancheno et al., 2014
	1.5	Lacunar porosity of rat tibias	
50	–	Vascular porosity	Cardoso et al., 2013
100 nm		Lacunar-Canalicular porosity	
1 nm		Collagen-Apatite porosity	
–	1.5	Rat cortical femur –Lacunar porosity	Tommasini et al., 2012
–	0.7	Mouse femoral diaphysis Canalicular porosity	Schneider et al., 2011
17.2	2.76	Rat tibiae	Britz et al., 2010
–	54.6 (average)	Human lumbar spines Average age: 63 years	Rodríguez et al., 2011

2.2.2. Bone composition

Bone tissue is composed of mineral and organic phases, and water. About 10% of the bone tissue is comprised of water. The mineral phase (70%) is mainly composed of carbonated hydroxyapatite (80%), calcium carbonate (15%), other minority phases (5% -dicalcium phosphate, calcium dibasic phosphate, and tricalcium phosphate, among others), and some substitutional ions such as Mg, K, N, among others (Londoño-Restrepo *et al.*, 2018). Collagen type-I (90%), lipids and non-collagen proteins are the main components of the organic phase (20%). Both phases provide strength and resilience to the bone. Hence, the skeleton can absorb impacts without breaking. The minerals are not directly bound to the collagen but rather through non-collagen proteins that provide active sites for mineralization and cell union.

The skeleton is the structural support that protects body organs, and it is a subjection point for muscles. Large bones are associated with high movements such as jumping and running. Large bones as femur are divided into three zones named diaphysis, which is the central one, epiphysis which is the external part of the bone, and finally, the metaphysis that is located between the diaphysis and epiphysis. The most compacted zone of the bone is called cortical bone, and the spongy bone is called trabecular or cancellous bone which is the focus this work.

Hierarchical levels in the bone are designed to do many functions. In the first place, the carbonated hydroxyapatite nanocrystals are aligned into the collagen fibers which are organized in concentric parallels layers named lamellae that are located around the blood vessels forming osteons. The osteons are densely packed forming the compact or cortical bone. Trabecular bone is built by a cancellous network with low bone density (Olszta *et al.*, 2007). The trabecular bone has higher porosity and bigger pore size than cortical bone; the pore size for trabecular bone is in the order of microns to millimeters.

Hydroxyapatite

Hydroxyapatite (HAp) is a mineral that belongs to the apatites family which is a group composed of phosphates, arsenates, and vanadates with hexagonal and pseudo-hexagonal monoclinic structures. "Apatite" is the name of chlorapatite, fluorapatite, and hydroxyapatite, and they exhibit a general formula $A_5(BO_4)_3(OH, F, Cl)$, where A is for metallic cations such as calcium (Ca), Barium (Ba), Sodium (Na), Lead (Pb), among others. While B is for phosphorous (P), Vanadium (V), or arsenic (As) (Gómez Ortega *et al.*, 2004).

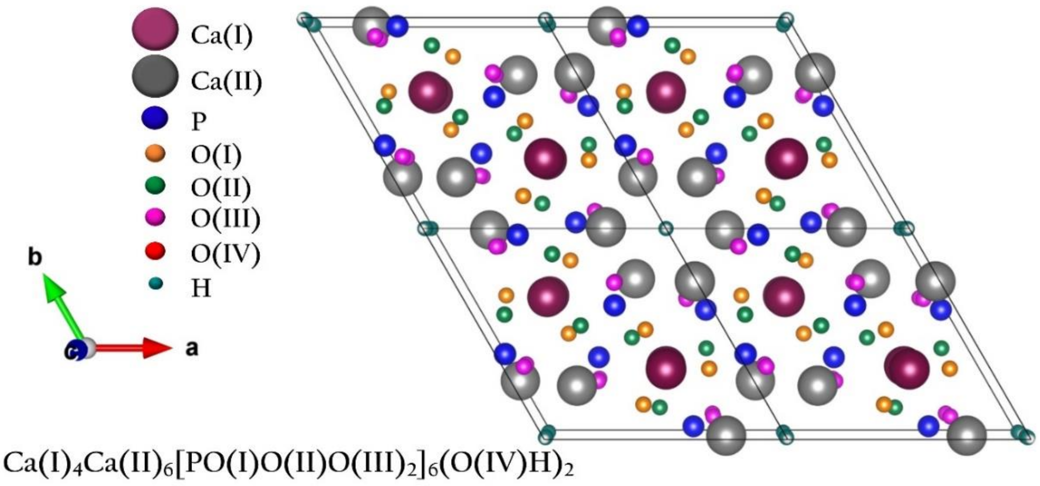

Figure 2. 2 **Crystalline structure of hydroxyapatite.**

Stoichiometric hydroxyapatite has a chemical formula as follows: $Ca_{10}(PO4)_6(OH)_2$ or $Ca_5(PO_4)_3OH$ because in fact, the base of the structure is Z=2, and a Ca/P rate of 1.667, while hydroxyapatite from mammalian bones that is called "Bio-hydroxyapatite" (BIO-HAp) is non-stoichiometric (Giraldo-Betancur *et al.*, 2013), and the Ca/P ratio varies from 1.8 to 3. At crystallographic level, HAp has a compact hexagonal packing with oxygen atoms at tetrahedral and octahedral holes with a spatial group P6₃/m and lattice parameters of $a = b = 9.37$ Å, $c = 6.88$ Å, $\alpha = \beta = 90°$, and $\gamma = 120°$ (Rujitanapanich *et al*., 2014).

The chemical formula for stoichiometric hydroxyapatite is $Ca_{10}(PO_4)_6(OH)_2$ but, to differentiate the structural component of the HAp structure, it is important to rewrite this chemical formula as $Ca(I)_4Ca(II)_6[PO(I)O(II)O(III)_2]_6(O(IV)H)_2$. Regarding hydroxyapatite structure, there are two calcium types as a function of the chemical environment. The notation Ca(I) and Ca(II) indicates Ca atoms type 1 and type 2, respectively. This division in two calcium atoms is due to each one being surrounded by a different number of oxygen atoms in the apatite structure (Figure 2.2). Ca(I) has a 9-coordination number, where all sites are occupied by oxygen atoms, and it results in a tricapped trigonal prism structure. Ca(II) has a 7-coordination number and represents a pentagonal bipyramid (Campa Molina *et al*., 2007). On the other hand, P atoms are surrounded by four oxygens, and they form a tetrahedron structure that is the characteristic structure of the phosphate group (PO_4^{3-}).

Bio-hydroxyapatite

Bio-hydroxyapatite (BIO-HAp) is a non-stoichiometric apatite due to its numerous ionic substitutions, that is obtained from natural sources. Carbonate groups and halogens can replace the phosphate and hydroxyl groups, respectively. The ionic character of hydroxyapatite turns it into a hard, refractory ceramic with a fusion point above 1500 °C; this also allows the partial or complete ionic substitution in the lattice with other ions of similar atomic radio.

BIO-HAp has a lot of medical applications due to its physicochemical properties are similar to human hydroxyapatite, but its applications are limited to direct replacement because it has low mechanical strength. The main uses in this field are as filling material, coating metal prosthesis, maxillofacial surgery, among others, where mechanical strength is not required. This ceramic makes bonds with surrounding bone tissue to promote material integration and growth of new bone tissue.

Nanometric hydroxyapatite (10–100 nm) has better functional properties than HAp with micrometric sizes (>1 μm). Its superficial reactivity and ultra-fine structure, for example, help the interaction tissue-graft when this material is implanted. In addition, nanometric HAp promotes more adherence, mineral deposition, osseointegration, osteoblast differentiation, and proliferation in comparison to micrometric HAp (Nasiri-Tabrizi *et al*., 2014). Pore sizes of at least 50 μm in diameter are required for the replacement parts elaboration to guarantee the fibrovascular tissue penetration, and pores must be interconnected (Thuault *et al*., 2014).

Bone powder is composed of HAp nanometric poly-crystals infused within an organic matrix (fat and protein, see Figure 2.3 A and B). Lipids look like an amorphous coating in the material surface, while protein can be seen as oriented nano-fibrils. When the bone is raw, the organic matrix does not allow viewing the HAp nanocrystals. After a cleaning process, like the hydrothermal treatment that implicates pressure and temperature which was reported by Londoño-Restrepo *et al*. (2016), it is possible to see the HAp crystals in the surface (see Figure 2.3

C and D), but the morphology of the HAp crystals in images taken at 10000X is not well defined yet. In this way, High-Resolution microscopy is needed. When the bone powder with a hydrothermal treatment is calcinated at 600 °C for 50 hours, fat and protein are entirely removed, and in this manner, it is possible to see the micrometric HAp crystals with semi-spherical morphologies (see Figure 2.3 E and F).

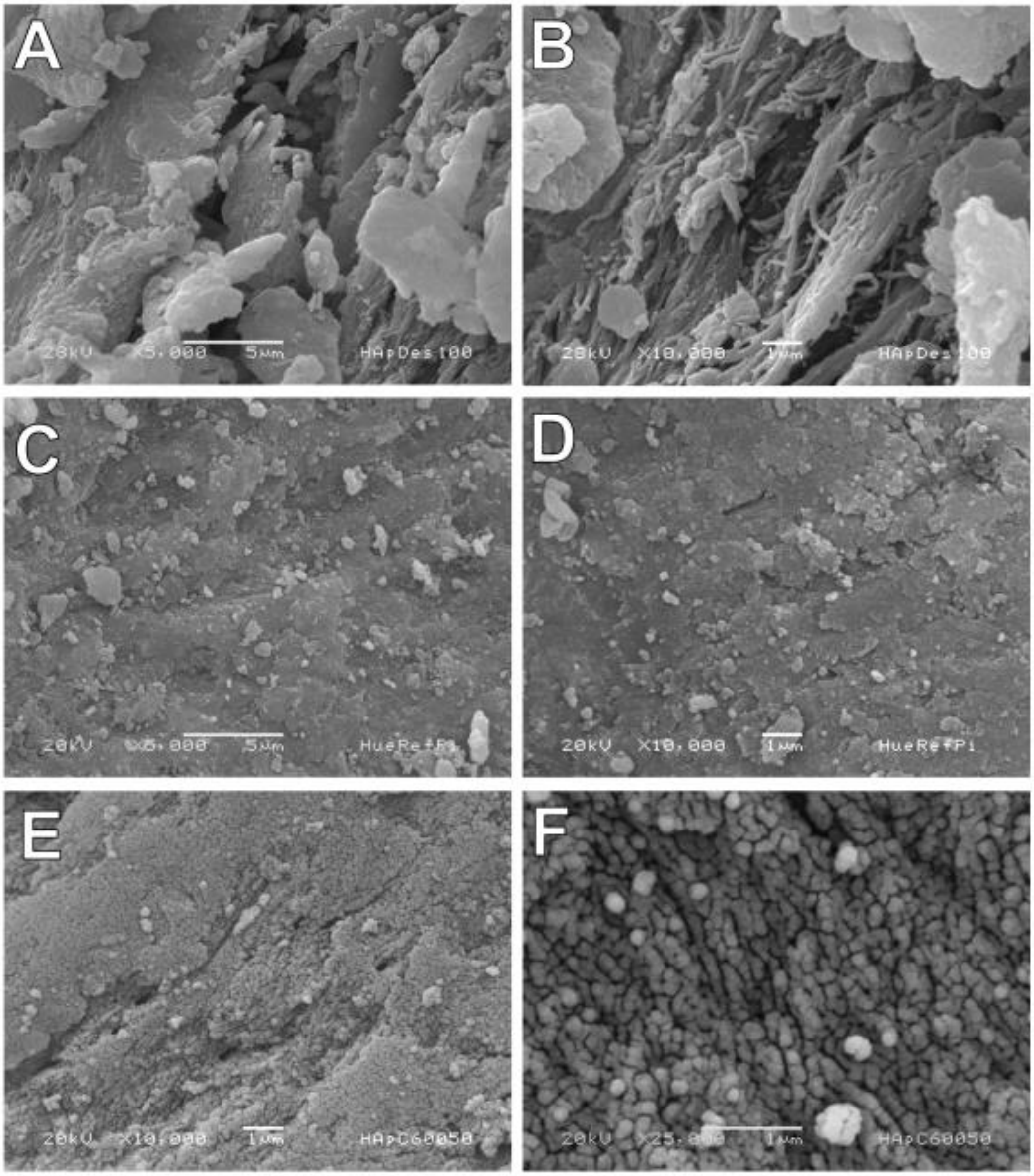

Figure 2. 3 Bovine bone powders: (A) 5,000×, (B) 10,000×. Bovine bone powders with hydrothermal process: (C) 5,000×, (D) 10,000×. Hydroxyapatite from bovine bone: (E) 10,000×, (F) 25,000×.

In natural bones, nano-polycrystalline HAp looks like small clusters that have preferential orientation. It is well known that for temperatures above 750 °C, the HAp polycrystal can be transformed into single crystals through a coalescence phenomenon (Londoño-Restrepo *et al.*, 2018). HAp single crystals have hexagonal and pseudo-hexagonal monoclinic rods-like shapes with micrometric sizes. These rods are obtained to understand the structural properties of the material, but it is known that for medical applications, it is much better to use nano-polycrystalline HAp due to its composition, large reaction surface, and semi-spherical morphology. This last characteristic is important because rod tips damage the bone cells.

The physicochemical properties and extraction efficiency of the BIO-HAp depend on the extraction technique, heating rate, annealing temperature, sintering time, cooling rate, and bone nature (Ramirez-Gutierrez *et al*., 2016). In general, apatite crystals that have been produced by biological systems exhibit crystal sizes less than synthesized HAp crystals.

These characteristics can be readily observed in the trabecular bone, which is an anisotropic percolated macro lattice composed of HAp nanocrystals as will be seen in the morphological characterization section. In an attempt to emulate the cancellous bone, tissue engineering has developed scaffolds from materials like ceramics and polymers. These scaffolds are isotropic macro lattices without preferred structural orientation and micro-porosity. Some properties of the bone have been reported as necessary for an ideal scaffold such as biocompatibility, bioresorbability, mechanical properties, and pore size (Bose *et al*., 2012), but the trabecular bone has other forgotten physicochemical properties such as porosity and interconnectivity, which are necessary too.

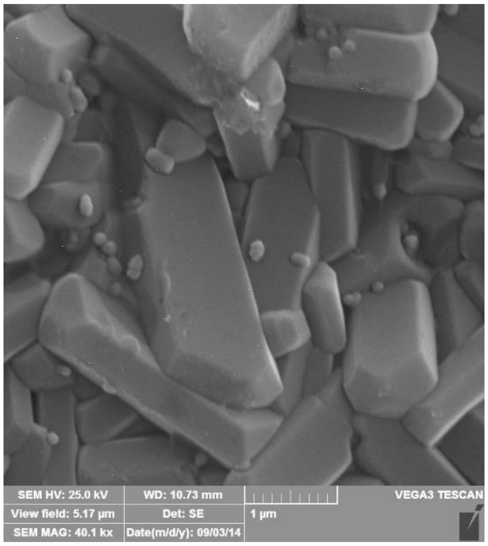

Figure 2. 4 **Hydroxyapatite monocrystals from bovine bone, obtained after calcination at 1000 °C.**

Figure 2.4 shows the characteristic morphology of BIO-HAp single crystals obtained after calcination of bovine bone at 1000 °C. Quasi-hexagonal structures that grew up because of the heating treatment, are present in this image. As it was mentioned before, the BIO-HAp is polycrystalline with nanometric sizes that form a cluster in the bone. This kind of single HAp crystal does not appear in any bone.

- *Structural properties of BIO-HAp*

X-ray diffraction is an excellent technique to identify crystalline structures in any sample and the crystalline percent of a sample when it has micrometric sizes. Bio hydroxyapatite obtained by calcination of bovine cortical bone at 1000 °C (BIO-HAp-1000) was achieved by using the cortical bone of the same femur, and it was used as a reference for X-ray and Raman experiments (Ramirez-Gutierrez *et al.*, 2016). Figure 2.5 A shows the X-ray diffraction pattern of this sample; the red lines correspond to the identification of HA using the ICDD card No. 00-009-0432. These narrow peaks are characteristic of BIO-HAp micro crystals. Figure 2.5 B shows the SEM image of BIO-HAp single crystals where the presence of hexagonal structures and another minority phase like spheres has been identified as magnesium oxide (MgO) is clear (Ramirez-Gutierrez *et al.*, 2017).

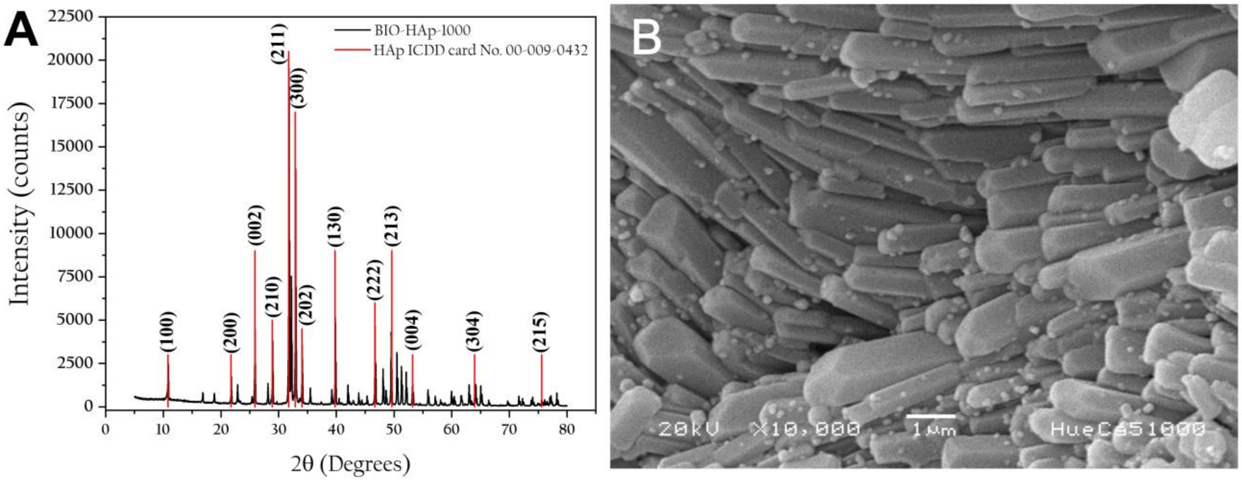

Figure 2. 5 (A) X-ray diffraction pattern of BIO-HAp single crystals. (B) BIO-HAp single crystals.

It is important to point out the differences between crystalline percentage and crystalline quality. The crystalline percentage is defined as:

$$\%C = \frac{C_A}{TA-N} \qquad \text{Eq. 2.1}$$

Where %C is the crystalline percentage, C_A is the crystalline area under the pattern, N is the characteristic electronic noise of the system, and T_A is the total area. Here, it is important to recall that to determine this parameter, it is necessary to take into account the complete diffractogram. Giraldo-Betancur *et al.* (2013) studied the crystalline percentage of commercial BIO-HAp used as medical implants, and this parameter changed from 60 to 80 %.

Crystalline quality (CQ) is commonly calculated by studying the Full Width at the Haft Maximum (FWHM) of any characteristic peak. The most intense peak is usually used for this calculation, but any peak can be characterized. If the FWHM increases, it is an indication that the

CQ decreases and vice versa. The CQ of the bone can be obtained by using the inverse of the FWHM value. However, considerations regarding crystallite size are not taken into account.

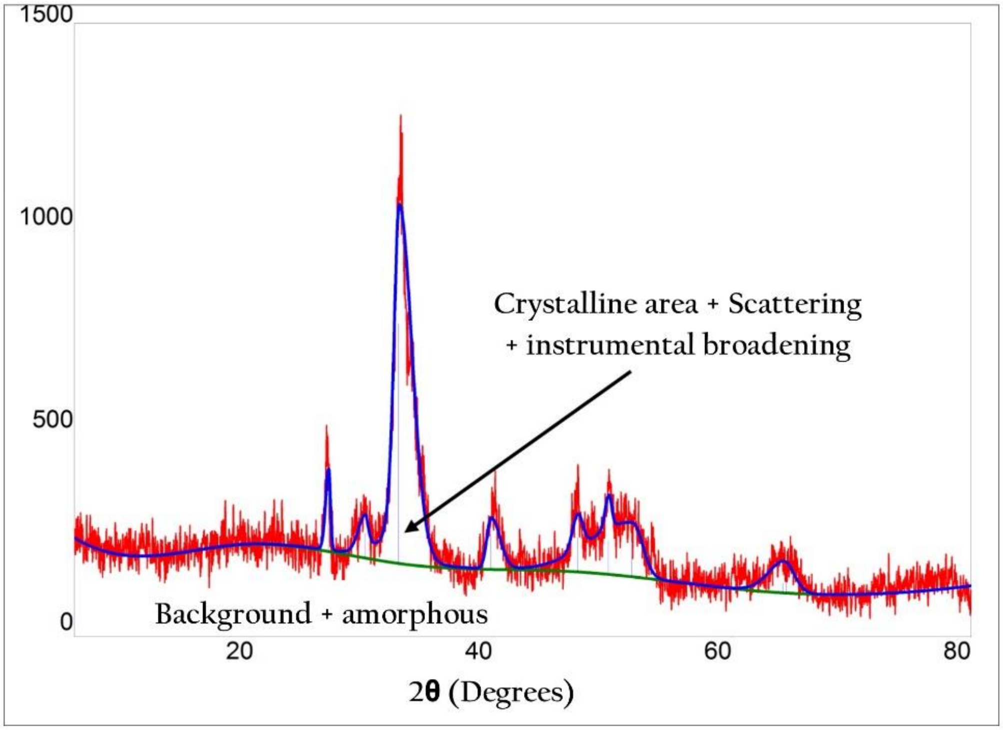

Figure 2. 6 X-ray diffraction pattern of defatted bovine bone powder.

Figure 2.6 shows a characteristic X-ray diffraction pattern of raw powder bovine cortical. In the case of micro-crystals, the crystalline area is taken from the base of the green line and the blue line that covers all diffracted peaks. The area below the green line corresponds to the background where there are contributions from the electronic noise of the system and the amorphous region of the material. However, this is not the case of HAp from mammalian bones, which is nanocrystalline. The interphase between the nanocrystals acts like a diffraction grating when the radiation interacts with the material. This phenomenon produces patterns with broad peaks that are, in fact, curves instead of patterns.

Ramirez-Gutierrez *et al.* (2016) studied the effect of the cooling rate on the structural properties of bovine cortical bone incinerated at 940 °C and cooled in liquid nitrogen, water, furnace air, and air. Figure 2.7 A shows the (211) peak for all samples, indicating that the sample cooled in the furnace produced the BIO-HAp with the best crystalline quality. Figure 2.7 B and C shows the procedure used to calculate the crystallinity quality using the (211) diffracted peak; Figure 2.7 B corresponds to the changes in the FWHM value of each sample, and Figure 2.7 C shows the inverse of this parameter. This calculation was possible because HAp crystals were grown until they reached micrometric sizes by calcination process.

The phase identification was obtained by using the Powder Diffraction File (PDF) that is part of the any X-ray diffraction system library. Usually, the ICDD card No. 00-009-0432 of hydroxyapatite is used, but others PDF files also can be used to its identification such as ICDD card No. 00-072-1243. These PDFs correspond to synthetic HAp, and then the peak positions of BIO-HAp indicate a shift due to the inclusion of other ions such as Mg, N, K, among others, which distort the lattice.

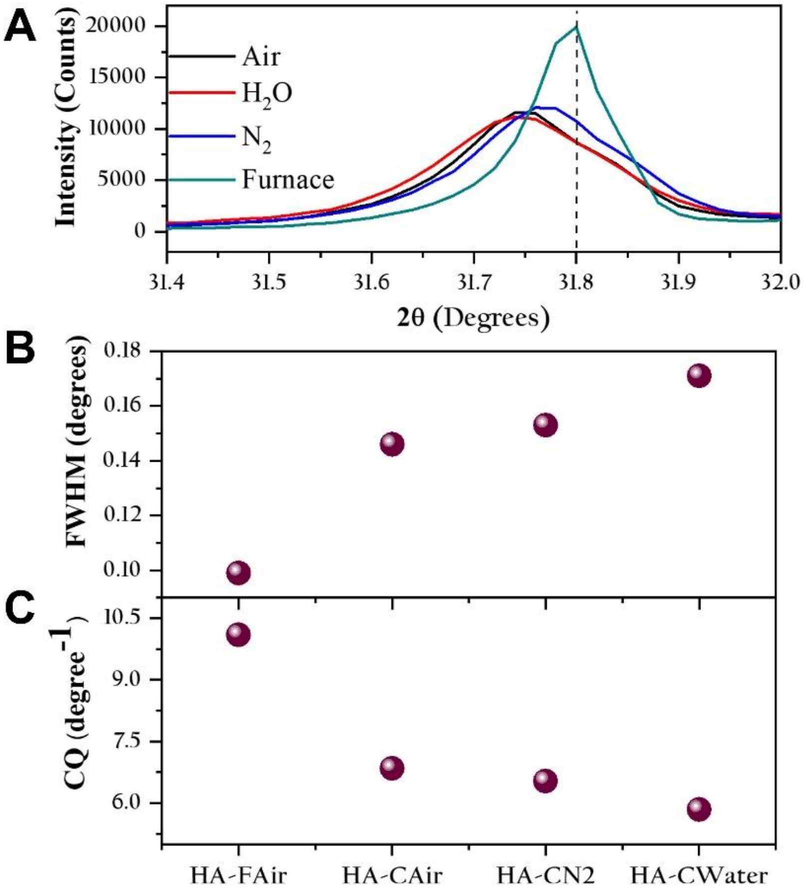

Figure 2. 7(A) (211) peak for all studied samples, the vertical dash line represents the position of the (211) peak for pure HAp. (B) FWHM values for this peak, and (C) inverse of FWHM (crystallinity quality).

- ***Mineral composition of BIO-HAp***

The ion traces of the following samples were quantified through inductively coupled plasma atomic emission spectroscopy (ICP-OES): bovine bone powder (BBP), BBP with a hydrothermal process (BBP-HTP), BIO-HAp from BBP-HTP calcinated at 600, 800, and 1100 °C (BIO-HAp600, BIO-HAp800, BIO-HAp1100). Table 2.2 shows the mineral traces in parts per million; the major elemental components are sodium and magnesium.

Because the presence of these traces enhances bone regeneration, it is important to monitor their presence in the material. The small variations in the mineral content indicate that these ions belong to the inorganic phase, and little losses can be attributed to the fusion temperature of some of them. Iron levels are low in comparison to the results reported in the literature; these low iron levels can be due to an adequate milling process without contaminants. The loss in the mineral content after the hydrothermal process is due to the partial removal of the organic phase, which indicates that some of the found ions are not in the HAp structure. Bone calcination at elevated temperatures does not produce a significant loss of substitutional ions. However, this lack of loss should not imply that this kind of process provides a suitable material for tissue engineering. HAp obtained by calcination at enough temperature guarantee the absence of any organic compounds, but its morphology, porosity, and surface area are not adequate for medical purposes. Synthetic scaffolds do not have these ions in their composition; they are quite dissimilar from HAp in biological sources. In this section, it is worth noting that the chemical composition of the bone can vary due to the diet, gender, and age of the animal, kind of bone, and the location of the studied bone, among other factors. Therefore, certain changes in the mineral content values are not due to the conditioning process (cleaning and calcination), but to the heterogeneous content of the sample. In the case of HAp from Sigma, it only has aluminum, iron, and zinc, which indicates that this HAp was obtained by means of a chemical process (Giraldo-Betancur *et al.*, 2013).

Table 2. 2 **Mineral composition of bovine bone, hydroxyapatites, and commercial samples.**

Sample	Mineral content (ppm)									
	Na	Mg	Al	K	Mn	Fe	Ni	Cu	Zn	Ba
Bovine Bone Powder*	6689.23	3048.49	33.98	414.89	—	9.89	—	—	90.17	—
BBP- HTP*	5463.60	2720.90	21.73	147.45	—	16.63	—	—	78.54	—
Bio-HA600*	7493.14	3818.75	32.27	211.08	—	17.01	—	—	130.70	—
Bio-HA800*	8546.57	4307.55	44.81	225.00	—	21.51	—	—	92.06	—
Bio-HA1100*	8111.94	3936.94	28.35	169.64	—	14.44	—	—	81.88	—
Defatted Bio-HA **	—	—	6.6 ± 0.21	345.27 ± 5.06	—	31.36 ± 0.1	—	1.07 ± 0.76	79.46 ± 0.98	294.08 ± 4.74
Bio-HA Alkaline**	—	—	6.66 ± 0.32	—	—	83.33 ± 14.5	—	5.22 ± 2.01	135.81 ± 0.25	241.99 ± 1.56
Bio-HA Calcined**	—	—	20.01 ± 1.27	228.14 ± 6.84	1.25 ± 0.04	42.71 ± 0.45	—	9.05 ± 0.22	139.38 ± 6.05	265.58 ± 13.15
NIST**	—	—	270.53 ±4.45	—	17.44 ± 0.11	645.45 ± 17.18	5.8 ± 0.54	2.7 ± 0.01	180.87 ± 3.38	240.76 ± 5.16
Apafill G**	—	—	103 ± 2.9	—	59.73 ± 1.97	137.17 ± 4.86	—	15.33 ± 0.46	24.88 ± 1.16	150.3 ± 5.02
Biograft **	—	—	6.62 ± 0.92	—	—	16.69 ± 1.42	—	—	119.05 ± 2.64	1.62 ± 0.07
Sigma Aldrich**	—	—	5.72 ± 0.6	—	—	11.57 ± 1.45	—	—	3.66 ± 0.08	—
Coralina **	—	—	14.29 ± 0.28	—	—	25.98 ± 0.33	—	3.98 ± 0.88	6.94 ± 0.26	8.49 ± 0.11

*This work, **Giraldo-Betancur et al., 2013.

Collagen

Collagen has a supramolecular structure with periodicity and hierarchical levels. The primary structure of collagen is composed of a typical amino acid sequence that determines the collagen type; there are 21 different types of collagens with at least 42 polypeptide chains. Collagen I-type is the main protein in the bone; it is composed of three left α-helices with a length of about

300 nm and variable diameter from 4 to 20 nm. Each chain has about 1050 aminoacid. Two chains are named α(1) because they have the same amino-acid sequence and the other one is called α(2). The general sequence for collagen chains is −(Gly-X-Y)n−, where X is proline and Y is hydroxyproline (Olszta *et al*., 2007). Tropocollagen is aligned to form fibrils of about 200 nm, but these fibrils are not continuous. Collagen fibrils have gaps with a length of about 40 nm where hydroxyapatite crystals are located; because there is a low concentration of proline and hydroxyproline, these zones have high structural flexibility. The high thermal stability of collagen is due to the structural arrangement and its chemical bonds; in triple helix chains, there are hydrogen bonds between amino and carboxyl groups of amino acid chains. The main function of collagen is to give flexibility, elasticity, and tensile strength longitudinally. Biomechanical properties that collagen gives to bone depend on concentration, spatial orientation and bond stability. Collagen incorporated in grafts can produce an immunologic response, and for this reason, its presence in implants should be avoided.

Other components of organic phase are non-collagen proteins such as osteocalcin (BPG), osteonectin (ON), osteopontin (OPN), thrombospondin (THBS1), bone morphogenetic proteins (BMPs), and bone sialoproteins (BSP)), polysaccharides, lipids, cytokines, and primary bone cells: osteoprogenitors, osteoblasts, osteocytes and osteoclasts (Campa-Molina *et al*., 2007). Osteoprogenitor cells promote the formation of osteoblasts, these cells are responsible for the creation of new bone through collagen secretion that is after coated with non-collagen proteins. The non-collagen proteins can retain minerals (mainly calcium and phosphate), and these aids the blood flow. Osteocytes are needed cells to maintain biomechanical properties of bone tissue; these cells are osteoblasts that have been trapped in the matrix during the mineralization process, and they take on a starry appearance. Finally, osteoclasts secrete substances that dissolve the inorganic bone phases for bone resorption. Finally, osteoclasts secrete substances that dissolve the inorganic bone phases for bone resorption. Phosphate and calcium ions are deposited in the collagen matrix to form an amorphous calcium phosphate that is subsequently turned into hydroxyapatite. As it was mentioned earlier, the mineral phase has citrate, magnesium, and other minority ions that contribute to the mineral structure being more stable. These traces contribute to hard tissue life cycle because they influence some biochemical reactions related to bone metabolism (Akram *et al*., 2014). The mechanism of bone formation is still unclear, and the knowledge about it is limited. Minerals in the bone provide rigidness and hardness due to the packed crystals within the collagen gaps; hence, these properties depend on the mineral quantity, packaging level, and the crystal ordering around the collagen fibers.

Osteocalcin

Osteocalcin (BPG-Bone Gla Protein) is a non-phosphorylated glycoprotein; rather, it is the main non-collagen protein in the bone. BGP helps to capture osteoblasts and osteoclast cells which play an essential role in bone formation and resorption during the specimen life, respectively. This protein also influences the bone mineralization due to its high affinity with hydroxyapatite but, the reaction mechanism has not been clarified yet. BGP has negative charges on its surface which coordinate five calcium ions in a particular configuration that is complementary to calcium ions in hydroxyapatite (Hoang *et al*., 2003). Human BGP has 49 amino-acids but, it is not constant for the diverse species, there is a range of 46 to 50 amino acids depending on the specie (γ-carboxyglutamic acid (Gla) is in the amino acids sequence). According to the bone sample and its age, the composition can be up to 20 % of non-collagen proteins in adult bones and about 2% of total bone proteins. There is a 90 % similarity between human and bovine osteocalcin for the amino acids sequence, especially in the central zone of the protein where there is a high concentration of Gla residues. BGP exhibits a folded structure due to disulphide bridges of cysteine (Cys), that is present into the BGP residues (Diaz, 1996). Through X-ray diffraction and Nuclear Magnetic Resonance (NMR), it has been determined that BGP is a globular protein made out of three alpha-helices, a hydrophobic core, an N-terminal as β-sheet, and a C-terminal as β-sheet exposed. The amino-acid sequence is NH_2-tyr-leu-tyr-gln-trp-ley-gly-ala-pro-tyr-pro-asp-pro-leu-gla-pro-arg-arg-gla-val-cys-gla-leu-asn-pro-asp-cys-asp-glu-leu-ala-asp-his-ile-gly-phe-gln-glu-ala-tyr-arg-arg-phe-tyr-gly-pro-val-COOH. The position of three Gla residues are the same for both sources: 17, 21, and 24.

Water

Water dwells within vascular channels that flow into the collagen and the mineral matrix. Due to polarity of water, it can interact with both phases, then, water is bonded with hydrophilic groups of the collagen (glycine, hydroxyproline, carboxyl, and hydroxylysine) and with charged groups such as phosphate and calcium ions. In addition, water has two interaction types with mineral phase: surface bonded water and lattice water (Behari, 2009). The water with the first interaction type is lost at low temperature during a calcination process (< 200 °C) as it was seen in the thermal degradation section, but the lattice water which is bonded to the structure, requires a higher temperature to break the bonds (200-400 °C). There is free water that fills the Haversian canals and the lacuno-canalicular system (see Figure 2.1). This water provides viscoelastic properties to the bone, and it is the cause of nutrient diffusion. During mineralization and demineralization processes, ions need to be transported to and from osteoid sites. Therefore, this water serves as a means of transport (Behari, 2009). Wilson *et al.* (2006) reported water in two different crystal lattice environments in the bone: lattice water and surface water. Lattice water is bonded to the crystal in vacant sites of carbonated hydroxyapatite, which provides structural stability through the hydrogen bond formation between ions. The collagen and the mineral phase can be mechanically coupled due to the surface water; this water type serves as a cushion against mechanical stress. The surface water has a dual-action mechanism. First, the water movement allows that the bone support the mechanical stress with less deformation, and second, this water protects the collagen from the shear under uniaxial stress by serving as a sacrificial layer.

Fat

Lipids (2-4%) in the organic phase are essential for bone metabolism and mineralization. The main lipid source are cells because they have a lipid membrane that regulates the input and output flux of components to the cell. There are lipids in the extracellular matrix—associated with the collagen as extracellular matrix vesicles (ECMVs) where bone calcification actively occurs. Particular complex phospholipid acids have been identified in the actively mineralizing tissues. These phospholipids are present in less quantity in the mineralized tissue, and they can nucleate mineral formation and regulate the growth of mineral crystals. Also, there are other lipids in the bone that are important for bone cell function: leptins can be essential for osteoblast function stimulation, which causes the formation of the bone as well as osteoclast activity suppression or bone resorbing (Boskey, 2004). Regarding tissue engineering, it is important to remove this component from the bone to avoid interference with other organic and inorganic compounds of the bone.

2.3. Methods to obtain HAp and BIO-HAp

There are many ways to obtain hydroxyapatite; it can be synthesized through dry methods (solid-state and mechanochemical methods), wet methods (emulsion, chemical precipitation, hydrolysis, sol-gel, hydrothermal, and sonochemical methods), and by high-temperature processes (combustion, pyrolysis, or obtaining from biogenic sources) (Sadat-Shojai *et al*., 2013; Thuault *et al*., 2014; Méndez-Lozano *et al*., 2017). Only when HAp is obtained from bio-waste, like mammalian bones, is it named BIO-HAp. Some properties of synthetic HAp are stoichiometry, high purity, homogeneous composition, and nanometric sizes. Synthetic HAp is ideal for applications related to adsorbents, sensors, catalysis, and chromatography for protein extraction and purification (Gómez Ortega *et al*., 2004). Dry methods do not use liquid solvent, and they are used for mass production; large hydroxyapatite with an irregular shape is obtained as a result of these methods, while wet methods produce nanometric hydroxyapatite with regular morphologies. Formation of secondary calcium phosphate phases is presented as a disadvantage of the HAp obtained by wet methods, but the mineral phase of mammalian bones has, in fact, these other phases (Londoño-Restrepo *et al*., 2018). Hydroxyapatite from mammalian bones is like human HAp, which is not stoichiometric due to the presence of substitutional ions like Na^+, K^+, Mg^{2+}, Ba^{2+}, F^-, Cl^- that are bonded to the crystal lattice. BIO-HAp has a deficient calcium content due to the substitution by the carbonated group, sodium, potassium, magnesium, zinc, or calcium.

It has been reported that processes that involve high temperature are suitable for producing high purity homogeneous HAp in a one step process, but HAp loses porosity and surface area after calcination at 700 °C. It is worth noting that processes at high temperatures not only consist of bone calcination, they also involve the synthesis of HAp from natural precursors such as algae, corals and eggshell (Akram *et al*., 2014).

CHAPTER 3

MATERIALS AND METHODS

3.1. Effect of the high heating rates on the physicochemical properties of BIO-HAp

- **Preparation of samples**

Samples were obtained from bovine cortical femur bone (2-years-old) collected from the local slaughterhouse (folio number SDA-537295-98, 2011) located in Queretaro City, Mexico. The bone conditioning method proposed by Londoño-Restrepo *et al.* (2016) was used to obtain the inorganic phase of the bone. Then, a primary cleaning was carried out by manually removing the marrow in bone slices 3 cm length. After this, soft tissue and blood vessels were eliminated by boiling them in deionized water at high pressure (154°C, 1.2 atm) during 40 min using an All American 1915X autoclave. The boiling process was done three times. Next, bone slices were placed in a vacuum at 90 °C for 5 days to weaken the bone structure facilitating the dry milling. Finally, dry slices were pulverized in a vibrating cup mill. Powder bovine bone (BB) was obtained using the US mesh 100 (149 µm); particles smaller than mesh 100 were collected in the plate for this research and BB with hydrothermal process was also studied (BB HP).

Powder bovine bone was subjected to a hydrothermal process to remove fat and denaturalize proteins using only deionized water as a solvent with a ratio 1:10. This process was carried out three times. Liquid fraction from this step was collected in a beaker, and it was left to sediment for five hours, then it was decanted and filtered to obtain the liquid fraction free of inorganic phase. This fraction was cooled at -40 °C and freeze-dried for 48 h using a Free Zone 2.5 freeze dryer (Labconco, Kansas City, USA). Powder bovine bone with the hydrothermal process (BB-HP) was dried in an oven at 90 °C for 24 h. The calcination process was carried out to obtain bio-hydroxyapatites at different nominal heating rates (7.4, 9.9, and 11.1 °C/min) from 700 to 1100°C taking samples each 100 °C.

Other set of samples was calcined from 520 to 620 °C each 20°C at 7.4°C/min to understand the thermal events that take place in this range of temperature according to the calorimetric study. These samples were analyzed only by SEM and X-ray diffraction to correlate structural and morphological changes with the thermal transitions. A Felisa furnace (Mexico) was used to calcination and all samples were cooled into the furnace in an air atmosphere. A data collection system was incorporated to the furnace to obtain the thermal histories and guarantee the reproducibility of the thermal treatment. Average temperature for the first isothermal condition at 620 °C was 619.8 °C and average experimental annealing temperatures for 700, 800, 900, 1000, and 1100 °C were 714.8, 810.2, 906.3, 1002.8, and 1096.1 °C, respectively. These thermal variations were due to environmental conditions in the room and by the thermal inertia of the furnace. Then, studied samples were: Powder bovine bone (BB), powder bovine bone with hydrothermal process (BB-HP), BB-HP calcined from 520 to 620 °C each 20 °C at 7.4°C/min, and bio-hydroxyapatites obtained by calcination of BB-HP at three heating rates (7.4, 9.9, and 11.1 °C/min) from 700-1100 to determine the influence of the heating rate and annealing temperature on physicochemical properties (700, 800, 900, 1000, and 1100; heating rate for each temperature is indicate in the graphs).

- **Thermal analysis: DSC and TGA**

Thermogravimetric curves and calorimetric measurements were carried out simultaneously using a STA 449 F3 Jupiter Netzsch thermal analyzer. 12 ± 0.1 mg of sample mass was placed in a crucible alumina. Samples were heated from room temperature to 1100 °C at the heating rates of 7.4, 9.9, and 11.1 °C/min, following the methodology proposed by Londoño-Restrepo *et al.* (2016). The measurements were carried out in a constant N_2 flow. Data were analyzed through Proteus software.

- **Compositional Analysis: ICP-OES**

This technique was used to analyze the elemental composition of the samples treatment at different heating rates and temperatures, and the powder bone as well as the lyophilized liquid fraction obtained from the hydrothermal process to study the chemical elements released during the treatment. Thermo Fischer Scientific ICAP 6000 Series equipment with argon plasma was used. 0.1 g of each sample was digested with 7 mL of nitric acid (Baker 69.3 %) and using a temperature program; it was made in duplicate. After this, samples were filtered (Whatman No. 42) and the volume was completed to 100 mL. Finally, samples were exposed to argon plasma and the elements were excited to be identified by their characteristic emission spectra that were converted to elemental content by comparing to a standard curve.

- **Morphological studies: SEM**

Morphologic analysis of all BIO-HAp samples obtained at different heating rates and temperatures, powder bovine bone (BB), and powder bone after the hydrothermal process (BB-HP), as well as samples calcined from 520-620 °C each 20 °C was carried out in a Jeol JSM 6060LV Scanning Electron Microscope, with an electron acceleration voltage of 20 kV. The samples were fixed on a copper holder with carbon tape and a gold thin film was deposited on them.

- **Structural Analysis: DRX**

X-ray diffraction technique was used to determine the crystalline phases and changes in the crystalline quality by studding the changes in the Full Width at Half Maximum (FWHM) in the BIO-HAp samples obtained at 7.4, 9.9, and 11.1 °C/min from 700 to 1100 °C, powder bovine bone (BB), and powder bone with hydrothermal process (BB-HP). Samples were densely packed in an Al holder. The X-ray diffraction patterns were obtained using a Rigaku Ultima IV diffractometer operating at 40 kV, 30 mA with CuKα radiation wavelength of λ=1.5406 Å. Diffractograms were taken from 5 to 80° in a 2θ scale and 0.02 step size.

- **Vibrational Analysis: Raman**

BIO-HAp samples obtained by calcination at 700, 800, 900, 1000, and 1100 °C at three different heating rates: 7.4, 9.9, and 11.1 °C/min were analyzed using a Labram model micro spectrometer (Senterra, Bruker) equipped with an Olympus microscope with a 20× objective. The Raman spectra was excited by a helium–neon laser (785 nm) with an output of 25 mW reaching the sample. Spectral ranges were of 300–1500 and 3500–3600 cm-1 to analyze BIO-HAp. Powder bovine bone, powder bovine bone with hydrothermal process, and HAp calcined at 620 °C were not analyzed in this work because these samples were well studied in a previous work (Londoño-Restrepo *et al.*, 2016).

3.2. Study of trabecular bone

- **Collection and preparation of samples**

Trabecular bone samples were obtained from bovine femur bones (2 years old) collected from the local slaughterhouse (folio number SDA-537295, 2014). The trabecular bone corresponds to the internal part of the femur head (Figure 3.1 A). X, Y, and Z directions were assigned according to the femur position that is shown in this figure. The femur head was sawed into slices of 1.1 cm thickness in order to obtain cubes of 1.4. x 1.4x 1.4 cm. Figure 3.1 B shows a single slice taken from the central part of the femur head (frontal view). Figure 3.1 C shows a frontal view of a cube obtained from a trabecular bone slice. Also, in the trabecular bone cube, X, Y, and Z, directions were defined (Figure 3.1 D) to study the structural, morphological, and mechanical properties for different directions. The Z direction is parallel to the femur length, the Y direction was defined as the direction from the external to the internal part of the femur head, and the X direction corresponds to the forward part of the femur head. The sponge cube shown in Figure 3.1 D was defatted by Soxhlet extraction using petroleum ether and washed with H_2O_2 to remove some organic compounds. Therefore, this cube is whiter than cubes in other pictures.

- **Thermal behavior**

The thermogravimetric curve for DSC and its second derivative in relation to temperature were obtained for the bovine trabecular bone powder sample using a TG Q500 equipment (TA Instruments). The sample mass was 12.0±1.0 mg of each sample, and these were placed in a platinum crucible of thermo balance (TA Instruments, USA). The samples were heated beginning at room temperature and up to 1200 °C, at a heating rate of 10 °C/min; the measures were carried out in a constant N_2 flow. The TG data was processed with the use of a Universal Analysis 2000 TA software.

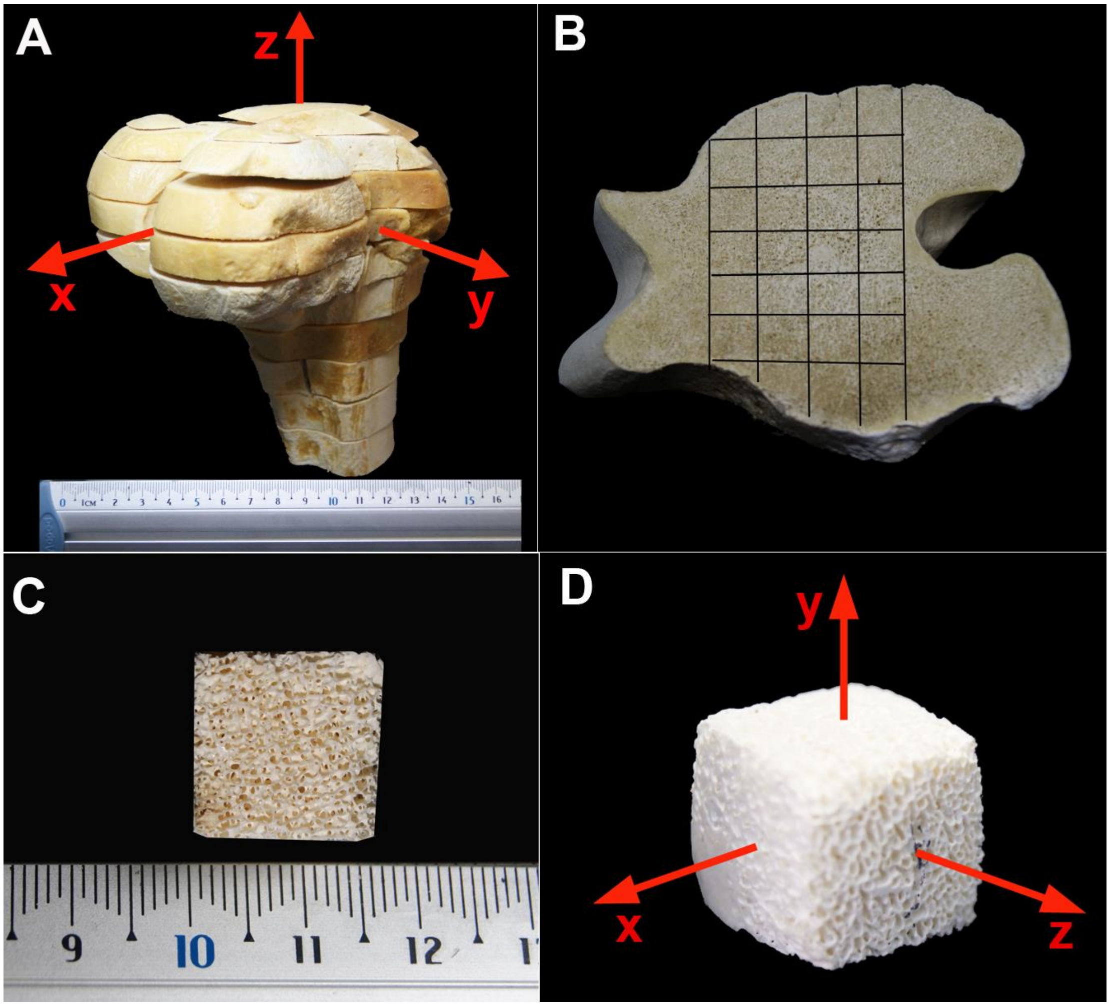

Figure 3. 1 (A) femur head, (B) shows a transversal slice cut from the central part of the femur head; (C) frontal view of the spongy cube cut from the femur slice (XY plane). (D) cube with *X*, *Y*, and *Z* directions were defined.

- **Vibrational Raman spectroscopy of spongy bone**

Raman spectroscopy is a non-destructive technique that provides chemical and vibrational information about functional groups in a molecule. This method is based on the analysis of inelastic dispersed light when a monochrome light beam interacts with the matter. The characterization was made using a Senterra-Bruker spectrophotometer with a He-Ne (785 nm) laser and a potency of 25 mW; the working distance was defined using a 20× objective lens. The global spectral resolution was 2 Δcm^{-1}.

- **Elemental composition: ICP-OES**

Bone powder was obtained from bovine trabecular bone by milling in a vibratory disc mill until 147 µm particle size (BTBP). After that, this powder was defatted by Soxhlet with petroleum ether, and deproteinized by immersion in hydrogen peroxide. Trace elements composition of the trabecular bone was determined by ICP-OES, using a Thermo iCAP 6500 Duo View equipment. 0.1 g of sample was digested with nitric acid (Baker 69-70 %), and it was made twice. The elements in the digested sample were excited by argon plasma, and each one emitted a characteristic emission spectrum when they returned to the ground state. The emission intensity was converted to elemental content by comparison with a standard curve.

- **Morphological characterization**

In the study of the trabecular bone, two parameters were widely analyzed: pore size and interconnectivity. SEM images of the sponge cube (Figure 3.1 D) for XY, YZ, and XZ planes were taken to study its tridimensional morphologic. A Jeol JSM 6060LV SEM was used with 20 kV electron acceleration voltage. The sample was fixed in a cooper holder with carbon tape. Gold covering of the samples was not necessary, indicating that the cleaning process removed organic phase components.

- **X-ray tomography.**

A cubical piece of spongy bone was scanned by X-ray computed tomography (CT) using an XTH 225 ST Nikon system. X-ray CT is a useful non-destructive technique capable of resolving microstructures like channel networks inside the trabecular bone. The X-ray CT setup consisted basically of an X-ray source tube, a detector, and a 360 degree rotary table. The scan protocol included securing the sample with synthetic foam transparent to the X-rays, in a cone-beam CT setup with X-rays generated by a tube accelerating voltage of 165 kV and tube electrical current of 100 µA, and collecting up to 2880 radiographs over a 360° rotation with an integration time of 708 ms per image. The bone sample was scanned with a resolution of about 10 micrometers. After scanning, the reconstruction was performed with a FDK (Feldkamp-Davis-Kress) type algorithm (Feldkamp *et al.*, 1984) to produce a 3D image as well as serial cross-sectional images of the bone sample. These consisted of matrices of 2000 × 2000 pixels which collectively composed a volume of isotropic $(20\ \mu m)^3$ for the bone slices and $(10\ \mu m)^3$ for the small cube sample. The latter was achieved by increasing the magnification of the CT setup. Once the 3D reconstruction was complete, a local adaptive or dynamic gradient threshold was applied for better surface determination. For visualization and pore network analysis, the software package VGStudio Max 3.0 from Volume Graphics, GmbH was used.

The schematic workflow chart for the full CT process is shown in Figure 3.2. The 3D image in gray values represents a 3D volumetric density map of the X-ray absorption coefficients for the specimen along the crossing paths of the X-rays. This map depends on both the density and composition of a specimen's material and the energy of the X-rays passing through it. Each gray level offers information about what the X-rays have encountered in their paths and their spatial location, thus revealing the external and internal structures of an object. While surfaces of the objects are not explicitly defined in this technique, they can be extracted from the reconstructed volume using a precise surface determination algorithm. Once the surface determination is made, with special calibrations, CT analysis can then provide the specimen's dimensional results (Villarraga-Gómez *et al*., 2018). As a result, interior measurements can be obtained as well as localization of structural material inclusion and identification of tissue clusters not usually visible through traditional methods of nondestructive testing. Once the scans were completed, dimensioning of the specimen was performed for size and morphology determination, and for measurement of voids/porosity distribution, and location of the bone tissues.

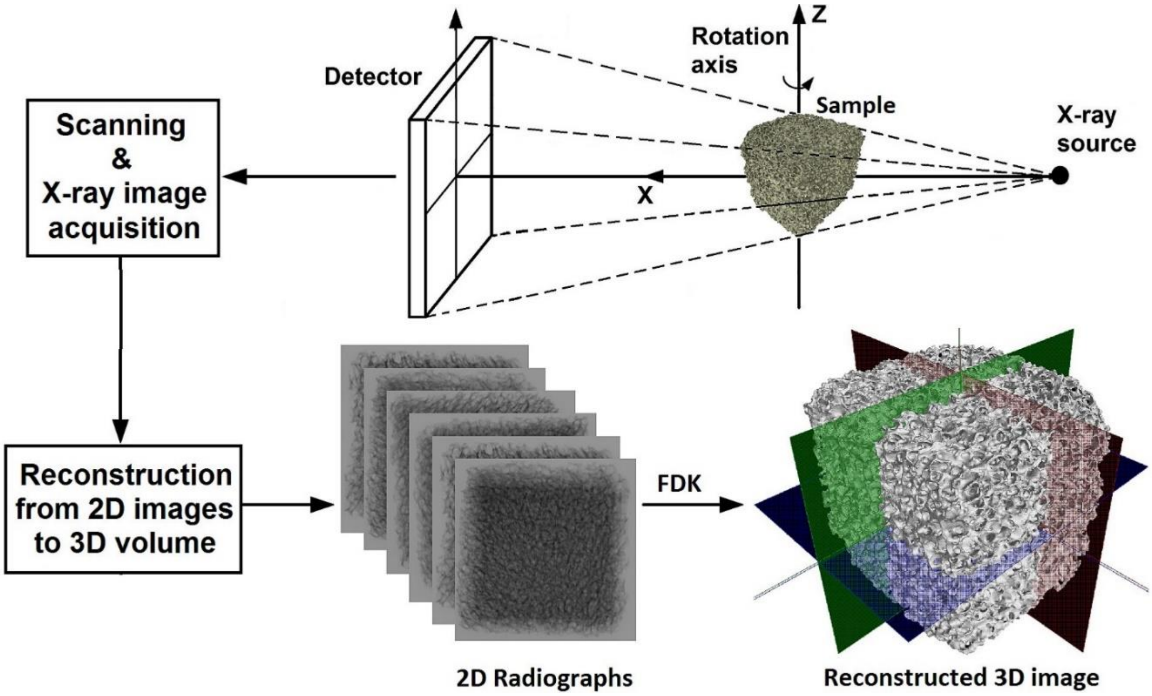

Figure 3. 2 CT process diagram.

- **Structural properties**

X-ray diffraction patterns of each sponge direction were obtained perpendicular to XY, YZ, and XZ planes (Figure 3.1 C). A Rigaku Ultima IV diffractometer was used to obtain the diffraction patterns, with the following operation parameters: 40 kV, 30 mA with Cu K_α radiation wavelength of λ=1.5406 Å, and from 5 to 80° in a 2θ scale and step size of 0.02°.

- **Mechanical properties**

The compressive tests of the cubes (1.4 x 1.4 x 1.4 cm) were carried out using a (HCT.25-400, Zwic/Roell Company, Germany) testing machine at 1 mm/min with a 500 N load cell. Compression tests for the XY, YZ, and XZ planes were discontinued when the height of the test bodies was reduced by two-thirds. The strength parameters: compressive strength, limit of proportionality, compression at rupture, and modulus of elasticity were analyzed following the methodology described elsewhere (Lindahl, 1976). Cleaned and dried bone cubes were subjected to a compression test with a deformation rate of 0.05 mm/min. The samples were reconditioned for 1 month at 60% relative humidity and 23°C.

3.3. Effect of the nano crystal size on the X-ray diffraction patterns of biogenic hydroxyapatite from human, bovine, and porcine bones

- **Raw bone and annealed samples**

Bovine, porcine, and human bones samples from femurs were used in this work. Human femur without apparent pathologies was donated by the Universidad Autónoma de Querétaro, femurs from bovine and porcine were collected from the local slaughter house. Cortical bone samples from each source were defatted and deproteinized following the methodology proposed by Londoño-Restrepo *et al*., (2018) to obtain clean bone powders. Each powder was sieved in a US 200 mesh (75 µm). These samples were dried and labeled as B-Raw for bovine, P-Raw for porcine, and H-Raw for the human. A fraction of each sample was simultaneously calcinated in a Felisa (Mexico) furnace at 720 °C and 6 °C/min heating rate for 10 min and cooled in furnace air according to thermal profile showed in Figure 3.3. These last samples were labeled as B-720 for bovine, P-720 for porcine, and H-720 for human calcined at 720 °C. Synthetic hydroxyapatite from Sigma Aldrich (No. 28,939-6) was used for comparative purposes.

- **Mineral content: ICP**

The mineral composition of the raw and calcined samples as well as Sigma HAp was determined using the methodology proposed in the section 4.1.

- **TEM and SEM characterization.**

A high-resolution transmission electron microscope (S) TEM (JEOL ARM200F) was used to determine the crystal size of the BIO-HAps samples by using Image J free version, and images were processed using the Digital Micrograph software V4.0 from Gatan and the array mask was applied to clean the FFT signal. SEM images of the incinerated samples were obtained using a High-Resolution Scanning Electronic Microscope (SEM) model SU8230(Hitachi).

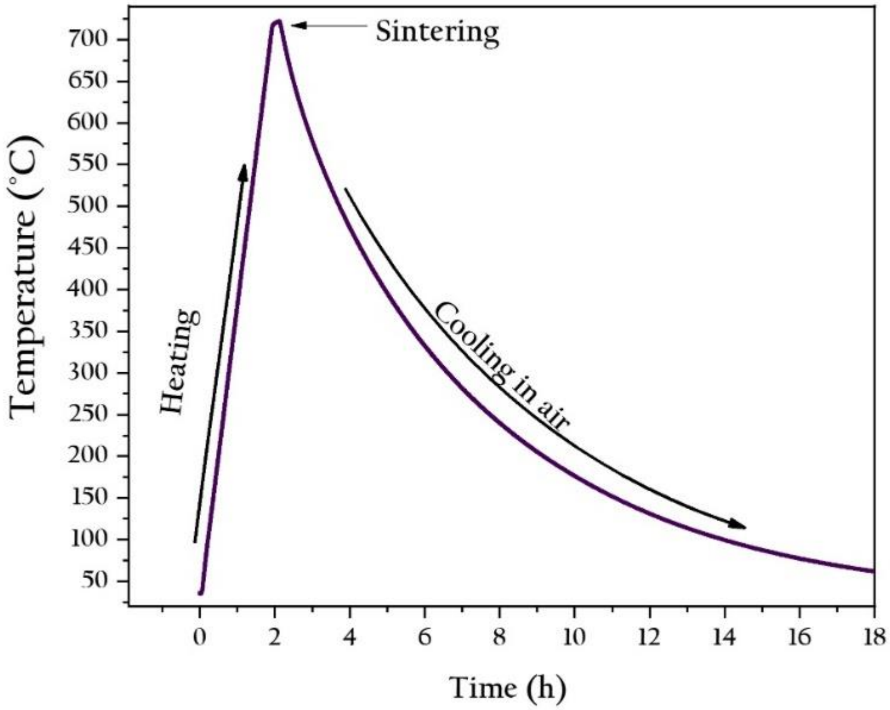

Figure 3. 3 Thermal history of bone powder calcinated at 720 °C: B-720, P-720, and H-720.

- **X- ray diffractions of bone.**

X-ray diffraction technique was used to obtain the patterns of synthetic HAp from Sigma Aldrich, clean bone powders B-Raw, P-Raw, and H-Raw, and calcined samples B-720, P-720, and H-720. The FWHM for all these samples was used to evaluate the effect of the crystal size on the XRD patterns. Patterns were obtained using a Rigaku Ultima IV diffractometer operating at 40 kV, 30 mA with CuK$_\alpha$ radiation wavelength of λ=1.5406 Å. Diffractograms were taken from 5 to 80° in a 2θ scale and 0.02° step size for phase identification. The effect of the crystal size on the shape of the diffraction patterns was analyzed by a simulation done using PDF-4 software by varying the crystallite size remaining a perfect order in the crystalline structure.

3.4. Effect of the crystal size on the infrared and Raman spectra of bio hydroxyapatite of human, bovine, and porcine bones

- **Raw bone and annealed samples**

Cortical bones from bovine, porcine, and human femurs were used for this work. Human femurs (56 years old) without any apparent pathologies were provided by the Universidad Autónoma de Querétaro while bovine bones (3-years-old) and porcine bones (157 days) were collected from the local slaughterhouse (folio number SDA-537295-98, 2017). All bones were defatted and deproteinized using the procedure reported elsewhere (Londoño-Restrepo *et al.*, 2018). These bones were pulverized and sieved in a US 200 mesh (75 µm) to obtain powders with particles smaller than 75 µm. The bone powders were subjected to an alkaline hydrothermal treatment to remove the protein in a $Ca(OH)_2$ solution (Mallinckrodt Baker CAS No 1305-62-1). Raw samples were labeled as B-Raw for bovine, P-Raw for porcine, and H-Raw for the human. Afterward, the samples were incinerated at the same time using a Felisa (Mexico) furnace at 720°C at a heating rate of 6°C/min and a sintering time of 10 min and later cooled inertially into the furnace in the presence of air. The annealed samples were labeled as B-720 for bovine, P-720 for porcine, and H-720 for the human. A synthetic HAp from Sigma Aldrich was used for a comparative purpose.

- **HRTEM characterization**

HRTEM images of B-Raw, P-Raw, and H-Raw were obtained. A high-resolution transmission electron microscope (S) TEM (JEOL ARM200F) was used to determine the crystal size of the bio hydroxyapatite samples; the acceleration voltage was 200 kV.

- **Mineral content: ICP**

The mineral composition of the raw clean bones, calcinated samples, and synthetic sample was determined with a Thermo Fischer Scientific ICAP 6000 Series equipment with an argon plasma. 0.1 g of each sample was digested with 7 mL of nitric acid (Baker 69.3 %) using a temperature program; samples were analyzed in duplicate. Afterward, the samples were filtered (Whatman No. 42) and their volume was completed to 100 mL with deionized water. Finally, the samples were exposed to the argon plasma to excite the elements in the samples to identify them through their characteristic emission spectra.

- **Infrared spectroscopy**

Infrared spectroscopy was used to follow the cleaning process aimed to defat and deproteinize the bones until the complete removal of the organic phase as well as to determine the influence of the crystal size on the infrared spectra of raw samples and samples incinerated at 720°C. The measurements were performed on a 6700 FTIR Thermo Scientific spectrometer equipped with an ATR (Attenuated Total Reflectance) accessory with a diamond crystal in the spectral range of 400 to 4000 cm^{-1} at a spectral resolution of 4 cm^{-1}.

- **Raman spectroscopy**

All bone samples were analyzed using a Senterra Raman spectrometer from Bruker, equipped with a 785 nm laser and an Olympus microscope. A 20X objective was used, the spectral range measured was from 70 to 3500 cm^{-1}, with a resolution of 3 cm^{-1} and the following instrument parameters: a 50 µ aperture, 100 mW of laser power of, 6 s integration time and 6 scans.

- **Morphological studies of incinerated samples: SEM**

Morphologic analysis of all BIO-HAp samples calcined at 720°C was carried out in a Jeol JSM 6060LV Scanning Electron Microscope, with an electron acceleration voltage of 20 kV. The samples were fixed on a copper holder with carbon tape and a gold thin film was deposited on them.

- **X ray diffractions**

The X-ray diffraction technique was used to obtain the diffraction patterns of clean bone powders B-Raw, P-Raw, and H-Raw, calcined samples B-720, P-720, and H-720, and synthetic Sigma Aldric. The Full Width at Half Maximum (FWHM) obtained for the peak located at 25.879 ° in 2θ scale, corresponding to the (002) crystalline orientation of these samples was used for comparative analysis. These patterns were obtained using a Rigaku Ultima IV diffractometer operating at 40 kV, 30 mA with CuK$_\alpha$ radiation wavelength of λ=1.5406 Å. Diffractograms were taken from 5 to 80° in a 2θ scale and 0.02° step size.

3.5. *In situ* study of hydroxyapatite from cattle during a controlled calcination process using HT-XRD

- **Samples obtaining**

Samples were obtained from bovine cortical bone (2-years-old) collected from the local slaughterhouse located in Queretaro City, Mexico (folio number SDA-537295-98, 2017). Samples consisted of bone powders (<147 μm) cleaned according to Londoño-Restrepo *et al.* (2016) including a thermo-alkaline process at 127 °C for a partial removal of the organic phase as follows: powder bovine bone was deproteinized with a hydrothermal method at 1.2 atm in calcium hydroxide 0.005 M (pH=11) and 1:10 ratio; this process was carried out three times. This cleaning process using solvents was done to remove the organic phase without modifying the hydroxyapatite structure. In general, the removal of fat, protein, and water facilitate the milling step, and the reduction of the minerals from the organic phase, that are not desired because they can contribute to secondary reactions (Londoño-Restrepo *et al.*, 2018). Clean bone crystals were analyzed through High-Resolution Transmission Electron Microscopy (HR-TEM). Regarding calcined samples, two sets of them were studied *in situ* and ex situ. The *in situ* analyses included differential scanning calorimetry (DSC) and high-temperature X-ray diffraction (HT-XRD). The second set was bone powder heated in a furnace from 400 to 900 °C at 6 °C/min and then characterized by scanning electron microscopy (SEM) and inductively coupled plasma (ICP). Figure 3.4 A shows the method used to prepare the bone powder before *In situ* HT-XRD experiments and the BIO-HAp obtained for the morphological characterization. Figure 3.4 B shows a characteristic thermal profile used during the *in situ* HT-XRD for hydroxyapatite from bovine bone heated at 3°C/min.

- **Compositional Analysis: ICP**

This technique was employed to analyze the elemental composition of the defatted and deproteinized bone and samples calcined in a FE-360 furnace (Felisa, San Juan de Ocotán Zapopan, Jalisco, México) at 700, 800, and 900 °C at 3, 6, and 9 °C/min each one. A Thermo Fischer

Scientific ICAP 6500 DUO Series equipment using an internal standard of 1 ppm Yttrium to evaluate the signal of the spectrometer with an error less than 10 %. Calibration curves were prepared for each element with seven points from100 ppm (Inorganic Ventures solutions). Correlation coefficients were higher than 0.9990 and recovery rates higher than 90 % were evaluated using the reference standard material from the High Purity Standards EPA 200.7.

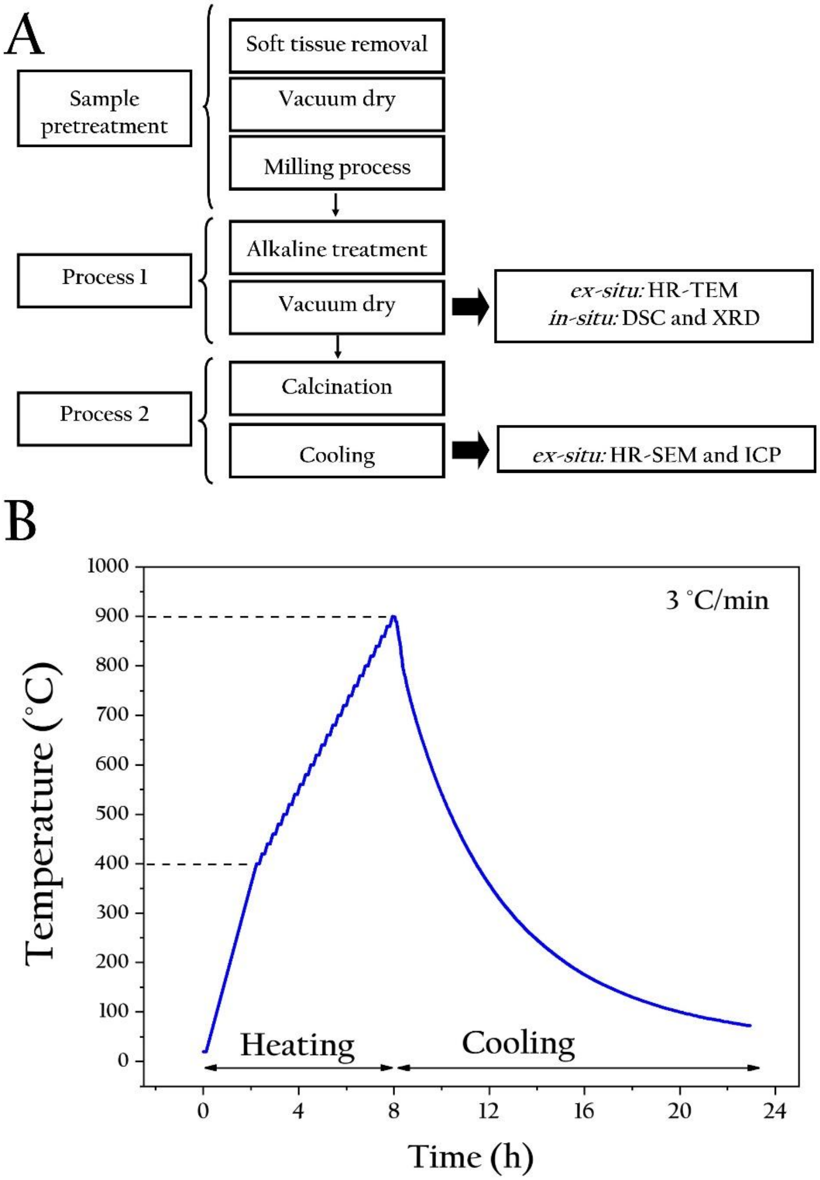

Figure 3. 4 (A) Diagram process followed to obtain and characterize bone samples. (B) Heat treatment for *in situ* thermal XRD from 400 to 900 °C every 20 °C at 3 °C/min.

0.1 g of each sample was digested in 7 mL of nitric acid (69.3 % Baker AnalyzedTM A.C.S Reagent, J.T. Baker) and using a heating cycle. After this, the samples were filtered (Filter paper-Whatman No. 42), and the solutions were adjusted to 100 mL. Finally, samples were exposed to an argon plasma where the elements were excited to be identified by their characteristic emission spectra that was converted to elemental content by comparing it with a standard curve. This analysis was made twice. The elemental analysis was done according to EPA 200.7 method.

- **Morphological analysis: SEM**

SEM images of BIO-HAp powder samples were taken to study morphological changes close to the crystal size transition temperature. Bovine bone powder and a bone lamella without calcination, as well as calcined samples from 500 to 820 °C at 6 °C/min every 20 °C, were observed. A Hitachi SU8230 scanning electron microscope was used with 1.0 kV electron acceleration voltage. The samples were prepared in aluminum holders and fixed with alcohol-based colloidal graphite.

- **Structural characterization**
  - **HR-TEM**

Clean bovine bone powder was dispersed in an ultrasonic bath in isopropyl alcohol using an UP200Ht ultrasonic processor (Hielscher Ultrasonics GmbH) with a S26d7 sonotrode operated at 40 W of power and working frequency of 26 kHz for 15 min. 2 µL sample was taken and put on a copper grid coated with carbon film for further examination in a high-resolution transmission electron microscopy (HR-TEM). HR-TEM (JEOL ARM200F) microscope, operated at 200kV. Dark-field images were taken and analyzed with the Digital Micrograph software (Gatan). Fast Fourier Transform (FFT) was generated to study the crystalline structure. The determination of the crystal size (2D) was made using the Image J software.

  - ***In situ* HT-XRD**

1 g of defatted and deproteinized bovine bone powder (mesh 100) was densely packed in a platinum sample holder located into a controlled high-temperature devise, Ultima IV-Rigaku. Samples were analyzed through *in situ* HT-XRD test at 3, 6 and 9 °C/m in a Rigaku Ultima IV diffractometer, operating at 40 kV, 30 mA with CuKα radiation λ = 1.5406 Å. XRD patterns were obtained every 20 °C from 400 °C to 1100 °C during heating. Diffractograms were obtained from 5° to 80° on a 2θ scale with a step size of 0.02°.

Thermal expansion coefficient (TEC) was determined for each one of the three heating rates. The values of a and c lattice parameters were determined for every temperature using the 2θ position for (310) and (004) planes located at 39.81 and 53.14 for synthetic hydroxyapatite according to the ICCD card No. 00-009-0432. Linear TEC for *a* and *b* lattice parameters was found by employing the following equation:

$$\alpha_a = \frac{1}{a_i} * \frac{\Delta a}{\Delta T} \qquad \text{Eq. 3.1}$$

Where α_a is the thermal expansion in *a*, a_i is the lattice parameter at room temperature, Δa is the change in *a* value, and ΔT is the change of temperature; the same procedure was followed to determine αc. αa and αc were plotted as a function of the temperature. Moreover, the cell volume was also calculated considering a hexagonal lattice ($V=a^2c \sin 60°$).

- **PDF-4**

The effect of the crystallite size on the broadening peaks of the diffraction patterns was analized by a simulation conducted with the PDF-4 software, which requires crystallographic information of the phase from either a powder diffraction file (PDF) or a crystallographic information file (CIF). In this case, crystallographic information of hydroxyapatite was obtained from the ICCD card No. 00-009-0432.

- **Thermal analysis: DSC and TGA**

Thermogravimetric curves and calorimetric measurements of cleaned bovine bone powder were carried out in an STA 449 F3 Jupiter Netzsch equipment. 9.8 ± 1.0 mg of sample was put into an alumina crucible and heated from 500 to 900 °C at a heating rate of 6°C/min heating rate; measurements were carried out in a constant N2 (99.9%; Infra) flow.

CHAPTER 4

EFFECT OF THERMAL TREATMENTS AT HIGH HEATING RATES ON PHYSICOCHEMICAL PROPERTIES OF HAp FROM BOVINE BONE

The incineration process can be described in detail by using the thermal history carried out to obtain the sample. It is divided into four stages: heating rate temperature, annealing temperature, sintering time, and cooling process under determined atmospheric conditions. The heating rate has been reported from 2 to 200°C/min (Londoño-Restrepo *et al.*, 2016; Barakat *et al.*, 2009; Sobczak-Kupiec & Wzorek, 2012; Nasiri-Tabrizi *et al.*, 2014; Li *et al.*, 2016; Eslami *et al.*, 2017), the sintering time can be carried out from 0 to 50 h (Ramirez-Gutierrez *et al.*, 2017; Bahrololoom *et al.*, 2009; Herliansyah *et al.*, 2009) under different thermal annealing conditions that vary from 400 to 1400°C (Ooi *et al.*, 2007; Sofronia *et al.*, 2014). Finally, the cooling process can be through cooling or quenching (Bahrololoom *et al.*, 2009; Ramirez-Gutierrez *et al.*, 2016). Moreover, it is necessary to consider that the atmosphere in each one of these steps has a strong influence on the physicochemical properties of the BIO-HAp (Elliott, 2013; Nasiri-Tabrizi *et al.*, 2013).

Ooi *et al.* (2007), studied the effect of the annealing temperature from 400 to 1200 °C for bovine bone calcined with a heating and cooling rate of 5 °C/min. They reported that the annealing temperature enhanced the crystallinity, but the presence of $Ca_3(PO_4)_2$ was not detected until 1100 °C. They also affirmed that bovine bone annealed between 800 and 1000 °C has the same characteristics of a natural bone. However, Londoño-Restrepo *et al.* (2016) showed that for temperatures around 700 °C, the BIO-HAp suffers an order-disorder transition and for temperatures higher than this, BIO-HAp structure is a single microcrystal.

Figueiredo *et al.* (2010) studied the effect of the sintering temperature on the composition and microstructure of human and animal HAp. They reported no increase in the HAp crystallinity above 900 °C and the formation of other phases were not identified in the X-Ray diffractograms. At this point, it is important to note that BIO-HAp from mammalian bone is not a pure phase; BIO-HAp is accompanied by carbonates and phosphates. Also, crystalline changes continue happening above 900 °C like dehydroxylation of the sample (Londoño-Restrepo *et al.*, 2016).

In relation to the morphological changes that take place because of the different steps to obtain BIO-HAp, scanning electron microscopy has been used to detect changes in the porosity, as well as changes in the morphology (Giraldo-Betancur *et al.*, 2013; Londoño-Restrepo *et al.*, 2016; Ramirez-Gutierrez *et al.*, 2016). Joschek *et al.* (2000) analyzed porous hydroxyapatite from bovine bone (Endobon®) from Merck. This sample is an interconnected pore system with pore sizes from 0.1 to 500 μm and crystal sizes from 1 to 7 μm; the specific surface area is minimal in comparison to natural bone. Through a simple inspection of the SEM images shown in this work, it was found that the sample is a mix of cortical and trabecular bone that was calcined at a high annealing temperature. The crystal sizes reported were for cortical bone, and the pore sizes were for trabecular bone. Also, it is possible to say that the porosity in this sample has nonphysical sense. Londoño-Restrepo *et al.* (2016) reported morphological changes for hydroxyapatite from bovine bone calcined at two low heating rates: 2.5 and 5 °C/min. They showed that the apparition of micro-holes in the sample at 700 °C was due to organic phase decomposition, and irregular shapes and submicron sizes for hydroxyapatite crystallites.

The aim of this section is to determine the effect of the high heating rates used to obtain BIO-HAp by calcination of bovine bones on its physicochemical properties for five annealing temperatures: 700, 800, 900, 1000, and 1100 °C, and three different heating rates 7.4, 9.9, and 11.1 °C/min. Thermogravimetric and calorimetric analysis were carried out to study the endothermic and exothermic transitions in bone, and inductively coupled plasma was used to analyzed the changes in the mineral content as a function of the heating rate and annealing temperature. SEM images were used to study the changes in the morphology and crystallite size as a function of the thermal treatments, while the identification of crystalline structures in the studied samples as well as the determination of the FWHM parameter was done by X-Ray diffraction. Finally, the vibrational state of the samples was studied by Raman spectroscopy. Additional samples were carried out from 520 to 620 °C (every 20 °C) at 7.4 °C/min to understand some thermal transitions; these samples were analyzed by SEM and XRD.

4.1. Thermal changes

Different thermal events take place during powder bone calcination, and these events have a strong influence on the source used to obtain bio-hydroxyapatite as the composition of the analyzed sample can change due to the age of the animal or its diet. On the other hand, DSC and TGA thermograms depend on the heating rate that is directly associated with the heat capacity of the sample. This property is a ratio of calorific energy transferred and change in the temperature of the sample. Some fluctuations in the data can be found due to the heterogeneous composition of the sample that has a lot of crystalline phases and organic remains; these factors influence the heat capacity of the sample as it is an extensive property.

Figure 4.1 A, C, and E shows the mass loss as a function of the temperature and its first derivative and Figure 4.1 B, D, and F corresponds to DSC curve and its second derivative in order to determine maximum and minimum points. All thermograms and DSC curves were done for samples of powder bovine bone with hydrothermal process heated at three heating rates. Figure 4.1 A and B for samples heated at 7.4 °C/min; C and D for samples heated at 9.9 °C/min, and E and F for samples heated at 11.1 °C/min. In order to analyze these thermograms, the first and second derivative criteria were employed. These criteria allowed to separate the thermal events.

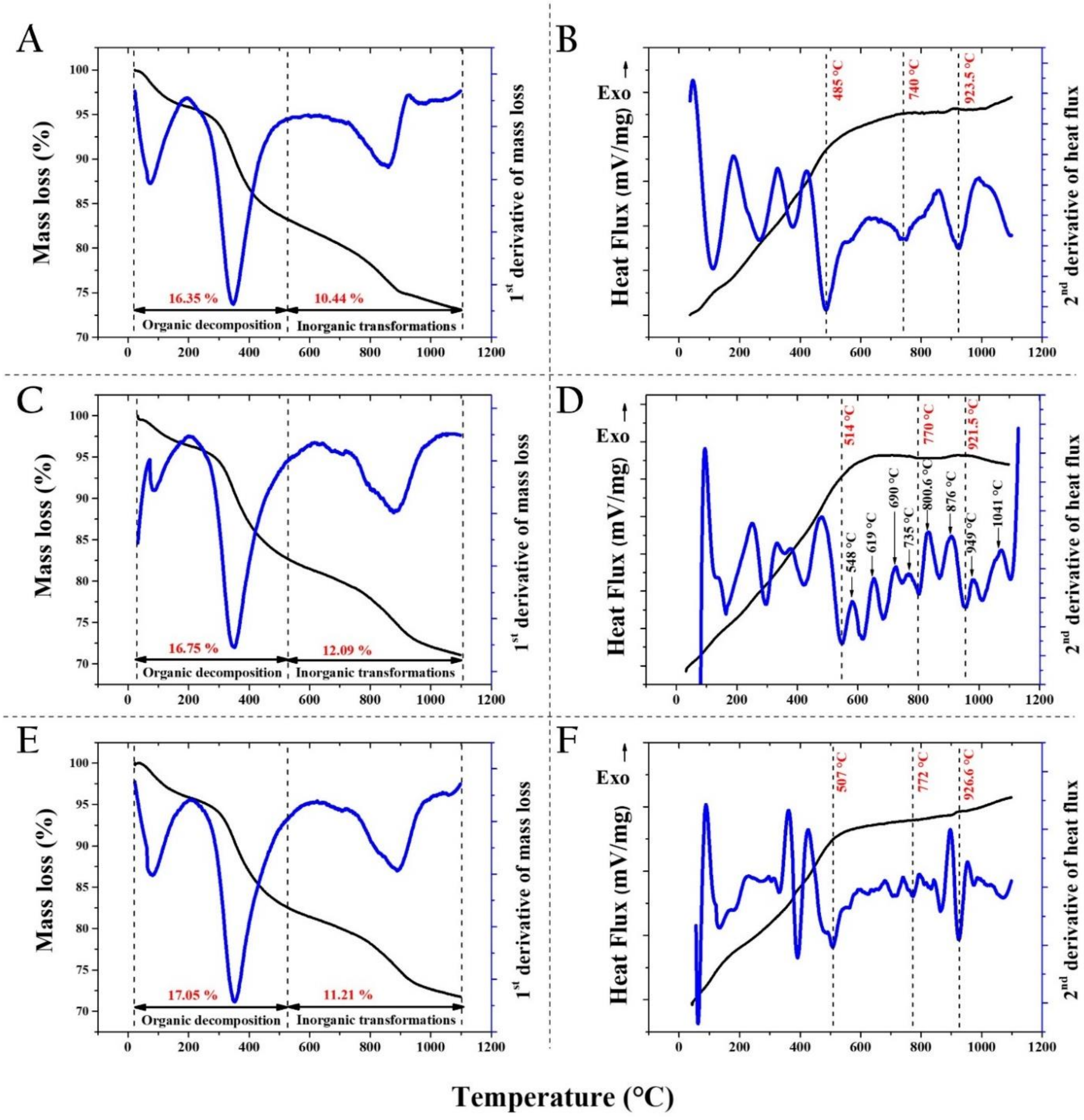

Figure 4. 1 (A), (C), and (E) shows TGA thermograms and DTA for the three heating rates (7.4, 9.9, and 11.1 °C/min) in growing order. (B), (D), and (F) shows DSC thermograms and its second derivative for the three heating rates in growing order.

From a mathematical point of view, if the slope of the first derivative is constant for a range of temperatures, then there are no changes in the sample, but if the slope changes, it means that some thermal events are taking place. The second derivative described if there are more events and it confirms the beginning and the end of the first change.

The thermal analysis graph by TGA was divided in two regions: region I (room temperature until 500 °C) is mainly associated with the organic decomposition and water loss, and region II for changes that take place in the hydroxyapatite. From TGA analysis, the organic mass loss for the three studied heating rates were 16.35, 16.75, and 17.05 %, respectively. According with DSC analysis, some endothermal peaks can be seen in this zone for organic decomposition and it is well known that these correspond to the adsorbed water liberation from room temperature to 120 °C, liberation of lattice water chemically bonded with the HAp lattice that was evidenced as a peak located about 200 °C; exothermal peaks indicate the fat and phospholipids degradation at about 330 °C, collagen and non-collagen proteins that were first denaturalized at 420 °C, and then their primary structures of amino-acids were broken (550 °C). This region is not relevant for the present study.

The second region from 500 to 1100 °C that is the focus of this research is important because it corresponds to the phase transition and phase formation of the inorganic compounds due to the heating rate and the annealing temperature. The mass losses for region II were 10.44, 12.09, and 11.21 %, respectively. For this region, some thermal events were identified: carbonate loss and hydroxyapatite transformation in a multi-step process by a dehydroxylation effect. Some authors have reported a whitlockite formation by reaction among calcium diphosphate ($Ca_2P_2O_7$) formed by decomposition of acid phosphate (HPO_4^{2-}) at about 250-400 °C (Eq. 4.1 and Eq. 4.2) that reacts with hydroxyapatite above 700 °C (Ishikawa *et al.*, 1993; Raynaud *et al.*, 2002; Tõnsuaadu *et al.*, 2012); then, an increase in whitlockite content is expected for the X-diffraction analysis.

$$2HPO_4^{2-} \longrightarrow P_2O_7^{4-} + H_2O \qquad Eq. 4.1$$

$$P_2O_7^{4-} + 2OH^- \longrightarrow 2PO_4^{3-} + H_2O \qquad Eq. 4.2$$

Hydroxyapatite can be dehydroxylated by effect of the high temperatures and it has been reported that this process starts at 860 °C and 900 °C in air (Sofronia *et al.*, 2014). For powder bovine bone with a hydrothermal process, the dehydroxylation process starts at 876 °C. In first place, oxy hydroxyapatite (OHAp, $Ca_{10}(PO_4)_6(OH)_{2-2x}O_xV_x$; where V is a vacant site) is formed. Then, if the heating process continues oxy hydroxyapatite changes to oxyapatite ($Ca_{10}(PO_4)_6O$) that is stable until 1050 °C (Raynaud *et al.*, 2002). This second step in the dehydroxylation process took place at 949 °C. Finally, oxyapatite was degraded at 1041 °C to a mix tetra-calcium phosphate ($Ca_4P_2O_9$) or TTCP, and tri-calcium phosphate ($Ca_3(PO_4)_2$) (Trębacz & Wójtowicz, 2005; Matsunaga & Murata, 2009) that is known as TCP or whitlockite.

4.2. Compositional Analysis: ICP

Figure 4.2 A shows the Ca content for powder bovine bone (BB), powder bovine bone with the hydrothermal process (BB-HP), sample calcined at 620 °C at 7.4 °C/min, and bio-hydroxyapatite calcined at three heating rates: 7.4, 9.9, and 11.1 °C/min for 700, 800, 900, 1000, and 1100 °C. For calcined samples, there is an apparent increase in the Ca content up to 620 °C that is associated with a concentration effect due to organic phase removal.

Figure 4.2 B shows the P content for the same samples, the apparent increase in concentration again is due to that the powder bovine bone lost some ions and compounds during the hydrothermal process, it means that this is a concentration effect. This effect is more evident when powder bovine bone with the hydrothermal process (BB-HT) is calcined at 620 °C and the most part of the organic phase is degraded. Figure 4.2 C corresponds to the Ca/P molar ratio and indicates that a non-stoichiometric hydroxyapatite was obtained using the incineration process, as it is expected because the studied samples are from a natural source and other substitutional ions are present. As the temperature increases until 1100 °C, Ca/P molar ratio decreases to 1.3. Another very important aspect to understand the mineral behaviors of the bone is to study the mineral content in the lyophilized fraction of the organic phase removed during the hydrothermal process.

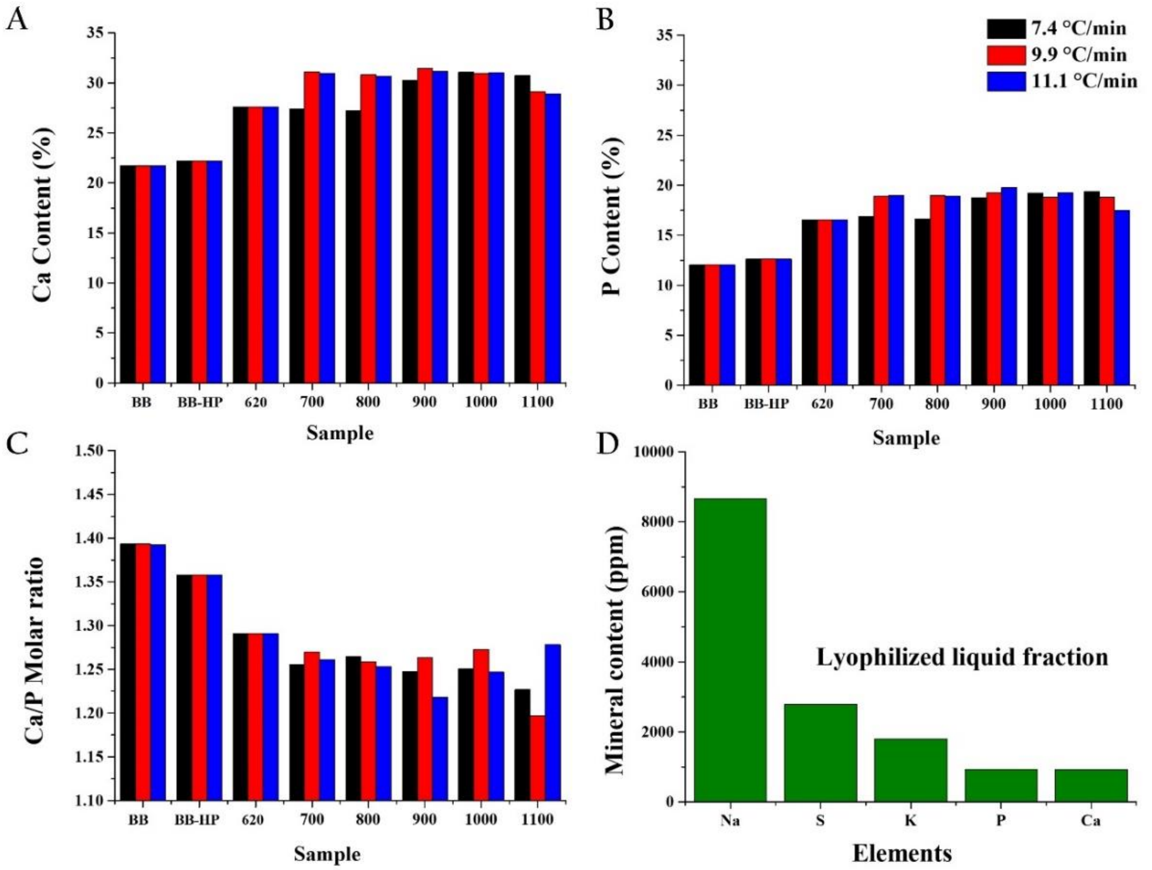

Figure 4. 2 Shows mineral percental content of (A) Ca, (B) P, and (C) its molar relation in powder bovine bone (BB), powder bovine bone with hydrothermal process (BB-HP), and BIO-HAp calcined at 620 °C (610) and from 700 to 1100 °C at the three heating rates (700-1100). (D) shows mineral content of the liquid fraction obtained from the hydrothermal process.

Figure 4.2 D shows the found elements in the lyophilized liquid fraction. Na, S, and K are the major components in this sample and correspond to the decrease in element contents during the cleaning process. These elements are associated with fat and proteins of the bone.

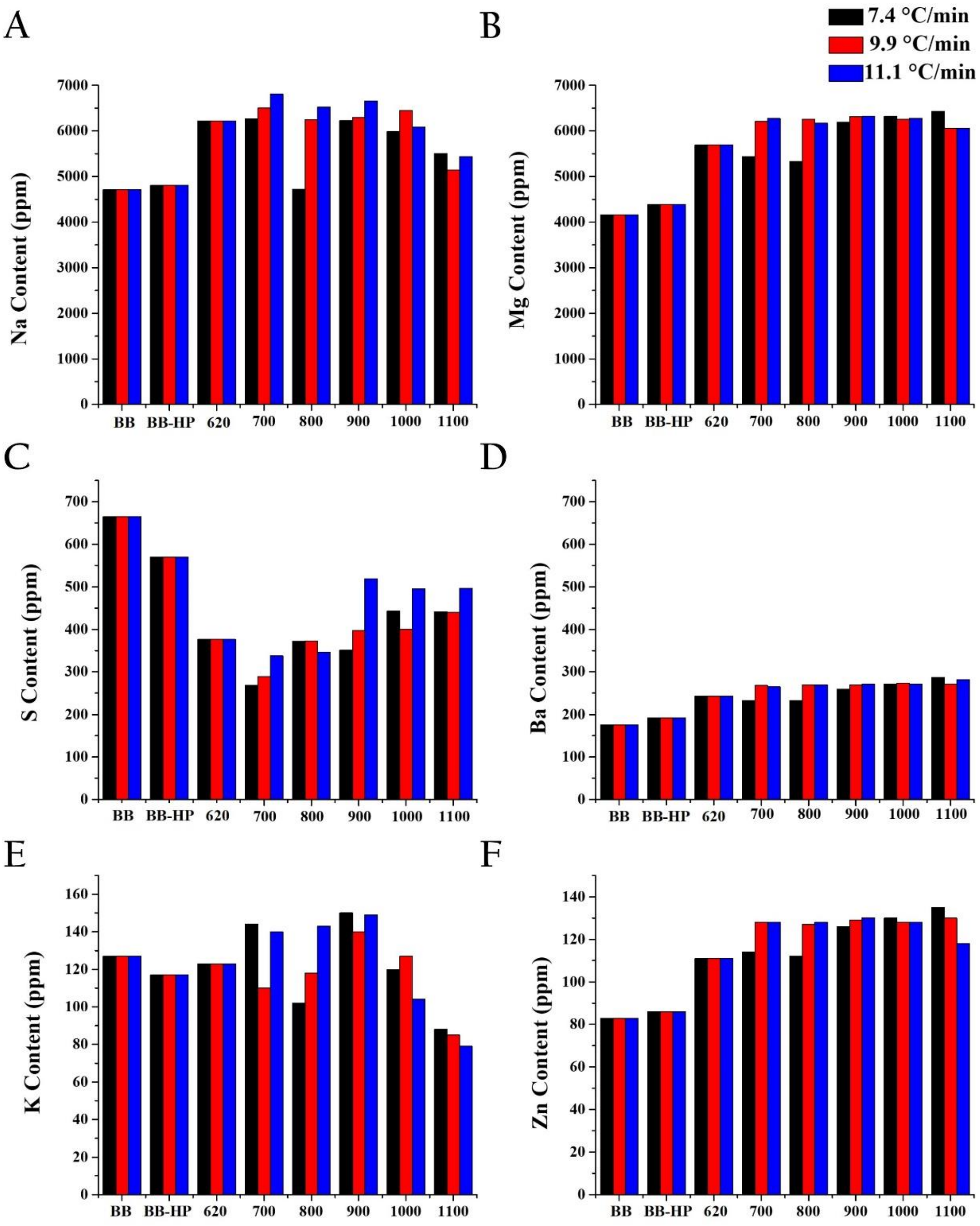

Figure 4. 3 Shows mineral content of minority elements (A) Na, (B) Mg, (C) S, (D) Ba, (E) K, and (F) Zn in powder bovine bone (BB), bovine bone with hydrothermal process (BB-HP), and BIO-HAp calcined at 620 °C (620) and from 700 to 1100 °C at the three heating rates (700-1100).

Figure 4.3 shows the mineral content for the majority substitutional ions found in BIO-HAp. Ions such as Na, Mg, Ba, and Zn had the same concentration effect that Ca and P, as it can be observed in Figure 4.2, these ions are mainly part of the inorganic phase. S and K contents show an opposite concentration effect, which is explain because these elements are mostly present in the organic phase as shows Figure 4.2 D. K ion has a different behavior from 900 to 1100 °C for all three heating rates in comparison to the other analyzed elements. It is possible to say that a potassium compound gets its melting point, but so far this was not identified.

Through ICP analysis, small amounts of Al, B, Co, Cr, Cu, Mn, Ni, Pb, Si, and Ti were found as well, but they were not quantified because these were below the detection limit.

4.3. Morphological studies: SEM

To understand DSC endothermal peaks at 548 and 619 °C (see Figure 4.1 D), samples were calcinated between 520 to 620 °C each 20 °C at 7.4 °C/min and were observed through SEM. Figure 4.4 shows SEM images for samples calcined from 520 to 620 °C every 20 °C. The system is an agglomeration of highly porous HAp crystallites of 10-90 nm length at 520 °C (see Figure 4.4 A). Due to the temperature rise, crystallites are bigger at 540 °C than at 520 °C, and the agglomeration observed at 520 °C has started to disappear (see Figure 4.4 B).

When the sample reached 560 °C, crystallites has the lowest contact among them; then it is a disintegration phenomenon where each crystallite is independent with a grain boundary well established (see Figure 4.4 C). At 580 °C grain boundary disappears, and crystallites start growing again by coalescence as is possible to see in Figure 4.4 D to F. Internal crystal reorganization, as well as a deagglomeration and orientation of crystallites could be the reason for the endothermic peak located at 548 °C in DSC curve. The second interesting peak located at 619 °C corresponds to coalescence phenomenon.

Figure 4.5 A, D, G, J, and M shows the BIO-HAp calcined at 700, 800, 900, 1000, and 1100 °C at 7.4 °C/min, respectively. Figure 4.5 B, E, H, K, and N corresponds to samples calcined at the same range of temperatures for the second heating rate of 9.9 °C/min. Finally, Figure 4.5 C, F, I, L, and O corresponds for samples heated at 11.1 °C/min. Samples calcined at 700 °C for the three heating rates have micrometric sizes in comparison to crystallites from the sample calcined at 620°C that has nanometric crystallites (see Figure 4.4 F). The crystallite morphology changes as temperature does. The system morphology starts as spheres (700 °C), next irregular spheres (800 °C), then hexagonal bars (900 °C), and finally, irregular big spheres (1000 and 1100 °C). Small spheres can be seen in the micrographics at 800 °C for the three heating rates. Some weakly bonded ions go out of bio-hydroxyapatite lattice and react with the oxygen from the air to form oxides. These spheres correspond to magnesium oxide as it was reported by Ramirez-Gutierrez *et al.* (2017).

Table 4.1 shows ranges for crystallite size that were measured in the longitudinal direction. For samples calcined at 700°C and different heating rates, the crystal size range of the grains increases as the heating rate increased. The crystal size grows up as the annealing temperature increases from 700 to 1100 °C. It is remarkable that the crystallite growth has a preferential direction and that rods are all oriented as can be seen in Figure 4.5 G and I.

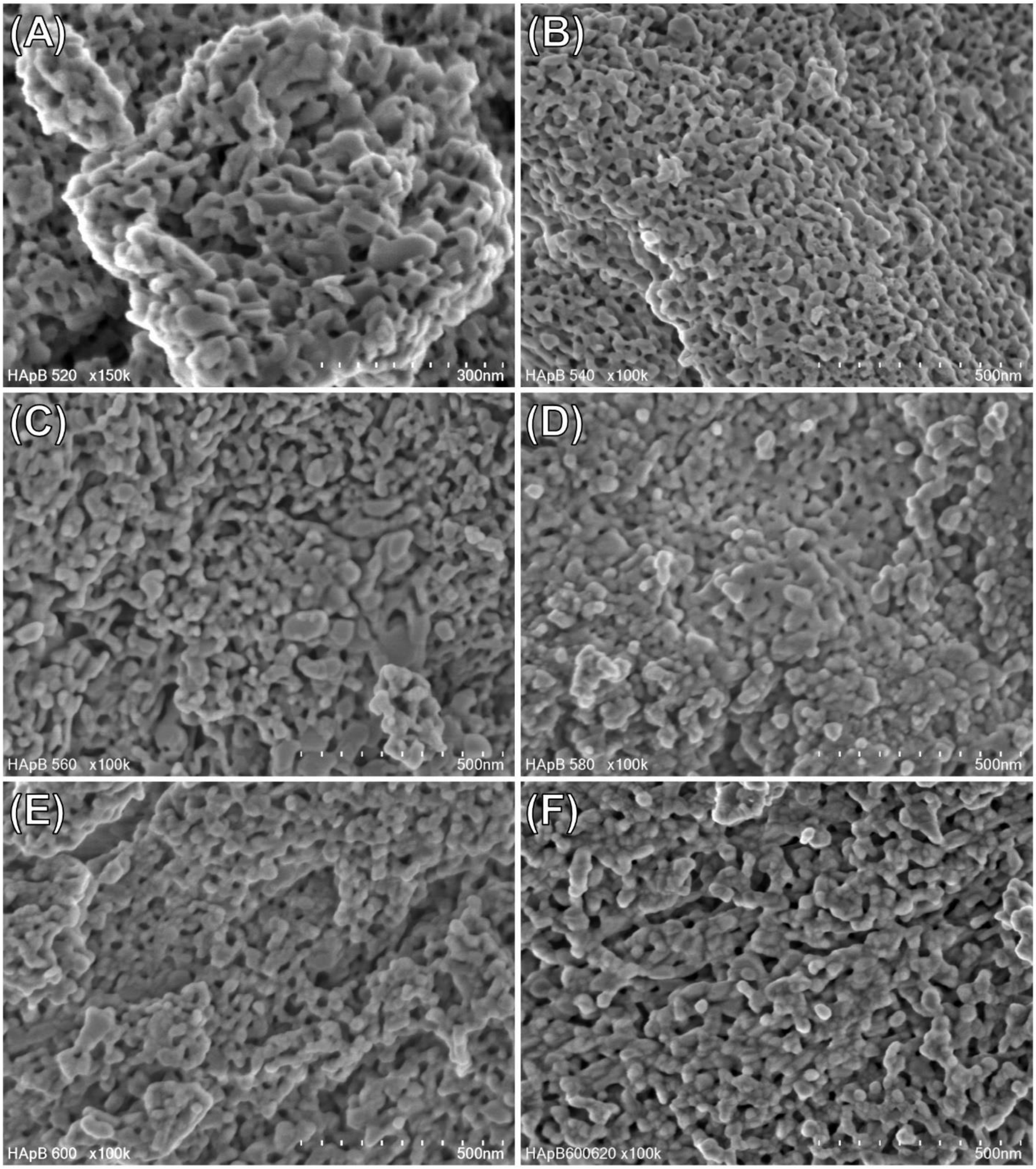

Figure 4. 4 (A) to (F) shows High Resolution SEM images at 100,000× for samples calcined from 520 to 620 °C each 20 °C in growing order at 7.4 °C/min.

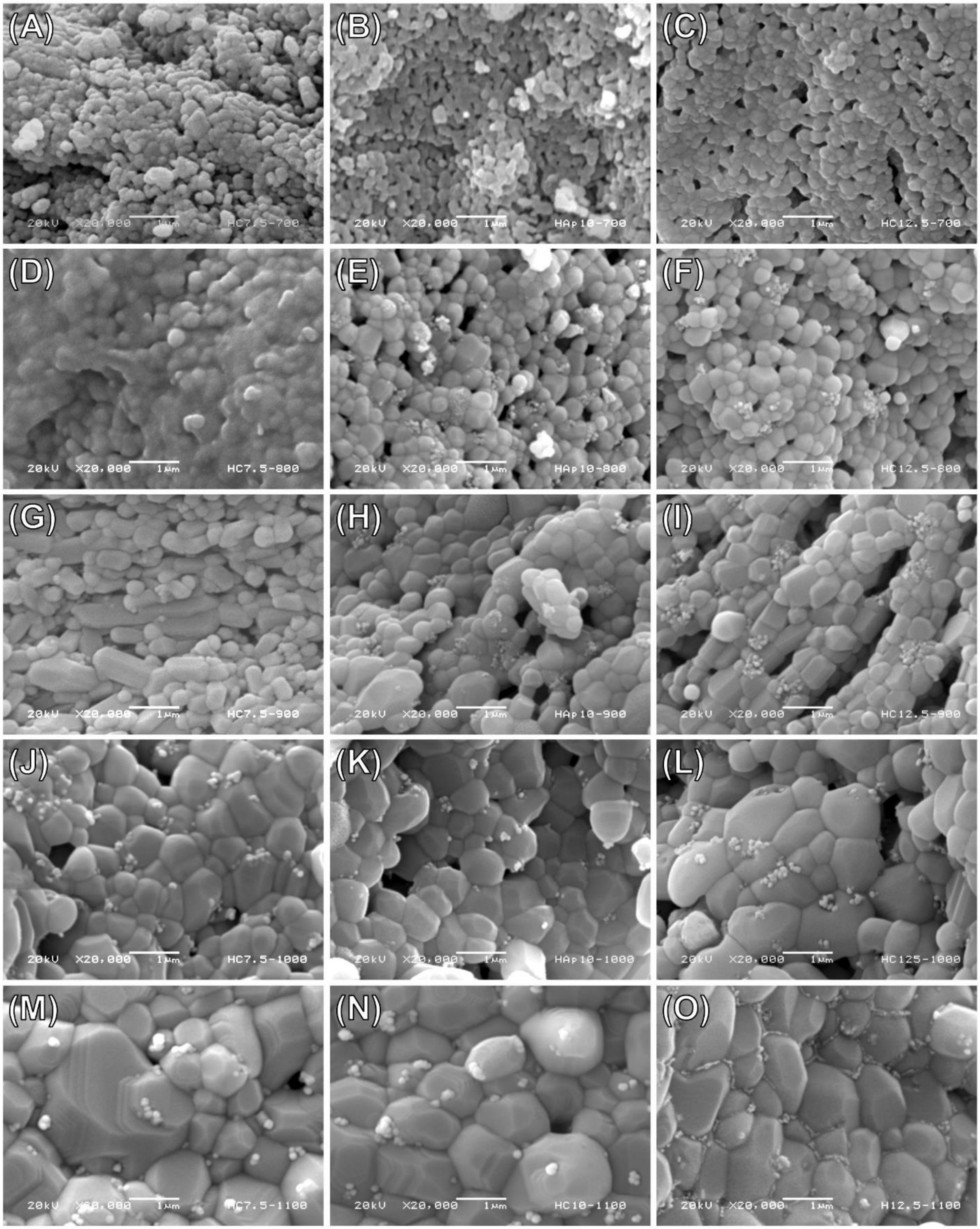

Figure 4. 5 SEM images at 20,000× of bovine bone calcined at 7.4 °C/min from 700 to 1100 °C (A, D, G, J, and M). Samples calcined at 9.9 °C/min from 700 to 1100 °C (B, E, H, K, and N). Samples calcined at 11.1 °C/min from 700 to 1100 °C (C, F, I, L, and O).

Table 4. 1 Crystallite size in function of temperature and heating rate.

Heat. Rate / Temp. (°C)	7.4 °C/min		9.9 °C/min		11.1 °C/min	
	CS (µm)	PS (nm)	CS (µm)	PS (nm)	CS (µm)	PS (nm)
700	0.10-0.20	100-320	0.13-0.26	60-180	0.2-0.36	40-140
800	0.16-0.44	50-230	0.25-0.56	50-140	0.32-0.69	50-110
900	0.29-1.26	40-120	0.40-1.05	40-150	0.63-1.01	40-110
1000	0.50-1.44	80-240	0.40-1.31	90-340	0.67-1.69	120-350
1100	1.06-2.87	130-480	0.48-2.99	170-290	0.78-1.79	230-320

4.4. Structural changes: crystalline phases

X-ray diffraction is an excellent technique to identify crystalline phases in a material. Figure 4.6 A shows the X-ray diffractograms for powder bovine bone (BB), powder bovine bone with hydrothermal process (BB-HP), and BIO-HAp which was calcined at 620 °C to remove the organic material. For these samples, all peaks increased their intensity. In BB and BB-HP samples, some broad peaks were identified as HAp and three peaks that correspond to calcium carbonate were identified such as (104), $(11\bar{3})$, and $(11\bar{6})$, located at 2θ = 29.26, 39.41, and 48.46°, respectively.

Figure 4.6 B shows the characteristic diffractograms for samples calcined from 700 to 1100 °C at 11.1 °C/min, in growing order. All peaks for hydroxyapatite (HAp) were associated with the Joint Committee on Powder Diffraction Standards (JCPDS) card No. 84-1998. The cards used for some interesting phases for this study were: No. 09-0169 for Whitlockite (*), No. 47-1743 for $CaCO_3$, No. 77-2364 for MgO (o), No. 76-1456 for $NaCaPO_4$ (▪), No. 70-1381 for $Ca(H_2PO_4)_2$, No. 09-0080 for $CaPO_3(OH)$, and card No. 25-1137 for $Ca_4O(PO_4)_2$.
All calcined samples from 700 to 1100 °C at 7.4, 9.9, and 11.1 °C/min have the characteristic peaks for hydroxyapatite, but other peaks did not correspond with HAp. Some of these phases are present in mammalian bones in smaller quantities such as calcium carbonate ($CaCO_3$), calcium phosphate ($Ca_3(PO_4)_2$; TCP), calcium hydrogen phosphate ($Ca(H_2PO_4)_2$; MCP), and di calcium phosphate ($CaPO_3(OH)$; DCP) (Vallet-Regí & González-Calbet, 2004).

It is well known that HAp, MCP, DCP, and TCP are phosphate phases which are present in the bone in natural way, but other compounds were formed during the calcination process. In all calcined samples HAp, $NaCaPO_4$, $Ca_3(PO_4)_2$, and MgO were found. Other phases were identified and showed in Table 4.2; among formed compounds during the calcination process there are MgO, $Ca(OH)_2$, and $Ca_4O(PO_4)_2$. MgO peaks are located at 2θ = 42.94, 62.33, and 78.68° that correspond to (200), (220), and (222) directions, and as it was showed in Fig. 6, it appears as small spheres with diameters of about 0.1 µm.

Full width at half maximum (FWHM) was determined for samples from 500 to 1100 °C (at 7.4°C/min) using a single peak of hydroxyapatite (002), and from 700 to 1100 for 9.9 and 11.1 °C/min. Scherrer parameter was not used to determine crystallite size because there is a disorder-order transition at about 620 °C that changes the system from polycrystalline to monocrystalline, and calculating the mean size for crystallites higher than 0.1 μm has no physical sense.

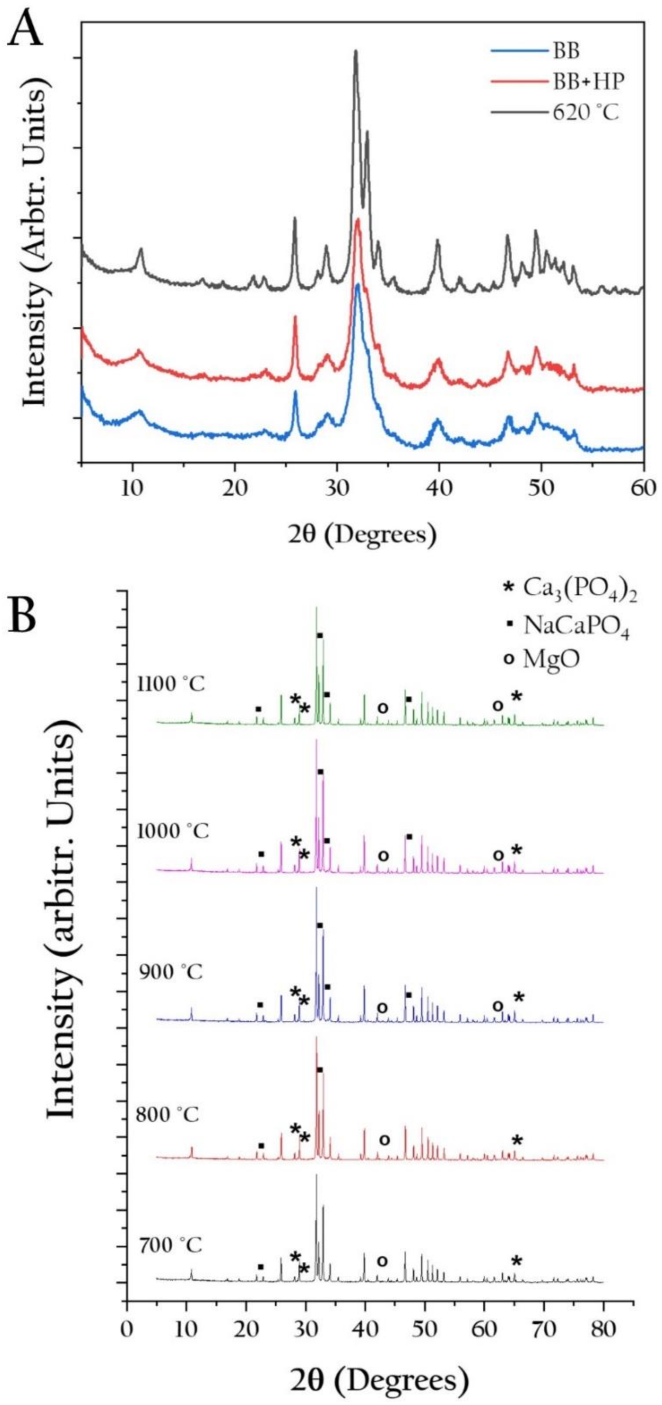

Figure 4. 6 (A) Diffractograms for powder bovine bone (BB), powder bovine bone with hydrothermal process (BB-HP), and BIO-HAp calcined at 620 °C. (B) Diffractograms of samples calcined from 700 to 1100 °C at 11.1 °C/min with some identified mineral phases different to HAp.

Table 4. 2 Additional phases found by XRD as a function of the temperature and heating rate.

Temp. (°C)	Heating rate (°C/min)	Other phases
700	7.4	$CaCO_3$
	9.9	$CaCO_3$
	11.1	$CaCO_3$; $CaPO_3(OH)$
800	7.4	$CaCO_3$
	9.9	$CaCO_3$
	11.1	$Ca_4O(PO_4)_2$; $CaPO_3(OH)$
900	7.4	-
	9.9	$Ca_4O(PO_4)_2$; $CaPO_3(OH)$
	11.1	$Ca_4O(PO_4)_2$; $CaPO_3(OH)$
1000	7.4	$Ca(H_2PO_4)_2$; $Ca_4O(PO_4)_2$; $CaPO_3(OH)$
	9.9	$Ca(H_2PO_4)_2$
	11.1	$Ca(H_2PO_4)_2$; $Ca_4O(PO_4)_2$; $CaPO_3(OH)$
1100	7.4	$Ca(H_2PO_4)_2$; $CaPO_3(OH)$
	9.9	$Ca(H_2PO_4)_2$; $CaPO_3(OH)$
	11.1	$Ca(H_2PO_4)_2$; $Ca_4O(PO_4)_2$; $CaPO_3(OH)$

Figure 4.7 A shows the FWHM for (002) peak located at 2θ =25.9° as a function of the temperature for powder bovine bone (BB), powder bovine bone with hydrothermal process (BB-HP) and BIO-HAP calcined from 520 to 1100 °C at 7.4 °C/min as well as samples calcined from 700 to 1100 °C at 9.9, 11.1°C/min. Figure 4.7 B shows the second derivative that allows the determination of the main changes in the FWHM parameter as a function of the temperature.

The FWHM as a function of the temperature as well as the second derivative curve of FWHM were divided in 4 regions. The first region corresponds to the cleaning process where most of the organic phase was removed of the bone matrix. In this case, FWHM decreases as a result of the elimination of the contribution of the organic component. The second region is for samples calcined from 520 to 700 °C where the system is composed of hydroxyapatite nanocrystals as it was shown in SEM analysis. It is possible to see that FWHM decreases due to the increase of the crystal quality of nano-crystals reordering lite growing. In region III (700-900 °C), samples are composed of micro-crystals of carbonated and calcium deficient hydroxyapatite. Finally, region IV (900-1100 °C) corresponds to the dehydroxylation process. An increase in FWHM was expected because of the loss of hydroxyl group, but FWHM does not have changes in this region as can be seen in Figure 4.7 B for the same region. It could be because dehydroxylation process is slow at these temperatures and due to re-hydroxylation by interaction of the sample with the air.

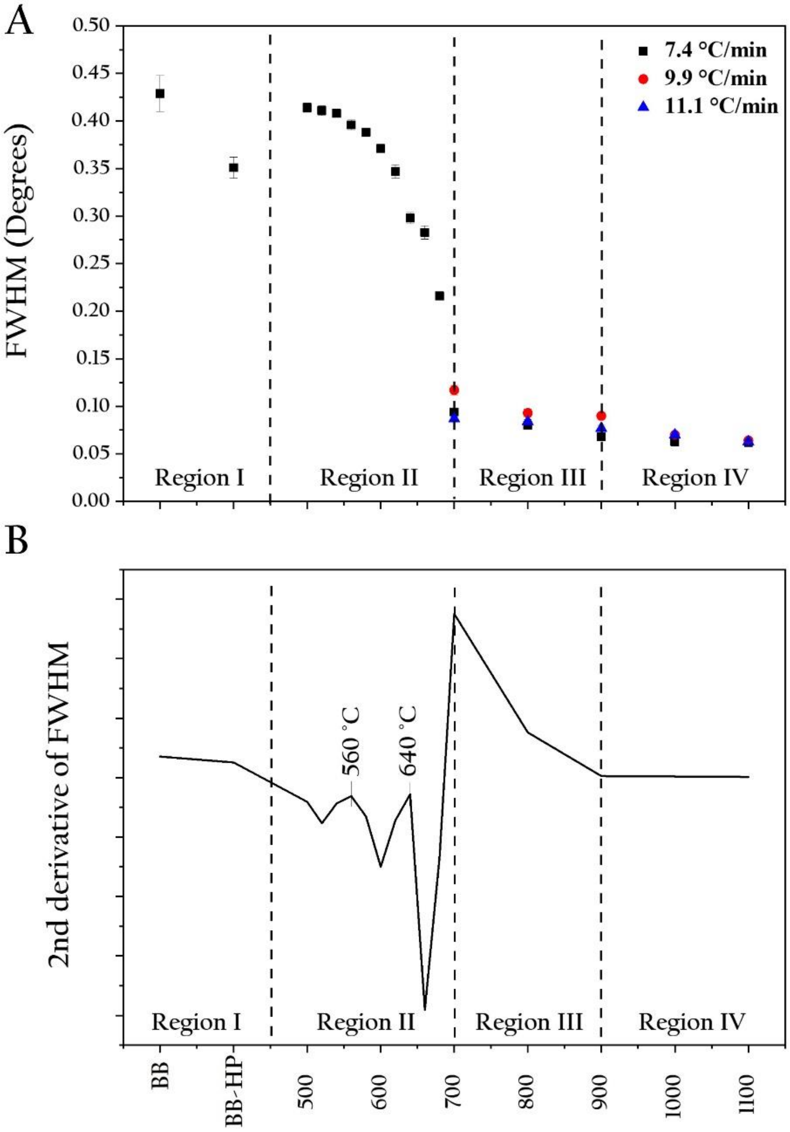

Figure 4. 7 (A) Full width at half maximum (FWHM) for (002) peak as a function of the temperature and heating rate. (B) second derivative of the FWHM as a function of the temperature.

4.5. Vibrational Spectroscopy: Raman

The Raman bands for bovine bone powder, bovine bone powder with hydrothermal process, and sample calcined at 620 °C were shown in a previous publication (Londoño-Restrepo *et al.*, 2016). It was clear that the hydrothermal process contributed to the organic phase removal. Although a calcination process was realized to disintegrate the remaining organic phase, some ashes and amide I and III were found in the sample; this fact is due to low sintering time of 3 hours, so the sample shows a gray color (Ramirez-Gutierrez *et al.*, 2017). All samples exhibit only the four internal vibration modes of phosphate group (PO_4^{3-}) at 430, 588, 960, and 1070 cm^{-1} for υ_2, υ_4, υ_1, and υ_3 modes, and they have bands for the O-H stretching (Figure 4.8).

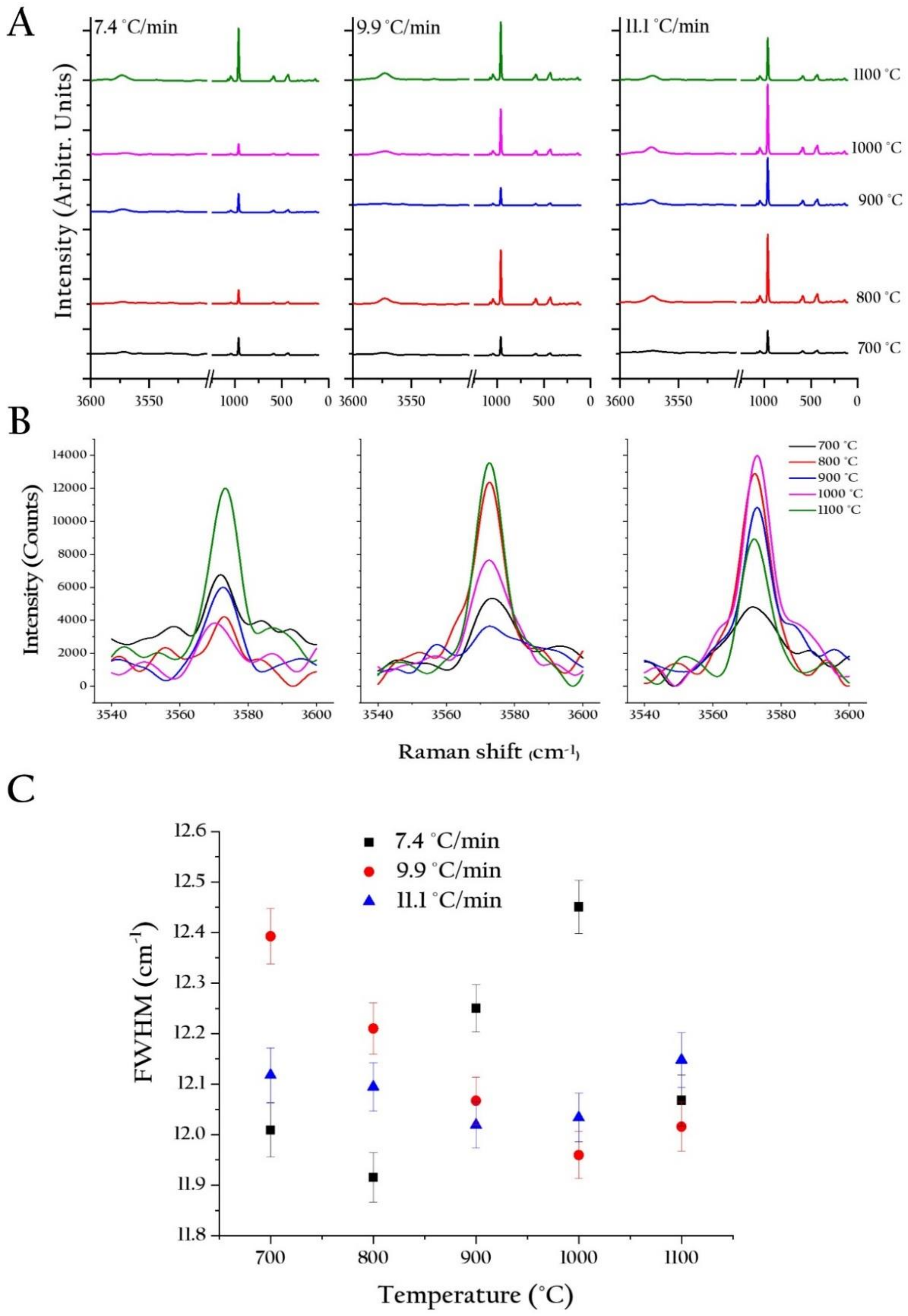

Figure 4. 8 (A) shows Raman spectrum for samples calcined from 700 to 1100 °C at the three heating rates. (B) O-H peak for BIO-HAp samples obtained from powder bovine bone. (C) Full width at half maximum (FWHM) for PO_4^{3-} band at 960 cm^{-1}.

4.6. Discussion

The organic mass loss percentages to the three heating rates indicate a similar organic content in the powder bovine bone used for the thermal curves. For DSC curves, there are fluctuations on the position of the peak temperature for thermal events that are related to its strong dependence on the heat capacity of the mineral compounds in the sample (Tõnsuaadu *et al.*, 2012). It is important to remember that biological apatites from mammalian bones are carbonated ($Ca_{10}(PO_4)_6(OH)_{2-2x}(CO_3)_x$). Carbonate group loss has been reported at 835 °C for a synthetic HAp heated at 10°C/min (Sofronia *et al.*, 2014), but this endothermal event happens at 800.6 °C when the BIO-HAp is calcined at 9.9 °C/min. Also, the resolution of the DSC depends on the heating rate, in our case, 9.9 °C/min gave a better resolved peaks than the others two heating rates. The phases and structural transformation of the inorganic compounds of the bone during calcination are still an open issue, due to the high complexity of the sample that has multiple compounds interacting with each other and with the atmosphere. Thus, some thermal events have not been well identified. DSC realized at 9.9°C/min also allowed to see well-resolved peaks at 548, 619, 690, and 735 °C, some of them in special for the 500 to 800 °C have not been elucidated. For this reason, we focused our attention for the first two peaks located at: 548 and 619 °C. Samples were obtained in the temperature range from 520 to 620 °C at 7.4 °C/min, without sintering time, and cooled in furnace air.

Ca content calculated by ICP indicates that BIO-HAp from bovine bone is a Ca deficient apatite, this kind of apatite has HPO_4^{2-} (Trombe & Montel, 1978), then, it is possible that thermal events related to Eq. 4.1 and Eq. 4.2 happen during calcination. As it was shown in the thermal analysis, carbonate hydroxyapatite has structural changes due to the dehydroxylation process; this change in the phase influences the Ca/P molar ratio. This low ratio at the end of the process indicates that dehydroxylation process produce a phase transition of HAp to tricalcium phosphate happened as it can be seen in the calorimetric analysis. According to Gross & Berndt (1998), a decrease in Ca/P molar ratio can be associated to the dehydroxylation process. At this point, it is important to note that although Ca/P molar ratio decreases at high temperatures, samples still have substitutional ions that are important to the osteogenesis process. The ionic radii of Na and Mg are very close to Ca value, then it is possible that these ions are offsetting the deficient calcium content in the lattice. Matsunaga & Murata (2009) reported Na and Mg are the mainly substitutional cations in human enamels and bones (0.5-1 %). Na and Mg content in BIO-HAp from bovine bone is like the human (0.45-0.65%; see Figure 4.3), then, from a compositional point of view this kind of bone is a good candidate to obtain hydroxyapatite for medical applications.

The changing morphology of the samples observed by SEM is influenced by the coalescence phenomenon, the out-diffusion process of Mg ion, and the dehydroxylation process. In terms of the heating rate, the crystallite growth for samples calcined at 11.1 °C/min is bigger than for the others two rates. It can be explained in terms of the energy given to the system. First, powder bovine bone used the thermal energy to break bonds and in consequence eliminates the organic phase. As the sample continues receiving energy, it tries to achieve its more stable state and starts to expel the substitutional and interstitial ions that make the network non-stoichiometric. Some carbonate compounds were lost at about 800-900 °C as seen in the thermal analysis (DSC-TGA) and the content studied by ICP. Regarding the porosity that is widely mentioned in most publications about BIO-HAp calcined at temperatures above 700 °C, it is important to mention that these samples do not have interconnected porous because of the micrometric size of the crystallites.

When powder bovine bone with hydrothermal process was calcined at 620 °C, some of its components were removed (organic phase), and hydroxyapatite diffracted peaks could be more easily seen due to the concentration effect that was mentioned in the ICP-OES analysis section. Calcium carbonate peaks are still at 620 °C, but some of them are overlapped with hydroxyapatite broad peaks. As it was showed in the SEM analysis for BB, BB-HP and samples calcined from 520 to 620°C, bone is formed by nanocrystal of HAp forming small cumuli of polycrystalline BIO-HAp. The X-ray analysis of the changes of this parameter indicates that for nano-particles the X-ray scattering produce broad peaks while in the case of micro crystal the scattering decrease and arrow peaks appear. The melting point for magnesium is 650 °C and for temperatures close to this one, Mg exhibits an out-diffusion process and when it has contact with the oxygen from the air, it forms MgO. This phenomenon had been observed for low heating rates, too (Londoño-Restrepo *et al.*, 2016). For $Ca(OH)_2$, it was a similar case. $Ca_4O(PO_4)_2$ that appeared at high temperatures (1100 °C) was formed due to the dehydroxylation process of hydroxyapatite. The formation of new phases above 400 °C in bio-hydroxyapatite samples have been reported; some of these phases are β-TCP, $NaCaPO_4$, NaCl, and KCl (Raynaud *et al.*, 2002). However, according to our analysis for all X-ray diffraction patterns, NaCl and KCl phases were not found. Based on thermal analysis there are at least three reactions that produce a decrease in the FWHM value: (1) Mg out diffusion and formation of MgO, (2) decarbonatization of the sample, and (3) formation of whitlockite. All of them happen from ions that are as substitutional components in the lattice, and when these ions leave the BIO-HAp lattice, it improves its internal order and its crystalline quality. In relation to thermal events located at 548 and 619 °C in DSC thermogram, the second derivative curve shows peaks close to these temperatures that corresponds to FWHM decreases (re-crystallization process). It is possible that these thermal events are correlated with structural changes in the lattice as it was proposed in SEM analysis.

4.7. Conclusions

All calcined samples from 700 to 1100 °C at the three high heating rates are composed only by inorganic phase. Genetic material, proteins, and fat were completely removed from the samples. Furthermore, secondary ions content does not have significant variations during the heating process from 700 to 1100 °C at the three heating rates.

Heating rate influences the thermal events of the DSC and TGA thermograms, for samples studied in this work, 9.9 °C/min shows an optimal resolution of each thermal event present during the calcination process. Some of these peaks are not yet elucidated; it is recommended that a detailed analysis with a smaller spacing of temperature be realized as was made among 520 to 620 °C. Heating rate influences on crystallite growth directly, so at higher heating rates, crystallites reach a bigger size before than with smaller heating rates, as it was the case for BIO-HAp from bovine bone calcined at 2.5 and 5°C/min whose results were analyzed and reported in a previous research (Londoño-Restrepo *et al.*, 2016). Regarding to crystallite size, two regions can be find:

nanocrystals from room temperature until 700 °C, and microcrystals from 720 °C. Moreover, high heating rates promote the formation of secondary phases as MgO and $Ca_4O(PO_4)_2$. Annealing temperature had a similar effect on the above mentioned physicochemical properties, it means as temperature increases, crystallites growth and the dehydroxylation process occurs forming new compounds in the sample. For samples calcined above 700 °C, porosity term has no sense, since the systems are big crystallites without interconnections between them. Due to this fact, these kinds of samples are not recommended to use in medical field.

Coalescence is the mechanism of how crystallites growth during calcination process; it provides the necessary energy to the formation of new bonds among them. While a crystallite is a nucleation center, others around it are rolled to form lamellae that are bonded with it forming each face of the hexagonal rods. At the starting temperature for the physicochemical characterization, crystallites were already grown, so it is important to analyze in detail what is happening with the inorganic phase from room temperature to 700 °C.

CHAPTER 5

STUDY OF TRABECULAR BOVINE BONES

Regarding clinical applications of spongy bone, two different routes to obtain hydroxyapatite have been established. The first one uses natural sponges from mammalian bones, and the second one is related to the development of scaffolds with different porosities based on synthetic materials in which an architectonic similarity with the natural 3D-sponges are expected, but this has not been possible yet because so far it is not possible to manipulate a preferred orientation and the micro-architecture to reproduce the mechanical and functional properties of the spongy bone. Furthermore, the chemical composition of synthetic scaffolds does not include substitutional ions such as Mg, Al, Ba, Cu, Fe, K, Mn, Zn, and Na that are present in the natural spongy bone (Giraldo-Betancur *et al*., 2013). In relation to mechanical properties, Lindahl (1976) studied trabecular bone obtained from human vertebrae and tibias. They reported a deterioration of the mechanical properties as a function of the age in the uniaxial force parallel to the bone. However, it has not been reported a detailed study of the mechanical properties of mammalian bones as a function of the direction. The chemical composition, quantity, and trabeculae orientation govern the mechanical properties of the sponge. This means that the mechanical properties change as a function of the position and direction of the trabeculae within the bone. Giesen *et al*. (2001) studied the mechanical properties for two loading directions. One direction coincided with the axial loading, and the other one was a direction perpendicular to the transverse loading. However, transversal loading has two different components. According to their study, the differences in the mechanical properties as well as its anisotropy can be considered as a mechanical adaptation to the loading. The crystalline structure of the bone is another important topic, in relation to the phase identification, this study can be carried out by using powders to identified crystalline phases (Londoño-Restrepo *et al*., 2016) or with the use of a small piece to identified preferential orientation of the bone. To sum up, materials for guided bone regeneration are not based on a depth study of the physicochemical properties of mammalian bones to emulate their characteristics thus, it is pretty

This part of the work is focused on the study of the physicochemical properties of bovine bone and hydroxyapatite the as well as morphological, structural, vibrational, and mechanical properties of defatted natural sponges from trabecular bone. This study was carried out taking into account three different sponge planes: XY, YZ, and XZ, about an XYZ coordinate system that was located in the femur head. The Morphology of a bone sponge was studied by using a Scanning Electron Microscopy (SEM), and the macro morphology of the sponge was analyzed using an X-ray tomography unit that allowed the porosity determination. Results showed that the micro-architecture of the sponge depends on the orientation while X-ray diffraction revealed that this trabecular bone is mainly formed by polycrystalline hydroxyapatite Z-oriented and calcium carbonate.

5.1. Thermal analysis

Figure 5.1 shows the thermal behavior of the bone powder with fat and protein and its second derivative as a function of the temperature with a 5 °C/min heating rate. The second derivative gives information about local minimums of a function, and this criterion is used to determine the position of some peaks which represent the transformations that take place in the bone during the calcination process. This thermogram is divided into two regions, the first one for temperatures below 650 °C that are associated with thermal changes due to the degradation of the organic matrix, and for temperatures up to 650 °C whose changes are associated directly to the inorganic phase. Changes in the mass below 100 °C correspond to the loss of free water, and the change from 100 to 220 °C is associated to loss of linked water (Londoño-Restrepo *et al*., 2016; Heredia *et al*., 2013; Peters *et al*., 2000; Sofronia *et al*., 2014). According to Lozano *et al*. (2003), the changes in the mass loss between 220 and 570 °C correspond to the degradation and combustion processes of collagen.

Six peaks were identified in the second region for the inorganic phase. Here, it is worth noting that the peak assignation of the thermal events for the inorganic phase is still controversial. However, peaks labeled as a, b, c, d, e, and f that are located at 690, 770, 870, 920, 960, and 1120 °C respectively, can be associated with the following bone transformation: the peak located at 690 °C (peak a) can be related to an exothermic process that takes place because of the recrystallization process of the HAp polycrystals. After, 700 °C some transformations of the mineral phase take place: carbonate loss and a dehydroxylation process where carbonate biohydroxyapatite becomes oxyapatite. Based on this information, it is possible to assign peak b (see Figure 5.1) an endothermic process that takes place as a result of the recrystallization process of the HAp polycrystals, peak c to the decomposition of carbonates, and peaks d to f to the multi-step BIO-HAp dehydroxylation process that turns HAp into OHAp. A more complete assignation of the peaks is shown in Table 5.1.

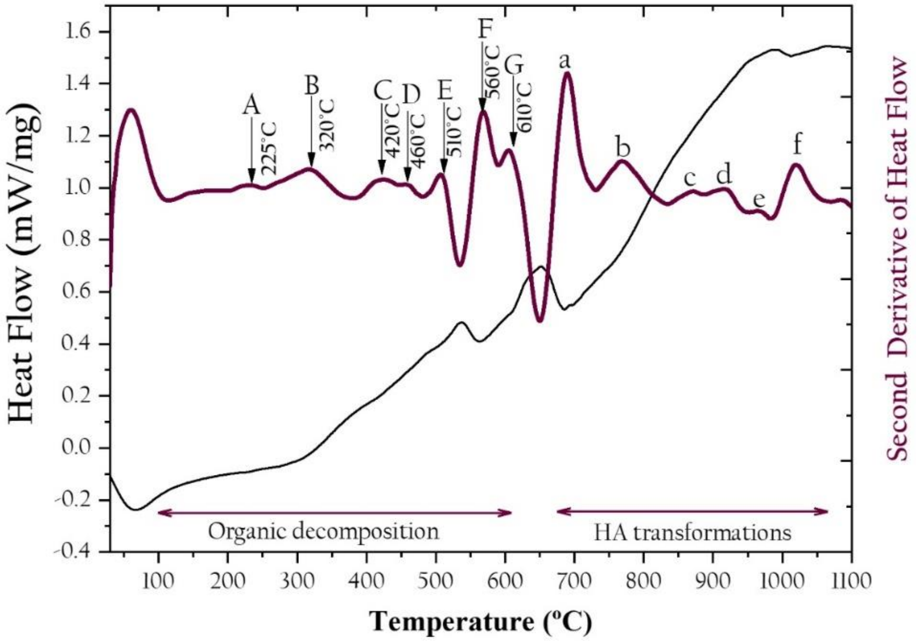

Figure 5. 1 **DSC and second derivative of the bovine bone powder.**

5.2 Vibrational properties

Figure 5.2 shows the Raman spectrum for the defatted spongy bone. Spongy bone exhibits typical bands of the phosphate group (PO_4^{3-}) that belong to hydroxyapatite, but other phases as carbonate are present too. In addition, there are bands for collagen as amide I, amide III, proline, and hydroxyproline. All bone components are summarized in Table 5.2 where it is clear that genetic material and fatty compounds are still present.

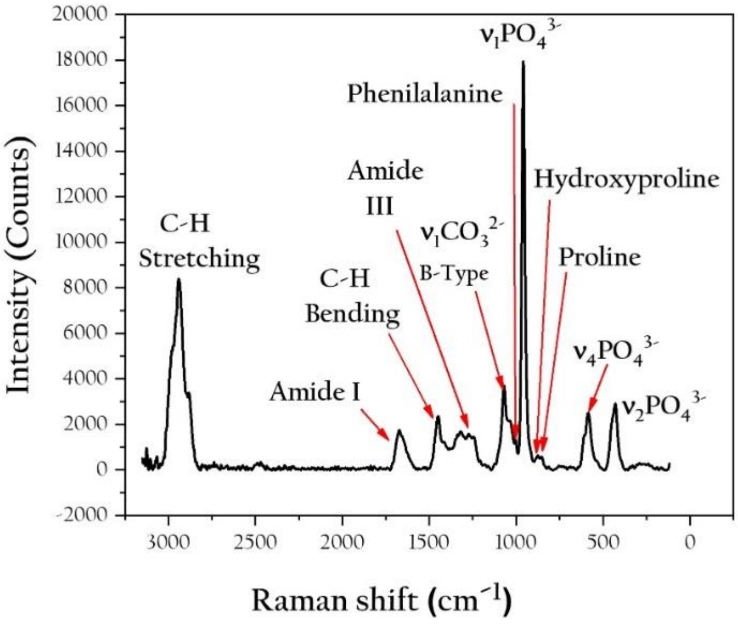

Figure 5. 2 **Raman spectra of trabecular bone.**

Table 5. 1 Thermal events during bone calcination.

Temperature (˚C)	Thermal event	Reference
-200-290	Collagen denaturation and decomposition.	Trębacz & Wójtowicz, 2005
622	Dissociation of calcium carbonate.	Kusrini & Sontang, 2012
800-1000	Partial dehydration of hydroxyapatite.	
345, 425 (exothermic	Collagen degradation and combustion.	Heredia et al., 2013
900-1000	Removal of remaining of organic components	Niakan et al., 2015
217-665	Liberation of chemically bonded water, decomposition of the organic matrix and carbonates.	Sofronia et al., 2014
835 (700-1100)	Decarbonization.	
988	Decarboxylation.	
1050	Decomposition Oxyapatite to calcium phosphate.	
1100	Decomposition HAp→βTCP→αTCP	
25-120	Adsorbed water liberation	Londoño-Restrepo et al., 2018
200	Lattice water liberation	
250-400	HPO_4^{2-} decomposition	
330	Phospholipids degradation	
420	Protein denaturalization	
550	¨Degradation of the primary protein structure	
700	Whitlockite formation	
876 and 949	$Ca_{10}(PO_4)_6OH \rightarrow Ca_{10}(PO_4)_6O$	
1041	$Ca_{10}(PO_4)_6O \rightarrow Ca_4P_2O_9 + 2Ca_3(PO_4)_2$	

Table 5. 2 Characteristic Raman bands for organic and inorganic phases for bone material.

Functional group	Wavenumber (cm^{-1})	References
PO_4^{3-}	$\nu_1 \rightarrow 960$	Penel et al., 2005
	$\nu_2 \rightarrow 430$	
	$\nu_3 \rightarrow 1068$	
	$\nu_4 \rightarrow 588$	
Amide I	1625, 1663	Penel et al., 2005
Amide III	1240 (β sheet)	Maiti et al., 2004
	1278 (α helix)	
	1338 (α helix)	Penel et al., 2005
C-H	$\delta \rightarrow 1450$	France et al., 2014
	$\nu \rightarrow 2883$	
	$\nu \rightarrow 2938$	
	$\nu \rightarrow 2971$	
CO_3^{2-}	754, 1068 (type B)	Penel et al., 2005; Gong & Morris, 2015
	1102 (type A)	
	1416 (ν_3 asym)	Movasaghi et al., 2007
Tryptophan	1530, 1576	Penel et al., 2005; Movasaghi et al., 2007
	740, 779	Zhu et al., 2011
Phenylalanine	618, 717, 1003, 1190, 1610	Penel et al., 2005; Zhu et al., 2011
	1582 δ(C—C)	Movasaghi et al., 2007
hydroxyproline	870	Gong & Morris, 2015
Other amino-acids	645 (proline), 857 (proline)	Gong & Morris, 2015; Zhu et al., 2011
	670 (C—S; cytosine); 697 (C—S; methionine); 1206 (tyrosine)	Movasaghi et al., 2007
ADN	682 (ring breathing mode), 725 (ring breathing mode), 823 (Out of plane ring breathing)	Movasaghi et al., 2007
Phospholipids	1123 (ν(C-C) trans), 1131 (fatty acids), 1745 (ν C=O)	Movasaghi et al., 2007
	1313 (δ(=CH))	Penel et al., 2005
Collagen/Lipid	1313 (CH_3CH_2 twisting mode of collagen/lipid)	Movasaghi et al., 2007
H_2O	1638 (Intermolecular bending mode of water)	Movasaghi et al., 2007
O-H	3232 (stretching)	Movasaghi et al., 2007

5.3. Elemental mineral composition

Table 5.3 shows the mineral traces in parts per million for trabecular bone powder before and after a cleaning process. The major elemental component are sodium and magnesium. It is possible to see a loss in the mineral content for the sample obtained after the cleaning process due to the partial removal of the organic phase, and then it is clear that some of these ions are bonded to this phase. In this section, it is important to remember that the chemical composition of the bone can vary in mammalian bones. Therefore, certain changes in the values are not due to the clean and calcination process but to the sample heterogeneity (Londoño-Restrepo *et al.*, 2018).

Table 5. 3 **Elemental composition of the trabecular bone powder.**

Sample	Mineral content (ppm)					
	Na	Mg	K	Zn	Al	Fe
Bovine Trabecular Bone Powder (BTBP)	6689.23	3048.49	414.89	90.17	33.98	9.89
Defatted BTBP	5463.60	2720.90	147.45	78.54	21.73	16.63

5.4. Morphological characterization of sponges

Figure 5.3 A to C shows the SEM images of a sponge cube that were taken from three different directions perpendicular to the YZ, XZ, and XY planes (see Figure 5.3 D), respectively. The sponge has a three-dimensional structure with different architectures for each direction because the bone has different functions within the body. The longitudinal and transversal continuous millimetric channels that percolate through the sponge can be observed in Figure 5.3 A to C; these channels correspond to the primary porosity of the trabecular bone. The width of these channels depends on the specific direction. These channels exhibit semi-circular shapes and they allow the presence of the blood vessels (Ural & Vashishth, 2007). Figure 5.3 A shows the YZ plane (parallel to the femur length) that is characterized by a continuous network with micro holes with diameters from 0.1 to 1.6 mm, where collagen fibers and fat are forming a percolative organic phase. Figure 5.3 B shows the XZ plane (parallel to the femur length) where it is possible to observe that trabeculae are forming parallel layers supported by hydroxyapatite columns. A detailed inspection of these images shows that the trabeculae that form these layers are not continuous and have a particular architecture as it will be seen in the next section. Figure 5.3 C shows the SEM images of the trabecular architecture for the XY plane characterized by channels with micro holes whose diameters vary from 0.15 mm to 1.6 mm, and it is evident that this network is interconnected. In this direction, the slope of the trabeculae is about 45°. At low magnification, the trabecular surface appears as a dense area which is in fact formed by aligned hydroxyapatite crystals imbibed in a proteinaceous matrix but, when the magnification increases to 1500X, it is possible to see that the bone has other kinds of porosities, for this reason a more detailed analysis of the microstructure of the trabeculae was conducted.

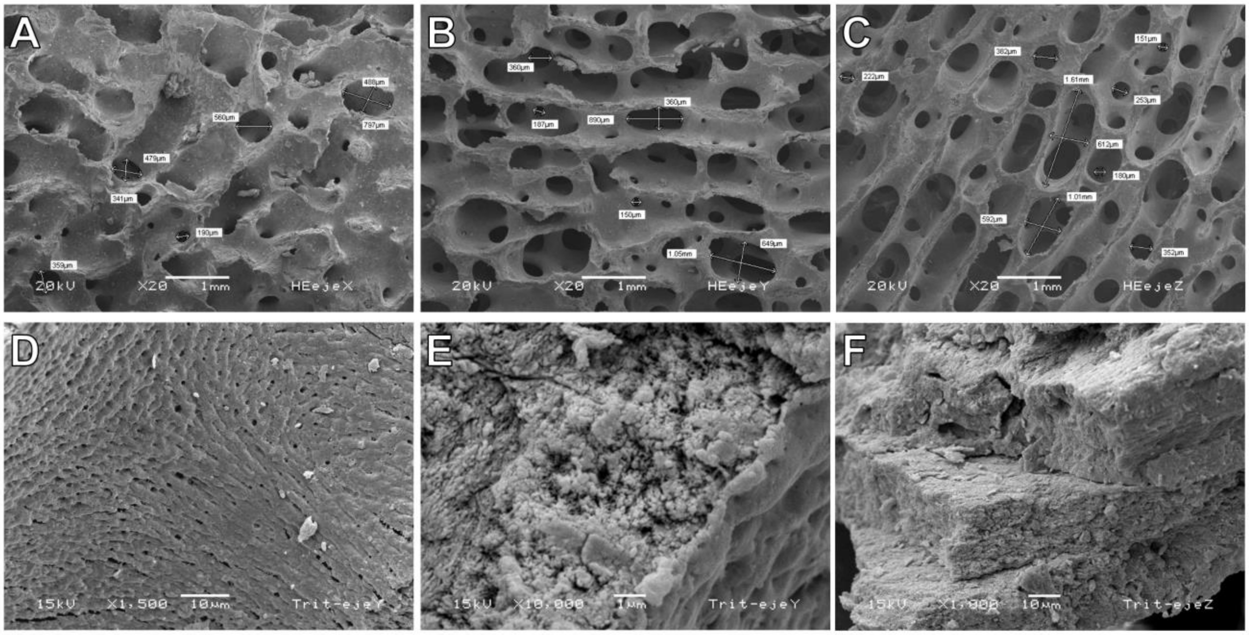

Figure 5. 3 SEM images for sponge cube in the (A) YZ plane, (B) XZ plane, and (C) XY plane, and SEM images of the internal part of the trabecular bone taken at (D) 1500×, (E) 10000×, and (F) 1000×.

In Figure 5.3 D, micro holes in the trabecular bone were observed which can be referred as the secondary porosity, while in Figure 5.3 E nano holes are present which can be identified as the tertiary porosity of this kind of trabecular bone. In Figure 5.3 F, a lamellar structure is observed which indicates that the trabecular bone could have a preferred orientation. Figure 5.3 D shows a SEM image taken at 1,500× of the surface of the trabecular bone where is possible to see canaliculi. Canaliculi are small channels where bone cells can communicate with the central conducts; these canals have diameters from 0.2 to 1 µm (secondary porosity). Figure 5.3 E was taken at 10000×, and it shows the frontier between the trabecula surface where the canaliculi are located, and an inner zone less dense that exhibits nano-pores which correspond to the tertiary porosity.

5.5. X-ray tomography

Figure 5.4 shows the cross-sectional views for the trabecular bone cube. The three orthogonal planes shown intersect at a point that can be used as the origin (0,0,0) of a Cartesian system of coordinates that serves as reference. These planes can be moved to any location in the volume, or additional tilted planes can be featured at any angle and position so the 3D volume can be inspected slice by slice. From the 2D slices, it can be seen that the bone microstructure is composed of an interconnected network. The porosity analysis of the bone showed that the overall porosity of the full bone specimen was around 60%, while the porosity of the trabecular bone cube section turned out to be close to 70% that corresponds to the primary porosity of this trabecular bone.

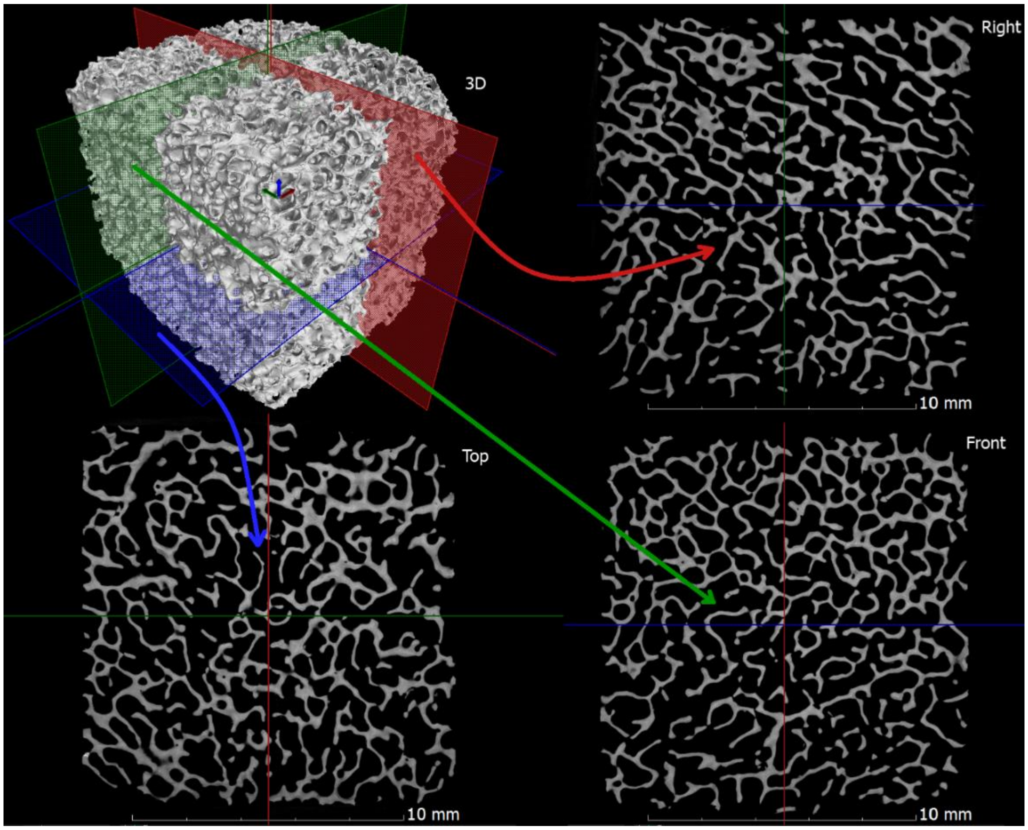

Figure 5. 4 3D image built from the 2D images in the three directions of the spongy bone cube. The black space corresponds to the primary porosity of the sponge.

5.6. Structural properties: X-ray diffraction

In this section, the crystalline orientation of the trabeculae perpendicular to each plane was studied. Figure 5.5 A to C shows the X-ray diffraction patterns for the trabecular bone cube taken perpendicular to planes YZ, XZ, and XY, (X, Y, and Z directions), respectively (Figure 3.1 C and Figure 5.3). The X-ray diffraction patterns show polycrystalline hydroxyapatite structures form trabeculae, these peaks in all cases are broad and the crystal size of these polycrystals is ranging from 10-20 nm and it was possible to identify some crystalline structures in these sponges. In Figure 5.5 B, for a better identification of the diffracted peaks, vertical lines identified the diffraction peaks for pure HAp (ICDD card No. 00-009-0432) and in Figure 5.5 C, the vertical lines correspond to the diffraction peaks for Calcite ($CaCO_3$) with ICDD card No. 00-001-0837. To determine the position of each peak, Lanthanum hexaboride powder (National Institute Standards and Technology (NIST)) was used as an internal standard (Standard Reference Material 660a). Another important aspect in relation to the spongy bone structure is that these patterns show the existence of a preferential crystalline orientation of the trabeculae that form the sponge, according to family of planes (002) and (004).

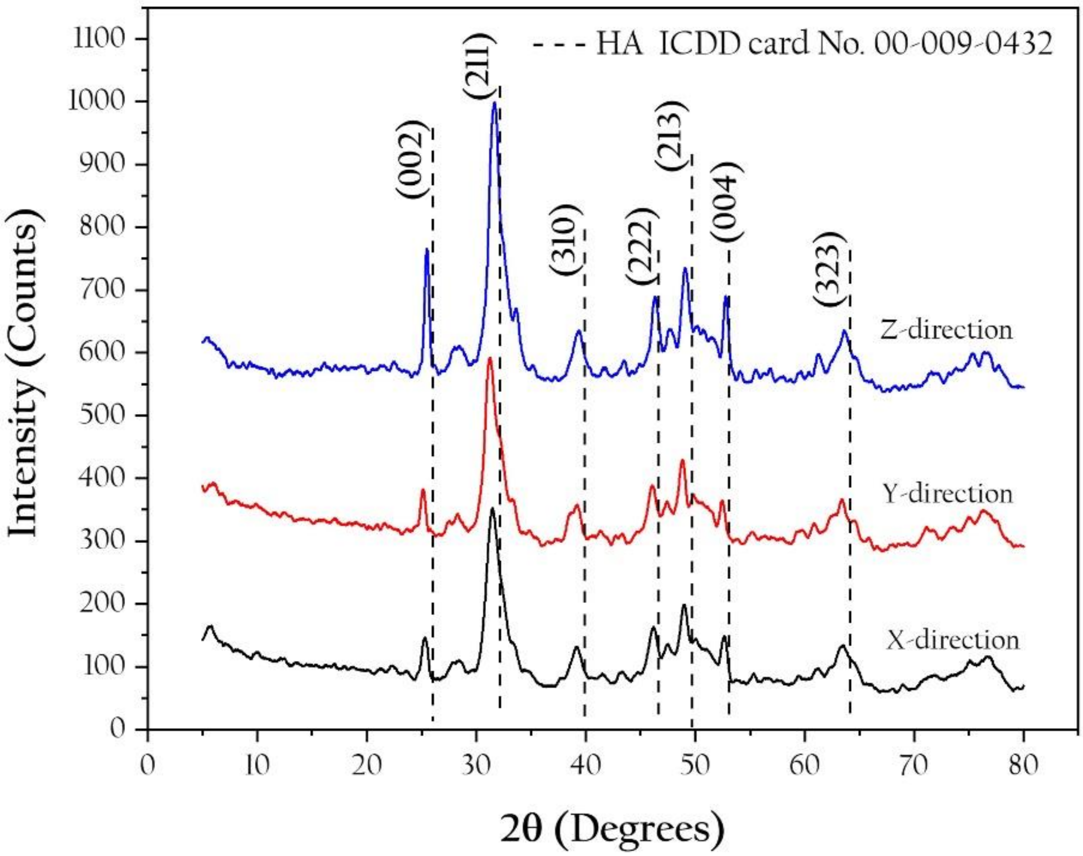

Figure 5. 5 X-ray diffraction patterns of sponges taken for the XY (A), YZ (B) and XZ (C) planes.

5.7. Mechanical properties

Figure 5.6 A shows the compressive test when the force was applied perpendicular to the YZ plane (Figure 5.6 A). From the first part of this figure, it is evident that the sponge exhibits an elastic behavior until point a (breaking point). From point a to b, it is possible to have a combined elastic-plastic regime. Consequently, the architecture of the sponge governs the mechanical properties. Figure 5.6 B shows the response of the sponge to a perpendicular force to the XZ plane, as it can be seen in Figure 5.6 B. In this direction, the sponge is formed by cylindrical tubes with micro holes, as the compression test exhibits. Then, only a simple elastic behavior occurs. Therefore, molecular forces govern these behaviors. Table 5.4 shows the modulus of elasticity and the compressive strength for each plane of the cube. In the case of a compressive force which is perpendicular to the XY plane as it is shown in Figure 5.6 C and Figure 5.3 C, the sponge exhibits the highest breaking force that is indicated by letter a = 898 N. Finally, this also corresponds to the fracture of columns (microstructure). The behavior of point b and c corresponds to a pure plastic deformation of the sponge that is associated with the rupture of the trabecular planes which are perpendicular to the columns.

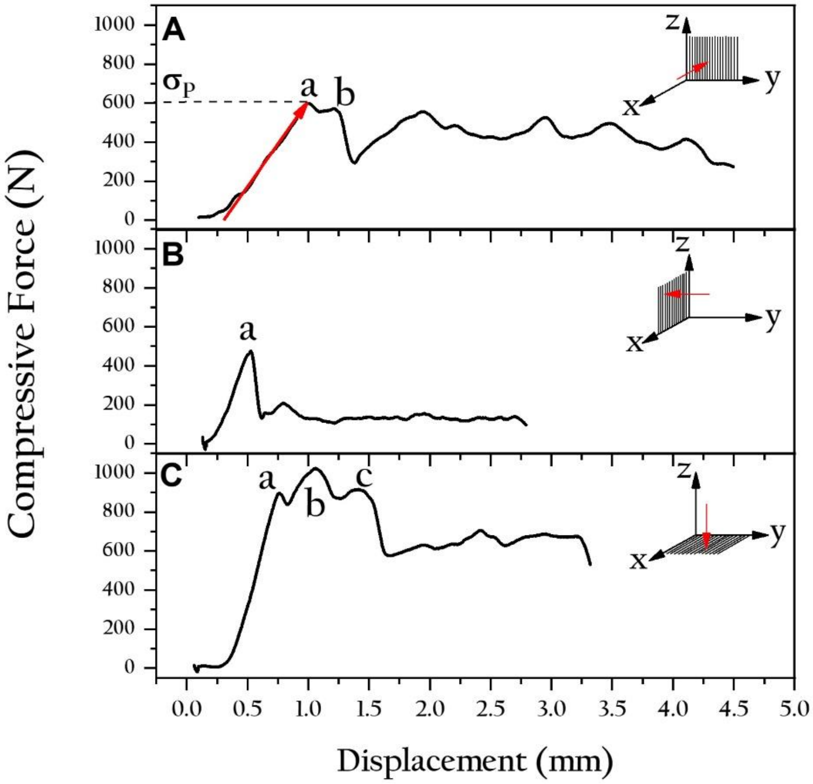

Figure 5. 6 Compression test taken for XY (A), YZ (B), and XY (C) planes of the sponge cube.

Table 5. 4 **Mechanical properties of the sponge cube.**

Plane	Peak	Compressive Force (MPa)	Modulus of Elasticity (MPa)
YZ	a	3.09	53.72
	b	2.93	40.13
XZ	a	2.45	92.62
XY	a	4.58	135.74
	b	5.25	95.27
	c	4.67	57.56

5.8. Discussion

In the case of the defatted bovine trabecular bone, the organic decomposition processes take place between 180 and 624°C. The peak located between 270 and 338 °C is related to the collagen degradation and protein denaturalization or de-branched (Londoño-Restrepo *et al*., 2018). Then, thermal events up 650 °C correspond to the inorganic phase (BIO-HAp, calcium carbonate, and other calcium phosphates). Thermal transitions found in the second region of the DSC curve which were labeled as a to f indicated that calcination process up 690 °C change the BIO-HAp structure due to the carbonate loss and dehydroxylation process. Then, calcinations above this temperature must be avoided to preserve the physicochemical properties of the apatite for clinical applications.

The presence of bands for carbonate in the Raman spectra indicates that there are carbonated hydroxyapatite crystals in the trabecular bone, and it contributes to confirm that BIO-HAp has ionic substitutions (Morris & Mandair, 2011). For this kind of samples, the presence of bands of amino acids which are not in the collagen type-I chains, indicates that there are non-collagen proteins as well. Based on the results, the hydrothermal process is an important step during bio-hydroxyapatite withdrawing because of through this treatment the phospholipids are extracted. The hydrothermal process also removed some minerals from the bone sample like Na, Mg, and K, but it does not indicate that the inorganic phase composition changed; the curtailment in the content for these ions is due to the organic removal as it was reported by Londoño-Restrepo *et al.*, (2018). It is widely known that the presence of these mineral traces helps to the bone regeneration, then, their presence is crucial for the tissue engineering and special for the scaffolds development.

For biomedical or tissue engineering, a complete morphological characterization of the spongy bone is the foundation for scaffolds development. The morphological characterization of the trabecular bone in this work is shown from the macro to the micro architecture. In this case, the micro-architecture corresponds to the morphology of one trabecula, while the macro-architecture is related to the morphology formed by the individual trabeculae that form the sponge. The morphology of the trabecular bone is influenced by factors such as the origin of the sample (human, bovine, pig, among others), the position into the bone, the type of bone, age, among others. The primary porosity of a bone is related to the volume of the milimetric channels exhibited in Figure 5.3 A to C, and it depends on extrinsic and intrinsic factors such as bone age, diet, and the assessed area. It is known that micro-porosity enhances bone growth because it allows blood irrigation and osteogenesis. The resulting micro-porosity provides a highly superficial area that promotes attachment points for osteoblasts and contributes to the growth of the new bone into the trabecular lattice. Interconnected pores provide sites for vasculature that is necessary for new bone creation and waste elimination. For this reason, an optimal proportion of pore size and interconnectivity for the creation of scaffolds is necessary (Woodard *et al.*, 2007), but it is also necessary to consider the 3D macro architecture. Bone scaffolds are created through tissue engineering in an attempt to emulate the physicochemical properties of trabecular bone and provide mechanical support during repair and bone regeneration of damaged or diseased bone (Bose *et al.*, 2012). According to these results, the macro-architecture of the sponge is strongly dependent on the bone orientation (position in the femur head). It means that the morphology of the sponge is anisotropic. This fact has a strong influence on the mechanical and functional properties of this kind of bone. In a detailed analysis of Figure 5.3, it is also possible to determine that the trabeculae form a porous system and a percolated lattice. Macro and micro porosities have been reported; macro-porosity corresponds to the pores with diameter holes bigger than 50 μm and less than 20 μm for micro-porosity (Morris & Mandair, 2011), but a tertiary nano-porosity was completely determined in this work by using SEM images. It is only possible to appreciate the tertiary porosity in a trabecular lattice by doing a rupture of the network. It is important to recall that this branching system provides many routes for the diffusion of the oxygen, blood nutrients, among others into the extracellular fluid to osteocytes, and it allows the expelling of cellular waste through the blood vessels.

The insight gained from imaging of the internal structure of the cube is quite valuable. After completing the CT scan process, including the reconstruction phase, the 3D reconstructed volume contains all internal and external geometry, allowing analysis of the specimen using clipping views or cross-sectional images with high spatial resolution (see Figure 5.4). The interconnected network of microporous channels, that composes the bone microstructure, facilitate blood irrigation. 3D analysis of the dimensions (size, spacing, volume) and network arrangement of the channels provide novel insights related to the porosity as well as the structural and mechanical properties of the bone. The 2D cross-sectional images of the cubical sample show marked differences in the cross-sectional network of channels and overall porosity, particularly anisotropy in the orientations as was shown in SEM images (see Figure 5.3). At Z = -2.8 mm, for example, some interesting features can be seen in the bone that are in accordance with the images obtained by SEM for the macro architecture and primary porosity. Thus, the CT-based analysis provides an efficient way to image and describe the 3D architecture inside of the trabecular bone, which facilitates a better understanding of the sponge that is valuable in the case of scaffolds design. Furthermore, it could be used to quantitatively obtain information on the topographical variation in orientation of the cortical channels as a function of the bone position. Differences in the found porosity can be attributed to the differences in the sponge as a function of the bone position.

As it was mentioned, the natural sponge has different trabecular morphologies as a function of the plane orientation (microarchitecture, see Figure 5.3). In the structural characterization, the crystalline orientation of the trabeculae perpendicular to each plane was studied. In these patterns, BIO-HAp as nano-polycrystals were identified but as well as calcium carbonate. A preferential crystalline orientation of the trabeculae that form the sponge according to family of planes (002) and (004) was found. Through a detailed inspection of these patterns, it is clear that the (002) direction (C direction for the hexagonal structure) exhibits different intensities as a function of the bone cube orientation. Consequently, the structure of the trabeculae that form the sponges shows a preferential direction perpendicular to the XY plane of the bone cube. It is important to remember that the growth of the femur is perpendicular to the XY plane. The relationship between I_{002}/I_{211} was 0.487, 0.474, and 0.565 for YZ, XZ, and XY planes respectively, indicating that the bone has a preferential orientation perpendicular to the XY plane. The shift of the lines of the PDF files to the right is related to the stoichiometry of the samples; the mineral phase of natural bone is a non-stoichiometric hydroxyapatite.

According to Bose *et al.* (2012), the ideal scaffold must have the following requirements: biocompatibility, mechanical properties, porous size, and bioresorbability. But according the X-ray diffraction analysis shown in this section, the preferential structure of the sponges also must be incorporated in their requirements, including micro and macro architecture and the most important fact, the preferential crystalline orientation of the bone sponge used for any implant to induce bone formation and vascularization.

Spongy bone is a complex composite system formed by porous trabeculae, collagen fibers and other organic compounds. The mechanical properties depend on different factors: the deformation that is originated on the molecular attraction forces by changes in the Coulomb force (interaction) and the tension created in the elastic solid. Therefore, the elastic properties of a solid depend on its internal structure. A compression test of a solid can be formed by means of three artificial regimens: elastic, elastic-plastic, and plastic. If the compression increases from zero to σ_P in a comparable way with the unitary deformation, the system being in the elastic region (a linear relationship between deformation and compression); point *a* in Figure 5.6 corresponds to this proportional limit. For all studied samples, the limit of elasticity corresponds to the breaking point. According to the compressive test results, the mechanical properties of the sponge are governed by three independent factors: the microarchitecture, the number of trabeculae, and their crystalline structure. In consideration of the results showed in Table 5.4, it is clear that natural sponges have different responses in the case of uniaxial compression for each direction. The microarchitecture of the sponge that is shown in Figure 5.3 reveals that the sponge has different microarchitectures per direction, and this fact could be originated due to the direct function of the sponge within the bone. Young's modulus for the sponge cube in the three studied directions was between 40.13 and 135.74 MPa. Mechanical properties were higher for Z direction than for X and Y as it was expected, due to in this direction, large bones support all weight of the body. Although these values are in accordance to Poumarat & Squire (1993) that reported the Young's modulus (117.49 MPa) for fresh trabecular bovine bone with marrow after a compressive test, they did not consider the bone direction, and it is worth noting that fresh bones have higher mechanical properties than dried bone because of the presence of organic material.

5.9. Conclusions

Several materials have been developed for tissue engineering as an attempt to replace the natural bone then, it is crucial to know the physicochemical properties of the bone for the design of artificial sponges. Raman spectra and mineral content showed that sponges are formed by hydroxyapatite with substitutional ions like Na and Mg, calcium carbonate, collagen and some non-collagen proteins. Based on the thermal properties of trabecular bovine bone, it can be concluded that BIO-hydroxyapatite is a steady phase until 650 °C, after this temperature, the physicochemical properties of the mineral phase of the bone change drastically. The natural defatted sponges studied in this work are formed by trabeculae that according to SEM images and X-ray tomographies have a preferential orientation as well as a well-defined microarchitecture. SEM images reveal that sponge architecture is influenced by the functionality of the bone, and that trabecular bone exhibits a complex percolated system which allows the nutritional exchange. The X-ray diffraction patterns confirmed the anisotropic character of the bone and show that trabeculae are formed by nano polycrystalline structures that exhibit a preferential orientation for the (001) plane, which is parallel to the bone growth (Z direction) and where the bone exhibits the highest mechanical properties. The mechanical properties of the sponge (three-dimensional) show that this structure has a different response as a function of the direction of the compression force. The polycrystalline structure of the trabeculae, as well as the collagen matrix, govern its elastic properties. It was found that a combined region of elastic-plastic is associated with the structure and microstructure (micro-architecture) of the sponge. A pure plastic deformation was found only for compression force perpendicular to the XY plane, and it is associated with the rupture of the trabeculae and layers. The studies as mentioned above show that there is a significant difference between natural sponges and designed scaffolds. Therefore, the morphology and the complex microstructure of the natural sponges as a function of the direction have not been considered in the design and fabrication of artificial sponges. Finally, it is clear that the properties of the natural bone are highly complex to be emulated, then the use of mammalian bones is still the best option for tissue engineering.

CHAPTER 6

EFFECT OF THE CRYSTAL SIZE ON THE X-RAY PATTERNS OF HAp FROM, BOVINE, PORCINE, AND HUMAN BONES

This section focuses on the study of the effect of the change of the crystal size on the shape and width of the X-ray diffraction patterns for defatted and deproteinized bones as well as incinerated biogenic hydroxyapatite obtained from bovine, porcine, and human bones. Inductively Couple Plasma showed the presence of some ions such as Mg, K, Al, Fe, Zn, and Na for all samples. The nanometric size of the crystals was determined through High Resolution Transmission Electron Microscopy in which ordered crystals were found. The calcination of raw clean bones at 720 °C produced a transition of crystal size from nano to micro due to a coalescence phenomenon, this was accompanied by a decrease of the peak width of the X-ray diffraction patterns due to the decrease of the inelastic scattering contribution from the microcrystals. A simulation of the effect of the crystallite size on the shape and width of the X-ray patterns was done using PDF-4 software which confirmed that raw ordered bone crystals produce broad peaks which so far have been erroneously assigned to polycrystalline hydroxyapatite with low crystalline quality.

Nowadays, there is an increasing interest in nanomaterials in different fields such as tissue engineering. One of these is the hydroxyapatites (HAp) from biological sources such as human, bovine, and porcine due to their different applications (Tagaya *et al*., 2010; Syamchand & Sony 2015; Fihri *et al*., 2017). The structure of these biogenic materials has been studied using X-ray diffraction (XRD). However, there is still a problem in the interpretation of their patterns concerning to the shape and width for raw and incinerated biogenic hydroxyapatite that are commonly used in clinical applications. This misinterpretation could limit their potential uses.

It is well established that the above-mentioned biogenic sources are formed by nanocrystals of HAp that contain~~s~~ minor elements such as Mg, Na, S, and K. Even with the presence of these ions, the XRD patterns of the raw bone mineral phase almost exhibit the same positions as those of synthetic hydroxyapatite (Giraldo-Betancur *et al.*, 2013). But, the peaks for biogenic hydroxyapatites (BIO-HAps) are less sharp and broader which is attributable to the small size of crystals (Boskey 2003). The ions presence influences the structural, thermal, optical, and morphological properties of hydroxyapatite (Londoño-Restrepo *et al.*, 2018), and are very important for tissue engineering applications. Until now, several methods are widely used to isolate the mineral phase from the organic matrix of the bone: alkaline or acid hydrolysis, subcritical water process, and thermal decomposition (incineration) (Sobczak *et al.*, 2009).

The physicochemical properties of the isolated phase obtained by incineration depend on variables such as heating rate, annealing temperature, sintering time, cooling, and the atmosphere (Londoño-Restrepo *et al.*, 2016; Ramirez-Gutierrez *et al.*, 2016; Londoño-Restrepo *et al.*, 2018). One of them is the crystal size that is commonly determined through X-ray diffraction. In the case of tissue engineering, some requirements are necessary for replacement materials among bioactivity, biocompatibility, biodegradability, osteoinductivity, enough mechanical properties, and a suitable architecture (O'Brien 2011). However, the nanometric crystal size as a requirement has not been explored. In this direction, it was found that some commercial hydroxyapatites for clinical applications showed microcrystals that could be the result of high annealing temperatures (Giraldo-Betancur *et al.*, 2013).

The structural properties of hydroxyapatite from several sources have been studied by X-ray diffraction, in which information about the determination of crystalline structures, crystalline quality, crystal size, and lattice defects can be obtained. However, according to Scardi 2008 and Piga *et al.* (2008), the XRD analysis and the reliability of the results when the domain size is in the nanoscale as is the case of BIO-HAp, are still an open problem due to the elastic and inelastic signals are detected at the same time and affect the peak width and shape of the patterns.

Ooi *et al.* (2007) showed that the X-ray pattern of raw bovine bone exhibits the presence of nanocrystalline apatite. Their results indicate that in annealed samples between 700 to 1000 °C, a substantial increase in the height and a decrease in the width of the peaks occur which were associated with an increment in crystallinity and crystallite size. The same findings were reported by Niakan *et al.* (2015). However, if the initial state of the hydroxyapatite of the bovine bone corresponds to nanocrystals, the width and the height of the peaks cannot be correlated with crystalline quality due to elastic and inelastic scattering phenomena governing them.

Ramesh *et al.* (2018) studied the effect of the incineration process used to obtain HAps on their structure and found out that if the temperature increases, the crystalline quality follows the same trend, resulting in a change from broad to sharp peaks in the patterns. The average crystal size for nanoparticles is usually obtained by calculating the Full Width at the Half Maximum (FWHM) and the Scherrer´s equation as well as its modifications (Monshi *et al.*, 2012). However, this equation has limitations since the lattice strain contributes to line broadening and the presence of organic components contribute strongly to the background. Both facts produce an error in the peak fitting and width calculation estimated in 10–15% (Suvorova *et al.*, 2007). Therefore, XRD patterns do not give a precise calculation of the crystal size. It only provides an order of magnitude for nanoscale-sized crystals in bones.

The crystallinity value is a parameter used to determine the atomic order of the atoms into the lattice and can be determined using an order parameter (Ramirez-Gutierrez *et al.*, 2014) which can be affected by intrinsic and extrinsic factors. On the other hand, the crystalline quality (CQ) is a parameter that can only be determined through the FWHM when the pattern is governed by the elastic contribution. If the crystal size is in the range of some wavelengths as is the case of λ=1.5406 Å for CuK$_\alpha$, it is not possible to determine the CQ because the pattern has elastic and inelastic contributions that are so far impossible to separate (Laven 2010).

Patel *et al.* (2015) reported an average length of 48.58 ± 0.13 nm and a width 5.41 ± 0.09 nm for bovine bone using TEM images, but they pointed out that this sample is amorphous. However, their TEM images showed ordered crystals. Barakat *et al.* (2009) also studied the crystallinity of apatite from bovine bones using TEM images. However, the crystal size was not evaluated, and the crystalline percentage again was correlated with the peak width.

6.1. Mineral composition.

Figure 6.1 A shows the mineral content of Ca and P majority elements for raw and sintered BIO-HAp samples, and HAp from Sigma. No differences between raw clean bones and samples calcinated at 720°C were found. Figure 6.1 B exhibits Ca/P atomic ratio for Raw and calcined bone samples as well as for HAp from Sigma Aldrich. The high Ca content in H-Raw increases the Ca/P ratio. Figure 6.1 C exhibits the content of the mineral traces in the bones which is well known to enhance bone regeneration.

6.2. TEM analysis.

Figure 6.2 shows HRTEM images for defatted and deproteinized B-Raw (A-D), P-Raw (E-H), and H-Raw (I-L) samples, where B-Raw corresponds to defatted and deproteinized bovine bone powder, P-Raw for porcine, and H-Raw for human. HRTEM images showed that clean raw bones are formed by polycrystalline nanocrystals with elongated plate shapes. Xin *et al.* (2010) reported HRTEM images of cortical human bones as thick mineral flakes and needles. However, in our work, the needles structures for human bone were not found, but their interpretation can be based on the transversal view of the elongated plates or flakes.

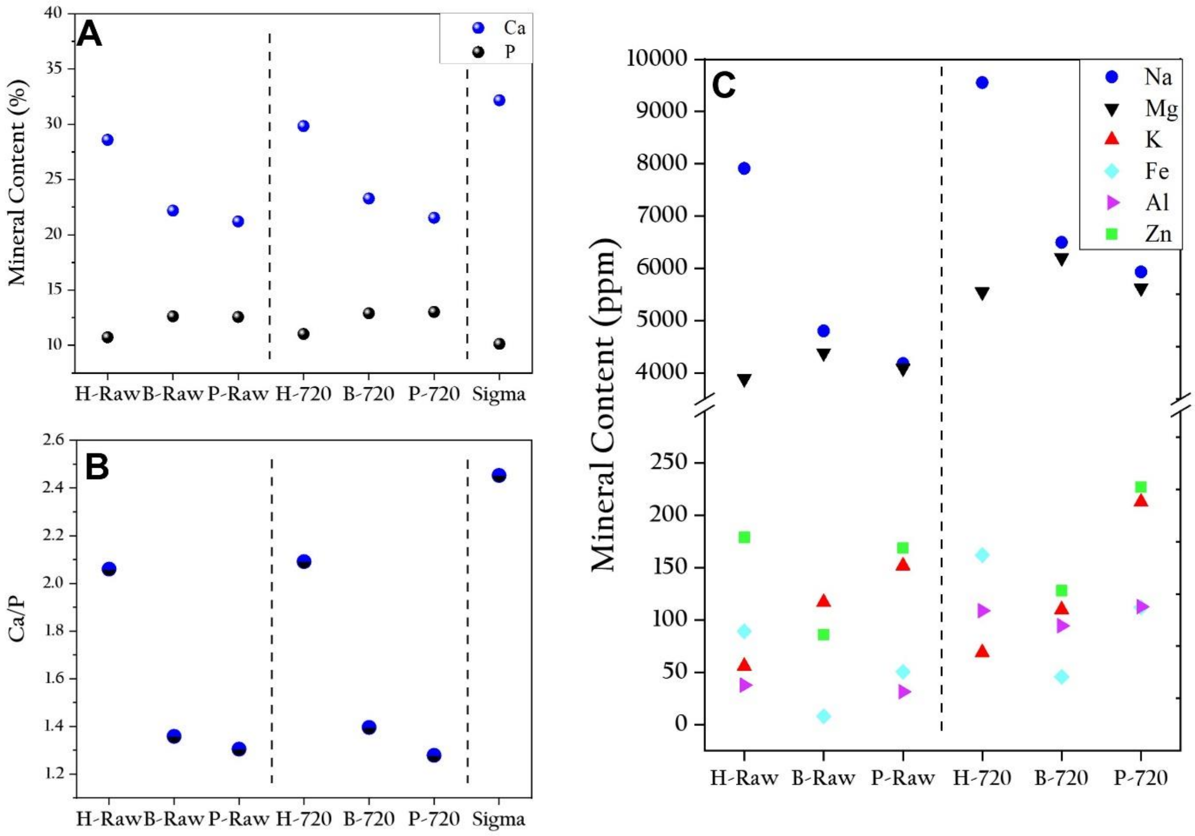

Figure 6. 1 (A) Ca and P content for HAp from Sigma, raw, and sintered samples, (B) Ca/P ratio, and (C) minority mineral composition.

The Image J software was used to determine the crystal size (2D) and the average value for 25 determinations were: 21 ± 8 nm and 6 ± 1.5 nm for H-Raw; 13 ± 3 nm and 7 ± 2 nm for B-Raw; and 17 ± 4 nm and 6.4 ± 0.4 nm for P-Raw, for length and width, respectively. These findings confirm the nano-dimensions of the hydroxyapatite crystals of raw bones, which are elongated like-plates that can be correlated with the well-known longitudinal and preferential growing of the bone (Londoño-Restrepo *et al.*, 2018). TEM analysis showed the presence of well-defined nanocrystals and the (112) and (002) planes for bovine bone, (211) for porcine, and (112) for human, indicating crystalline order. Patel *et al.* (2015) pointed out that raw bone powder from bovine is crystalline based on TEM images. According to Glimcher (2006), longitudinal like plates are formed by small spherical ones that are the youngest nanocrystals and the long needle shaped ones that are the older crystals.

The determination of the distances between the lines and dots was done using the Digital Micrograph software. All these samples are polycrystalline because of the multiple directions that are observed in their Fast Fourier Transform images (Figure 6.2 C, G, and K). For B-Raw, some dots are separated by 0.27nm which corresponds to the ‹112›, while the other distance (0.34 nm) corresponds to ‹002› family of directions. In the case of P-Raw, the direction ‹211› was identified as well as the ‹112› for H-Raw nanocrystals. All these planes were identified using the ICDD card # 01-084-1998 for synthetic hydroxyapatite.

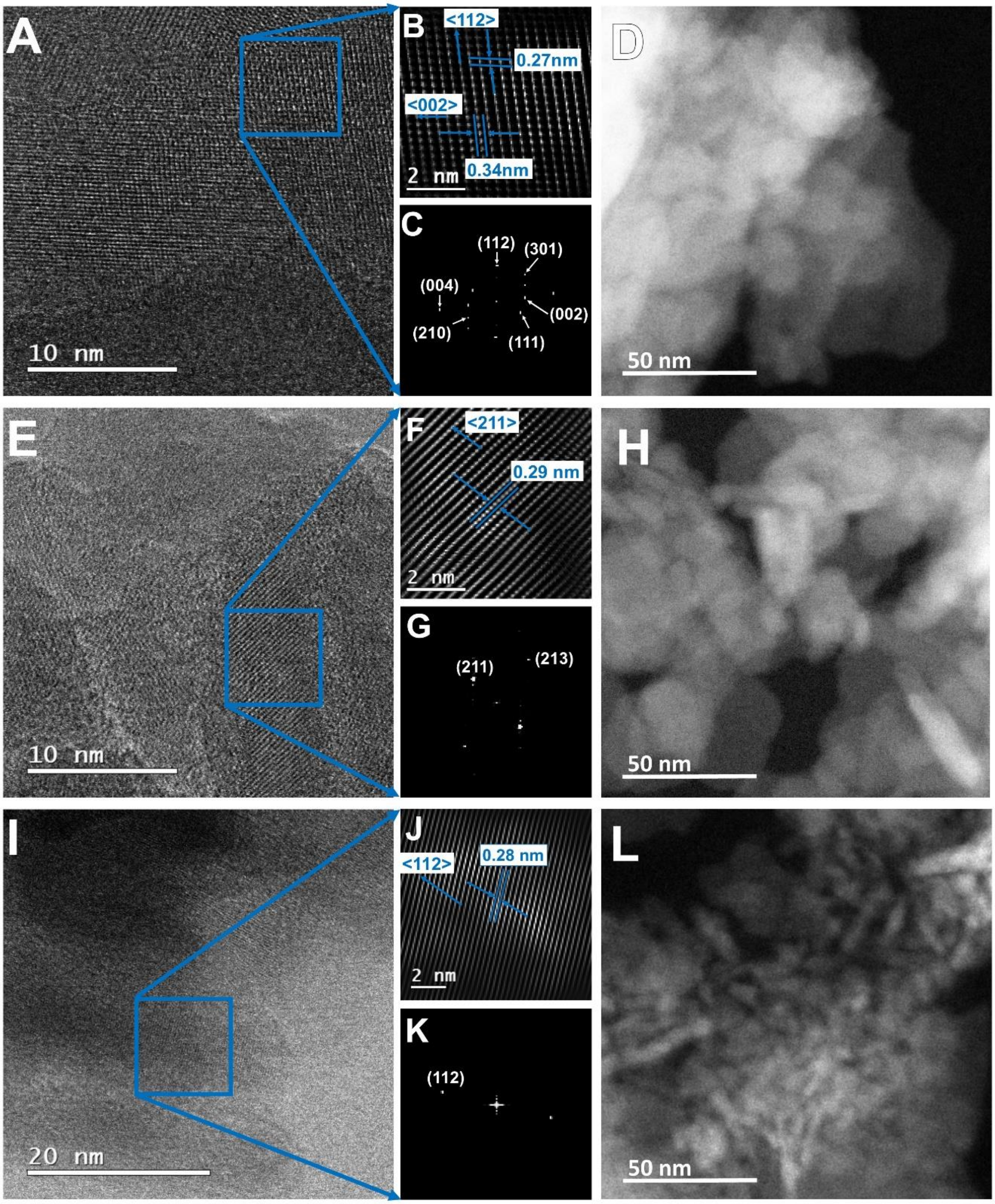

Figure 6. 2 HRTEM images for raw HAp crystals: B-Raw (A-D), P-Raw (E-H), and H-Raw (I-L).

6.3. SEM: morphological analysis.

After calcination at 720°C, HAp crystals reach sizes in the order of microns as in the case of H-720. Figure 6.3 shows SEM images for calcinated samples B-720, P-720, and H-720.The B-720 sample exhibits crystals with elongated shapes whose boundaries are joined to those of other crystals. It evidences that the growing process by coalescence was interrupted (Figure 6.3 A). In the case of P-720 sample, a bunch of crystals can be seen, which allows determining that the elongated structures are formed by their coalescence (Figure 6.3 B).

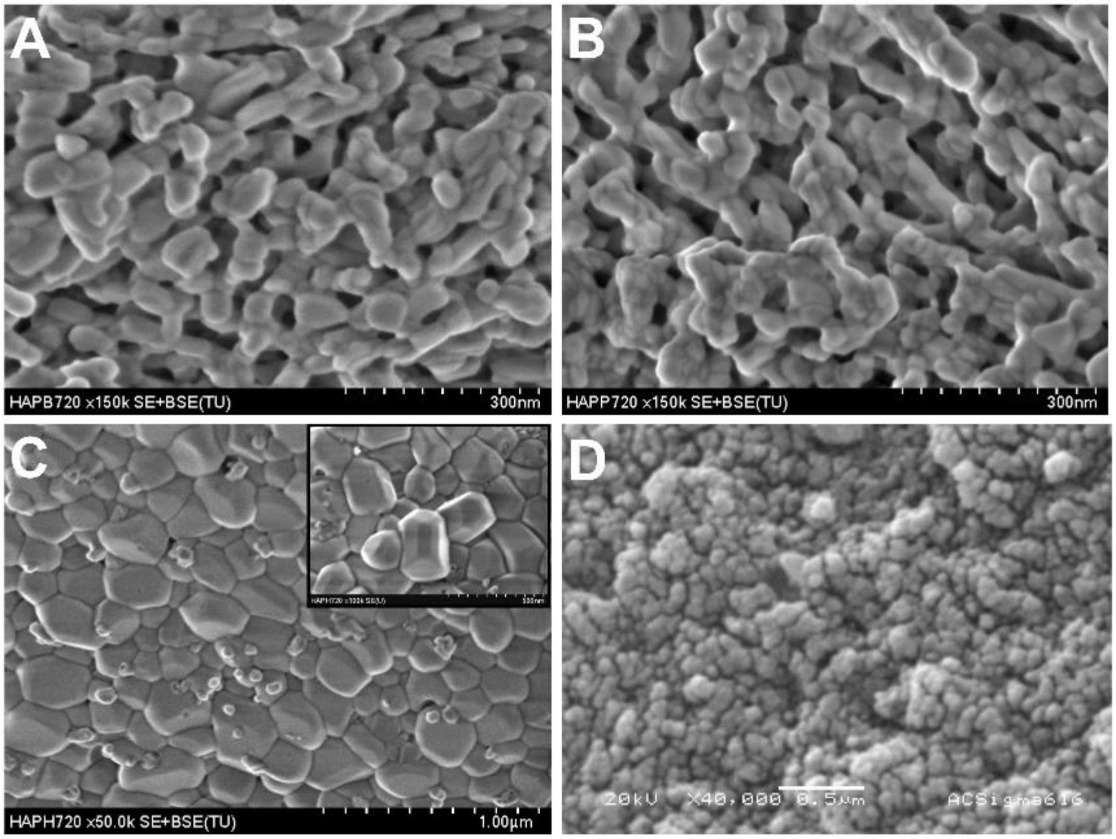

Figure 6. 3 SEM images for calcinated samples: (A) B-720, (B) P-720, (C) H-720, and (D) Sigma-Aldrich.

Human HAp crystals have irregular faceted shapes, and some hexagonal prisms are observed, but also small spherical crystals were identified as magnesium oxide as will be shown in the XRD section. It is worth noting that B-720 and P-720 are porous systems in which blood irrigation and vascularization are possible when these materials are used for clinical applications, but hydroxyapatite crystals for H-720 sample do not have any pores.

Newly, the Image J software was used to determine the 2D dimensions of the HAp crystals. The average lengths and widths are 117 ± 19 nm and 42 ± 9 nm for B-720 and 62 ± 9 nm and 28 ± 4 nm for P-720, respectively. In these cases, BIO-HAps are not single crystals yet but coalesced crystals that are still growing; this is the reason for the huge standard deviation for both samples. On the other hand, H-720 crystals developed the highest sizes until 330 ± 60 nm length and 200 ± 40 nm width on average. Pseudo-spherical crystal shapes and some hexagonal structures with well-defined facets were found (see inset in Figure 6.3 C). Figure 6.3 D displays HAp crystals from Sigma Aldrich that are clearly a synthetic HAp since these crystals do not exhibit the characteristic morphology and crystal size of HAp from mammalian bones.

6.4. X-ray diffraction.

Figure 6.4 shows a characteristic XRD pattern of a defatted and deproteinized cortical bovine bone. As it well known, a pattern is formed by: sample contribution (crystalline and amorphous), noise (background), and instrumental function. However, it is critical to show that the region that has been used to describe the crystalline contribution of a nano-crystalline sample is formed by elastic and inelastic scattering and the instrumental function, which means that it is not possible to determine independently each one of these signals. Hence, the regions that can be defined in X-ray pattern of a nanoparticles are the elastic and inelastic scattering contributions that involve information regarding the nano-size character of the crystals in the sample, the amorphous region, and the background (see Figure 6.4). Moreover, each instrument has an instrumental function that contributes to the final shape of the pattern.

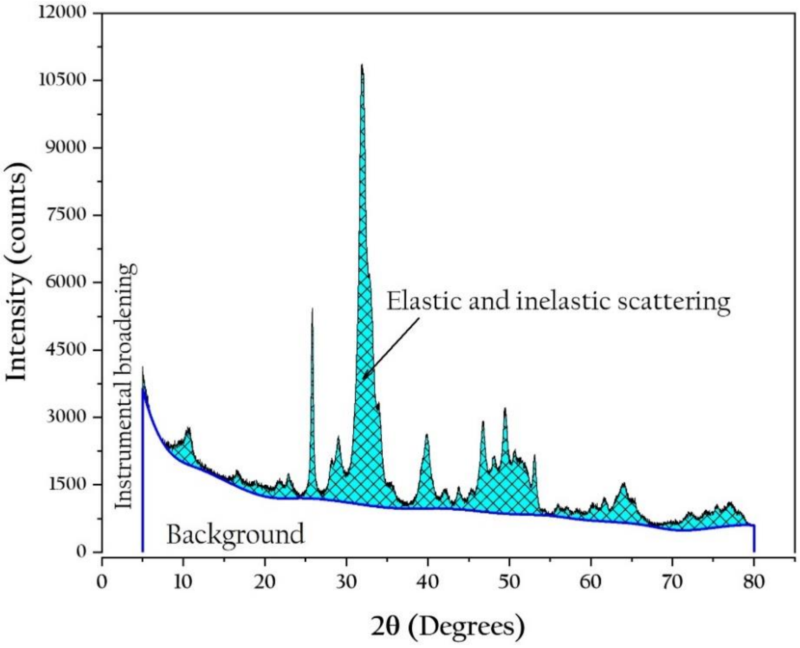

Figure 6. 4 Typical X-ray diffraction pattern of defatted and deproteinized bovine bone.

Figure 6.5 A shows the X-ray patterns of nano-Bio-HAp obtained for H-Raw, B-Raw, and P-Raw bones, incinerate samples H-720, B-720, and P-720, and Sigma Aldrich. The patterns of raw

HAps exhibit broad and not well-defined peaks and after calcination, the H-720, B-720, and P-720 patterns are characterized by sharp and well-defined peaks. The peaks identification in these X-ray patterns was done by ICDD card No. 01-084-1998 for hydroxyapatite. The peak width of the incinerated samples in relation to the raw samples decrease, while an opposite trend was found for the intensity, indicating that the elastic contribution governs the patterns for incinerated samples while the X-ray diffraction of raw materials has elastic and inelastic scattering contributions.

Table 6. 1 **Additional crystalline phases found for H-720.**

Additional Crystalline Phases			
Sample peak position 2θ (°)	**Phase**	**Peak position 2θ (°)**	**(hkl)**
26.08	$NaCaPO_4$	26.21	(200)
28.69	$NaCaPO_4$	28.68	(121)
29.42	$CaCO_3$	29.40	(104)
29.71	$Ca_3(PO_4)_2$	29.65	(300)
30.89	$Ca_3(PO_4)_2$	31.02	(0 2 10)
31.98	$NaCaPO_4$	32.09	(130)
32.38	$Ca_3(PO_4)_2$	32.44	(128)
32.97	$Ca_3(PO_4)_2$	33.02	(306)
33.12	$NaCaPO_4$	33.14	(002)
33.45	$Ca_3(PO_4)_2$	33.48	(1 1 12)
37.39	CaO	37.34	(200)
40.01	$Ca_3(PO_4)_2$	40.06	(1 1 15)
40.23	$Ca_3(PO_4)_2$	40.21	(042)
42.93	MgO	42.91	(200)
43.25	$CaCO_3$	43.14	(202)
53.91	CaO	53.85	(220)
60.26	$Ca_3(PO_4)_2$	60.37	(158)
62.44	MgO	62.30	(220)

All raw samples and B-720, and P-720 were identified as hydroxyapatite (ICDD No. 01-084-1998), but for the H-720, other crystalline phases were identified by using the following power diffraction files: Whitlockite ICDD card # 00-009-0169, $NaCaPO_4$ ICDD card # 00-029-1193, Calcite ICDD card # 00-047-1743, MgO ICDD card # 00-004-0829, CaO ICDD card # 00-037-1497. Additional phases present in the H-720 sample are reported in Table 6.1; MgO is confirmed in the SEM image for H-720 (Figure 6.3 C) as small spheres which were previously identified by Energy-

Dispersive X-ray Spectroscopy (EDS) (Ramirez-Gutierrez *et al.*, 2017). The presence of the additional phases for H-720 sample obeys to the age of the bone. It is well known that bovines are slaughtered 2-years-old and 5-months-old for pigs, while the studied human bone belonged to an adult that changes its composition due to metabolic activity, aging, and disease. Although, the presence of MgO is due to a diffusion issue where magnesium naturally present in the bone (Meneghini *et al.*, 2003) reaches the melting point at 650 °C and the oxidative atmosphere where the sample was calcined.

As shown in Figure 6.5 A, these patterns correspond to nanocrystalline samples. As it has been pointed out in different scientific works, hydroxyapatites from mammalian bones have been characterized as nanoparticles with low crystalline quality, considering that the diffracted peaks are broad and weak. However, by the inspection of different HRTEM images for these samples, they have a crystalline order. Figure 6.5 B shows the FWHM for the (002) peak of XRD patterns for raw samples (H-Raw, B-Raw, and P-Raw), calcined samples (H-720, B-720, and P-720), and Sigma Aldrich. Raw samples showed higher FWHM values than the calcinated samples, which is not an indicative that these samples are poorly crystalline.

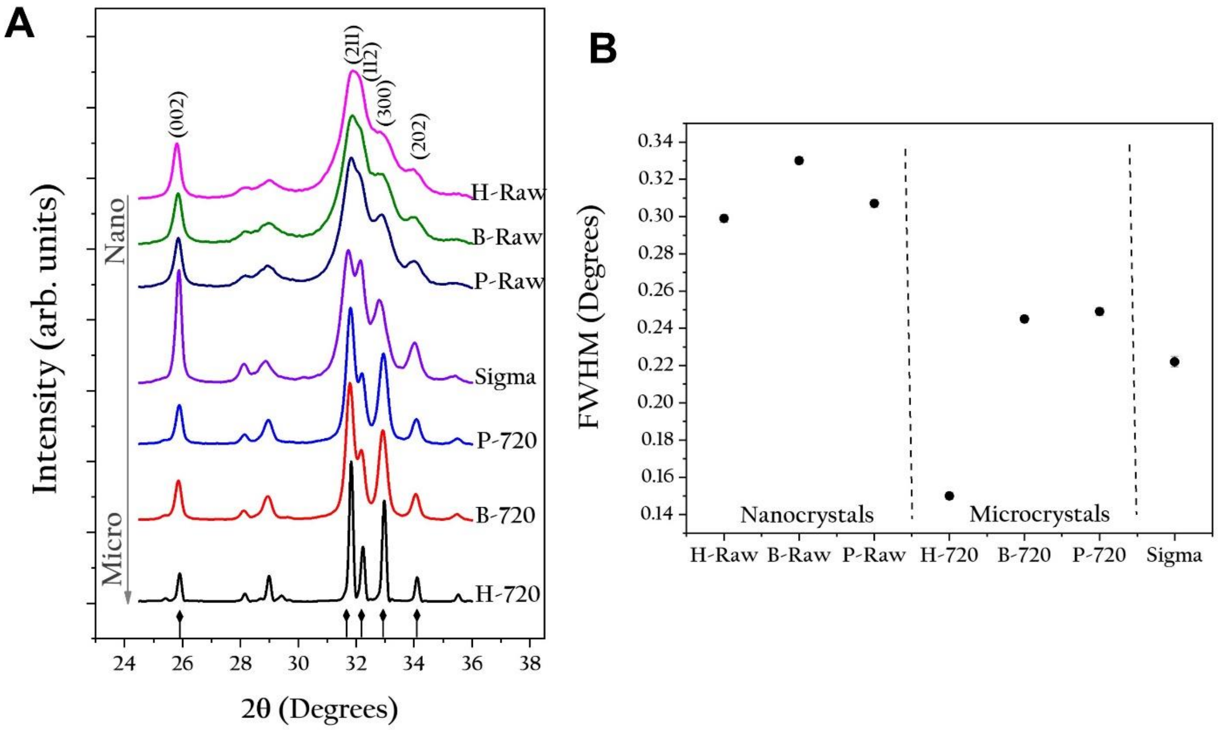

Figure 6. 5 (A) X-ray diffraction patterns for all samples (H-Raw, B-Raw, P-Raw, H-720, B-720, P-720, and Sigma), and their respective (B) FWHM calculated for the (002) peak.

6.5. Simulation of the effect of the crystalline size on the XRD patterns

The effect of the crystal size on the X-ray diffraction patterns has been studied in detail by using the PDF-4 software (Kabekkodu *et al.*, 2002; Needham & Faber 2003), that consider the peak shape analysis to provide information on particle size and strain distributions of the samples as well as the Bragg intensities that gives information about possible preferred orientation and texture effects in powder samples, for the PDF-4 analysis of the effect of the crystal size a characteristic Powder diffraction files for synthetic HAp (ICDD No. 01-084-1998) was used (Faber & Fawcett 2002).

As was confirmed by HRTEM images for the raw HAp samples, all of them are nanocrystals with lengths below 20 nm and width about 7 nm, and according to Figure 6.5 A, nanocrystals produces drastic changes in the shape and width of the XRD patterns. As it was mentioned before, it is possible to simulate the effect of the crystal size on the shape and width of the XRD patterns using PDF-4 software and this software was considered an ordered crystal. For this simulation and considering the HRTEM findings, the initial crystal size was 7 nm and the effect of the growth of the crystals was evaluated. Figure 6.6 shows the simulation of the XRD patterns for HAp using the ICDD No. 01-084-1998 for HAp varying the crystal size from 7 to 28 nm. For crystal sizes of 7 and 10 nm, the patterns correspond to broad peaks. The crystal size is sometimes the incident wavelength of the CuK$_\alpha$ radiation, in this simulation, it was not considered the amorphous contribution of the material. While, if in the simulation, the crystal size increases from 14 to 28 nm, the broad peaks become narrower and more defined because the X-ray inelastic scattering decreases and the resulting diffracted peaks are governed by the elastic scattering (diffraction) in the crystalline structure of the hydroxyapatite crystals. Here, it is important to clarify that this effect is less evident for the studied samples due to other issues (instrumental, sample nature, among others) that influence the pattern. These simulations showed clearly that the reported XRD patterns for raw bones, in fact correspond to nanocrystals and these do not represent as it has been mentioned before "poly-crystals with low crystalline quality".

With techniques as HRTEM or SEM it is possible to determine directly the crystal size. Another technique used in determining or estimating the crystal size of polycrystalline samples is X-ray diffraction using the Scherrer's equation. However, it has some limitations, for example, derivation of Eq. 6.1 does not consider the type or scattering power of the atoms, and instrumental function. These acceptable results are restricted to sizes up to a few hundreds of nanometers. Cullity & Stock (2001) showed that the Scherrer's equation is valid only for crystallite sizes up to 200 nm and has close relation to the resolution of the diffractometers. According to Miranda & Sasaki (2018) in an X-ray diffraction pattern, there is a multiple scattering, the waves scattered by one atom (or atomic plane) are also scattered by the other atoms (or atomic planes) and those waves are also subsequently scattered by other atoms and so on. The limits of the Scherrer´s equation have been described by Muniz *et al.* (2016) suggesting that there is a limit of applicability of this equation and found a dependence on the Bragg angle and the absorption coefficient of the XRD pattern. However, their findings are not general.

$$CS = \frac{k\lambda}{\beta Cos\theta} \qquad \text{Eq.6.1}$$

Where λ is the wavelength, k is a constant (0.9), β is the FWHM in radians, and θ is the diffraction angle. For this sample, β and θ were determined in the (002) peak. Scherrer's equation is limited to crystal sizes from 100 to 200 nm. Calculate sizes smaller than this range by this equation has the problem of the separate peak broadening due to the crystallite size from the broadening due to other factors (Holzwarth & Gibson 2011). Crystal size of H-Raw, B-Raw, and P-Raw was calculated using Scherrer's equation.

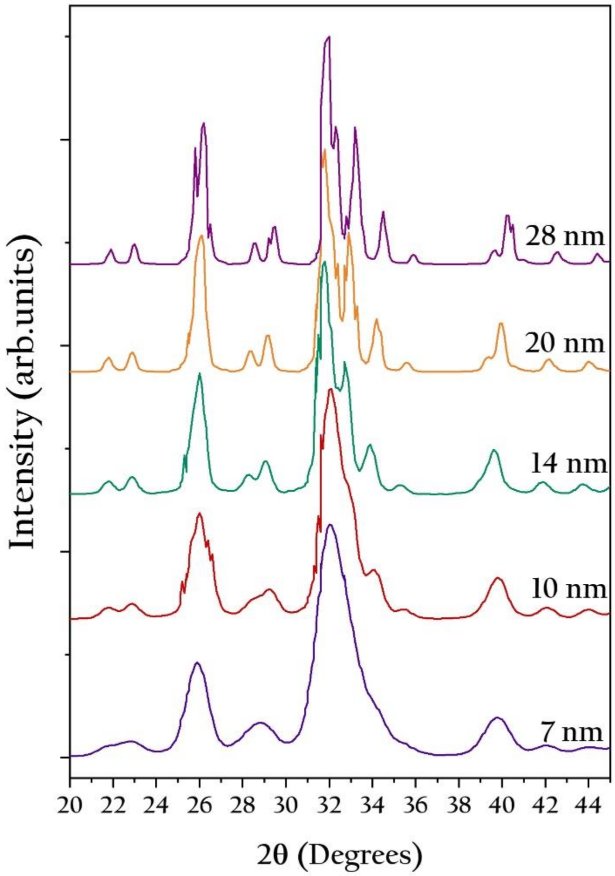

Figure 6. 6 **Simulated X-ray diffraction patterns of hydroxyapatite as a function of the crystal size.**

Figure 6.7 shows the crystal size of biogenic hydroxyapatites (raw and calcined) that was calculated by using the Scherrer's equation using the FWHM value calculated for (002) peak, and by TEM and SEM images processing (ImageJ free software) for raw and calcined samples, respectively. The crystal sizes for raw samples obtained for both methods are consistent between them, which confirms that Scherrer's equation is an excellent tool to determine the crystal size for nanocrystals, but in the case of micron crystals, the limitations of the equation do not allow determining their crystal size. Based on these values, it is clear that the HAp crystals suffered a dramatic change in their sizes which affected the shape of the X-ray diffraction patterns.

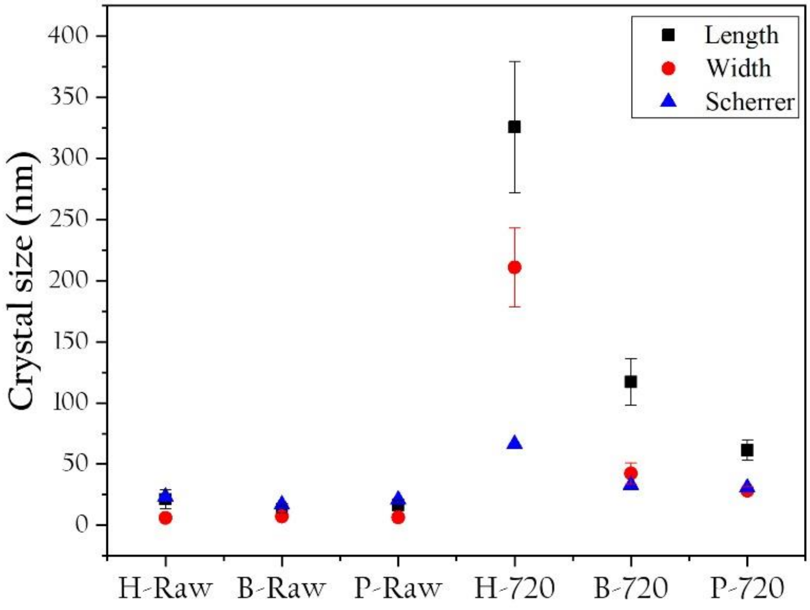

Figure 6. 7 **Crystallite sizes obtained by using Scherrer's equation and by HRTEM and SEM images processing.**

6.6. Discussion

Cleaning processes sometime involve changes in the mineral content (%) because of concentration effects, but in this case, no differences between raw clean bones and samples calcinated at 720°C were found. This fact indicates that the process avoids the loss of the main components of hydroxyapatite. Ca levels are higher for human than for bovine and porcine bone which could be due to the human diet rich in calcium, and that this HAp is carbonated. After calcination, Ca/P atomic ratio does not suffer any change because samples were defatted and deproteinized before the process. Sigma-Aldrich sample showed the highest Ca content; thus, its Ca/P ratio is higher than for pure hydroxyapatite. The presence of the minority minerals depends on several factors such as diet, age, gender, among others. It is also remarkable that the incineration does not affect the mineral content, and the small variations in these values correspond to a concentration effect (Londoño-Restrepo *et al*., 2018). Minoritarian elements can be located as substitutional or interstitial atoms that can change their structure.

HR-TEM images clarify that hydroxyapatite from bovine, porcine, and human bones exhibit nanometer dimensions; however, calcination at 720 °C produces crystal growth until microns. The difference in the crystal sizes reached after the calcination process at 720 °C may be due to the crystal size of the raw samples. All raw crystals are nanometric, but smaller crystals as the human sample have a higher surface area to react, and then bonds are rearranged between the surrounding crystals. Hydroxyapatite from Sigma Aldrich exhibits spherical particles with 48 ± 4 nm with apparent interconnected porosity which means that its process of synthesis developed particles bigger than those for raw biogenic apatites, and a calcination process at elevated temperature was no involved in the synthesis (see Figure 6.3 D). The atomic order showed for H-Raw, B-raw, and

P-Raw in Figure 6.2 A, E and I (see squares), clearly evidenced that the atoms that form these BIO-HAp are ordered into the hexagonal structure. These HRTEM images and the ones reported by other authors such as Xin *et al.* (2010) confirmed this fact. This finding indicates that it is necessary a reinterpretation of the X-ray diffraction patterns for nanocrystals, and of course, there is a misunderstanding related to the poorly crystalline quality of these BIO-HAp (Andrés *et al.*, 2017; Fratzl *et al.*, 2004; Murugan & Ramakrishna 2004; Bala *et al.*, 2011; Paschalis *et al.*, 2011; Giraldo-Betancur *et al.*, 2013; Querido *et al.*, 2018; Hammood *et al.*, 2018).

The nanometer size of HAp from bones can explain some well-established facts reported about the crystalline quality of these kind of samples. X-ray diffraction patterns for nanoparticles are is formed by elastic and inelastic scattering that cannot be separated so far. In this direction, there is a paper "Separating diffraction from scattering: the million-dollar challenge" by Laven 2010, that shows that this is an instrumental and physics problem in different areas where both contributions are present. It means that the calculation of the crystalline percent cannot be obtained in the case of nanoparticles because so far it is impossible to separate the inelastic scattering contribution and the diffracted signal. The patterns for raw HAps have been interpreted as polycrystalline samples with "low crystalline quality," but according to the HRTEM images these samples correspond to ordered HAp nanocrystals. The changes in the crystalline quality (atomic order) are influenced by the inclusion of different ions into the lattice as substitutional or interstitial sites. One of the problems related to the interpretation of the XRD patterns of HAps is the use of the FWHM as a parameter to quantify their crystalline quality. But, by direct inspection of this parameter in raw samples, these peaks are broad. Based on the FWHM of a characteristic peak, low crystalline quality has been reported for BIO-HAp, and the calculation of the crystallinity percentage is carried out considering the complete XRD pattern. However, the broad peaks that the diffractograms display are due to the inelastic scattering originated from the BIO-HAp nanocrystals, the broadening originated by itself diffraction, and the instrumental contribution. It means that the calculation of the percent crystallinity and crystalline quality in nanocrystals must be revised in detail in the future. On the other hand, the value of the FHWM for the H-720 is the lowest one. Here, the interpretation done by different authors is referred as that the FWHM decreases due to an increase of the crystalline quality of the sample, but the incineration process produces a coalescence phenomenon that originates the growth of the crystal and the X-ray diffraction instead inelastic scattering governs this kind of patterns (Londoño-Restrepo *et al.*, 2018). It can be interpreted as follows: first, the raw crystals improved their crystalline quality or due to the heating process the raw samples suffer a coalescence process increasing the crystal size from nano to micro, but it cannot be interpreted saying that the crystalline quality of the sample increases as is commonly reported (Ooi *et al.*, 2007; Sobczak-Kupiec *et al.*, 2013; Londoño-Restrepo *et al.*, 2016; Hammood *et al.*, 2017). Based on our analysis, it is not possible to define raw hydroxyapatites as structures with low crystalline quality.

6.7. Conclusions

The shape and width of the X-ray diffraction pattern for ordered crystals are governed by the crystal size. The broad peaks of the patterns for nano HAp are not necessarily related to disordered crystalline structures.

HRTEM images of the raw clean bones showed ordered structures, which means that the broad peaks of the X-ray patterns are originated by the simultaneous inelastic and elastic scattering produced by the beam/structure interaction. So far, the inelastic contribution cannot be separated from the signal produced by the elastic scattering that forms a diffraction pattern. HRTEM images showed in diluted samples that the needles are produced by transversal view of the elongated plates.

PDF-4 simulations of the effect of the crystallite size on the shape and width of the X-ray diffraction patterns confirm that both elastic and inelastic contributions in ordered BIO-HAp originated broad peaks.

This misinterpretation about the correlation between broad peaks and disordered crystals has caused the erroneous belief that hydroxyapatite nano crystals from mammalian are poorly crystalline, but as it was demonstrated in this work, is that these nanocrystals are ordered as was shown with the HRTEM images.

The XRD pattern of nano crystals is governed simultaneously by elastic and inelastic scattering. The incineration process produces an increase in the crystal size, and a decrease in the FWHM value, which cannot be directly related with an improvement of the crystalline quality. It is the result of the transformation from nano to micro HAp crystals.

From a tissue engineering point of view, these results showed that incineration process can be applied to obtain BIO-HAp, but the XRD patterns must prove that the temperature does not originated changes in its nanometric size.

CHAPTER 7

INFLUENCE OF THE CRYSTAL SIZE ON THE INFRARED AND RAMAN SPECTRA OF HAp OF BOVINE, PORCINE AND, HUMAN BONES

The optical properties of hydroxyapatites and bio hydroxyapatites have been studied using Raman and Infrared spectroscopies to describe their crystalline quality. However, the size of the hydroxyapatite crystals and their crystalline order effects have not been considered yet. This section of the work focuses on the study of the effect of the change in the crystallites size have on the width of the IR and Raman spectra for defatted and deproteinized bones as well as incinerated biogenic hydroxyapatite obtained from bovine, porcine, and human bones. Bone samples were analyzed through Raman and Infrared spectroscopies, X-ray diffraction (XRD), Transmission Electron Microscopy (TEM), Inductively Coupled Plasma (ICP), and Scanning Electron Microscopy (SEM). The Raman and IR spectra for raw samples showed broad bands while after calcination at 720°C became narrow and well defined. TEM images showed that all raw crystallites are ordered nano-plates contrary to the so far well-established concept that biogenic hydroxyapatites have low crystalline quality. X-ray diffraction data confirmed that raw samples display broad peaks which correlated with the HRTEM images of ordered nanocrystals. This fact confirmed that the broad Raman and infrared bands of raw clean bones come from nanocrystal-plates. SEM analysis confirmed the increase in the crystal size after calcination from nano to sub-micron dimensions due to a coalescence phenomenon. These results imply that the interpretation of Raman and IR spectra in the case of HAp nanoparticles has been erroneous These results contribute to the design of biomaterials for tissue engineering based on biogenic hydroxyapatite for bone regeneration.

The physicochemical characterization of raw bones and BIO-HAps obtained through different methodologies is still an open problem due to their complexity. Infrared and Raman spectroscopies have been extensively used to study these materials, monitoring the removal of the organic matrix from the mineral phase as well as to identify different mineral phases and to identify the changes in the crystalline quality of HAp caused by thermal processes (Ooi *et al.*, 2007; Ramirez-Gutierrez *et al.*, 2016). However, no studies about the influence of the crystal size on the vibrational properties (optical) of synthetic and BIO-HAps have been reported. Usually, when these spectroscopies are used to study the vibrational states of the above-mentioned samples (Freeman *et al.*, 2002), the full width at the half maximum (FWHM) of a characteristic peak is used to determine their crystalline quality (Sathyavathi *et al.*, 2015). But this criterion must be discussed in detail in the case of nanostructures.

It is well-established that nanosized crystals produce broader Raman bands than micro-sized ones as has been found for semiconductors (Ehbrecht *et al.*, 1995; Ehbrecht *et al.*, 1997). The phonon confinement model has been proposed to explain Raman spectra in nanosized systems because the surface states must be considered (Li *et al.*, 2000; Sirenko *et al.*, 2000; Swamy *et al.*, 2005; Dogan & Van de Sanden, 2013). According to Gao *et al.* (2016) the underlying mechanism behind the size-dependent Raman shifts is still quite controversial and an open problem. They proposed a theoretical method to explain the quantum confinement effects on the Raman spectra of semiconductor nanocrystals indicating that their shift is originated by two overlapping effects: the quantum effect shift and the surface effect shift. Their calculations showed that there is a small shift in peak position as a function of the crystal size. They also proposed this model for using Raman as a tool to measure crystal sizes in nanostructures.

Different works related to the Raman characterization of nano-synthetic HAp have been published in which the FWHM of the band was not considered in the interpretation. Wopenka & Pasteris (2005) showed that the significantly broader bands for biomaterials are indicative of the shorter-range disorder that these nanocrystalline and carbonated phases have in comparison to those of synthetic hydroxyapatites. Even though they found that the studied biomaterials are in the nanoscale range, they did not consider that Raman dispersion is governed by surface states. The translational symmetry of the crystal is broken at the grain boundaries which results in the appearance of the specific surface and interface vibrational contributions (Gouadec & Colomban, 2007). However, in the case of BIO-HAP, this information is still under discussion.

For the determination of crystallinity in bones using Raman, the FWHM of the phosphate band at 959 cm^{-1} is used because of its intensity and the no overlapping with other bands (De Mul *et al.*, 1988; Freeman *et al.*, 2002; Awonusi *et al.*, 2007). Its calculation is carried out using a single Gaussian curve. The fitted value is reported in wavenumbers, and its inverse is considered as a parameter that determines the crystalline quality of the samples. Nevertheless, this calculation does not make any physical sense when the crystals are at the nano-scale. FT-IR and Raman spectroscopies have also been used to quantify bone mineral crystallinity. Querido *et al.* (2018) developed a methodology based on the ratio between selected bands intensities. The X-ray diffraction peaks of the studied bones, according to their interpretation, have poor crystallinity thus resulting in broad and overlapped peaks. Nonetheless, this is misleading because it is well known that for nanoparticles, their patterns are formed by simultaneous and non-separable elastic and inelastic scattering. Concerning the Raman analysis of the same samples, they found that the bands varied in width and position due to the different degrees of crystallinity, but they did not perform the study of the crystalline quality of the samples by HRTEM.

The analyses of calcium phosphates by vibrational spectroscopies have been performed both from a theoretical and experimental point of view (Rey *et al.*, 2014). De Mul *et al.* (1988) shown that broadening of the IR bands is related to the irregularity of the atomic array, referred to as lattice strain, among others, and they determined the crystallinity of the apatite domains using XRD. This kind of determination at a microscopic scale is difficult, so they chose a crystallinity index obtained from the broadening of the ν_4 apatite band at 600 cm^{-1}. Here, it is essential to point out that the crystal size effects (finite crystal and surface states) were not considered. The same group made the calculation of the IR broadening with a relatively simple inter- and intra-ionic potential (Coulombian) in which all atoms have the same number of bonds, but the surface states break this rule and must be incorporated into the calculation.

On the other hand, the structural properties of HAp from several sources have been studied using X-ray diffraction to obtain information about their crystalline structures, crystalline quality, crystal size, and lattice defects among others. However, Scardi (2008) and Piga *et al.* (2008) pointed out that the XRD analysis and the reliability of the results for nanoscale sizes, as is the case of BIO-HAp, are still an open problem. In these cases, the elastic and inelastic signals are detected at the same time by the X-ray detector, affecting the peak width and shape of the patterns. Patel *et al.* (2015) reported a nanometric size for bovine bone using TEM images, but they pointed out that this sample was amorphous. Nonetheless, a detailed analysis of their HRTEM images showed these to correspond to ordered crystals.

7.1. TEM characterization

Figure 7.1 shows HRTEM images for clean P-Raw (A to D), B-Raw (E to H), and H-Raw (I to L) sample. Figure 7.1 C, G, and K shown that these bones are formed by polycrystalline arrangements of elongated nano-plates crystals while Figure 7.1 B, F, and J clearly shows that they are in fact highly ordered crystals. The crystal size (2D) of these samples was determined using Image J software and are reported as the average value of 25 determinations and correspond to: were: 21 ± 7 nm and 6 ± 1 nm for H-Raw, 13 ± 2 nm and 7 ± 1 nm for B-Raw, and 17 ± 4 nm and 6 ± 1 nm for P-Raw samples, for long and width respectively.

7.2. Mineral composition by ICP

Ca percentage is from 21 to 37% while the P content varies from 9 to 19%. Synthetic HAp 39.89% Ca and 18.5% P. In the same way, Ca/P ratio varies from 1.2 to 2.4 when is 1.67 for pure hydroxyapatite. Moreover, biogenic hydroxyapatites exhibit trace elements as Na, Mg, K, Fe, Al, and Zn with a maximum value of 9500 ppm (0.95%).

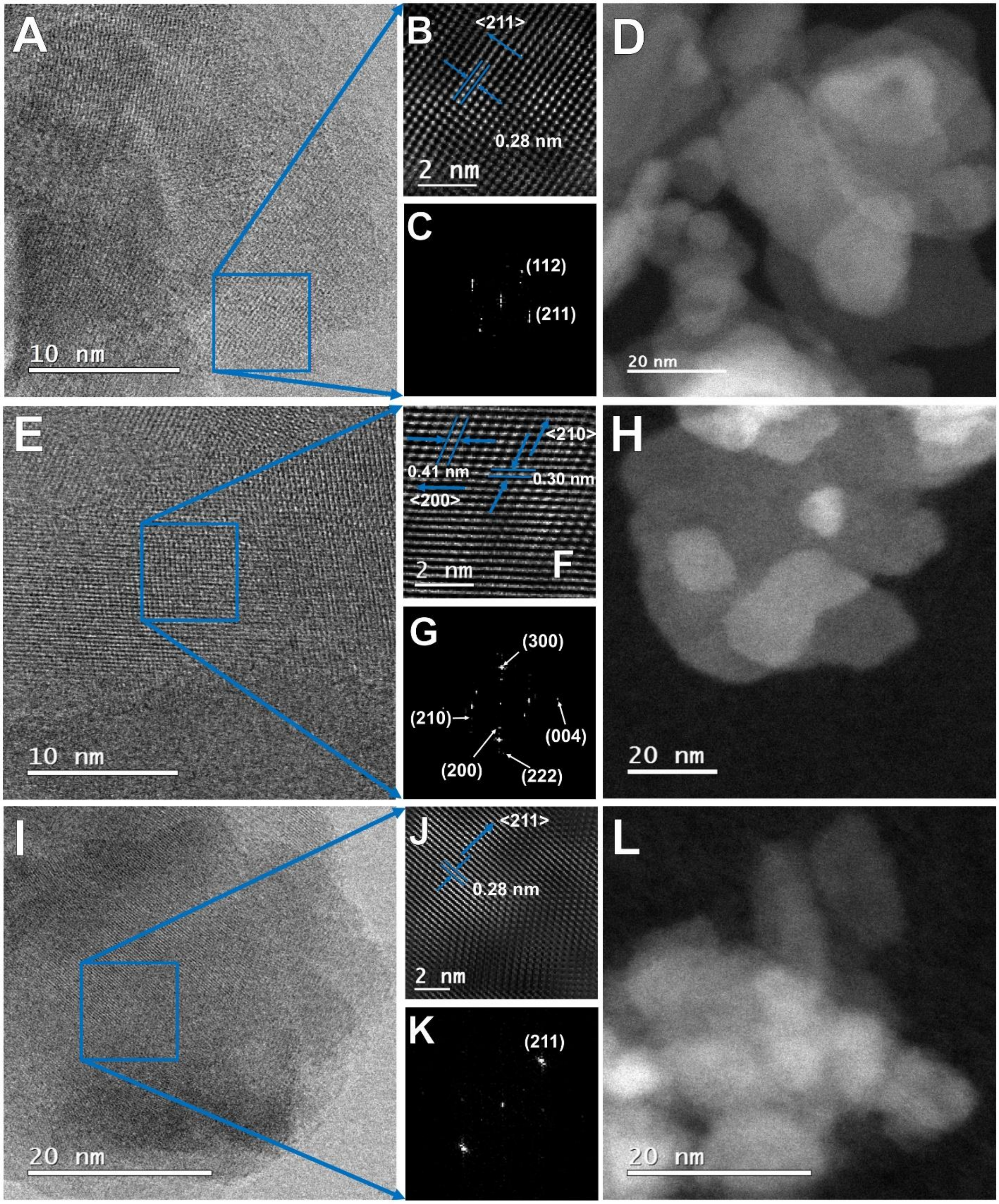

Figure 7. 1 Transmission electron microscopy images of the defatted and deproteinized porcine (A to D), bovine (E to H) and human (I to L) bones.

The Ca and P content for H-Raw, B-Raw, and P-Raw were 28.5 and 10.7%; 22.1 and 12.6%; and 21.2 and 12.5%, respectively; for the incinerated H-720, B-720, and P-720 samples: 37.0 and 15.7%; 31.0 and 18.9%; and 26.4 and 16.8%, respectively. The apparent increases in Ca and P is related to the removal of organic remnants. Ca and P, for the Sigma Aldrich HAp were 32.1 and 10.1 respectively. While other elements such Na. Mg, K, Fe, Al, and Zn were found (Londoño-Restrepo *et al.*, 2018), the presence of these elements changes the dispersion relation for *w* vs *k* and of course the shape and width of the IR and Raman bands.

7.3. SEM analysis

The effect of the incineration process on the crystal size of the calcined samples is showed in Figure 7.2 for P-720 (A), B-720 (B), and H-720 (C) samples. As was mentioned above, these samples were calcinated at 720°C using the same thermal profile. Figure 7.1 showed that the raw samples are nanoplates with dimension around 20 nm length and 5 to 7 nm thick. After calcination, these samples get the following sizes: 70 ± 24 nm length and 46 ± 10 nm width for porcine sample, 52 ± 15 nm length and 36 ± 8 nm width for bovine sample, and finally 190 ± 74 nm length and 175 ± 48 nm width for human.

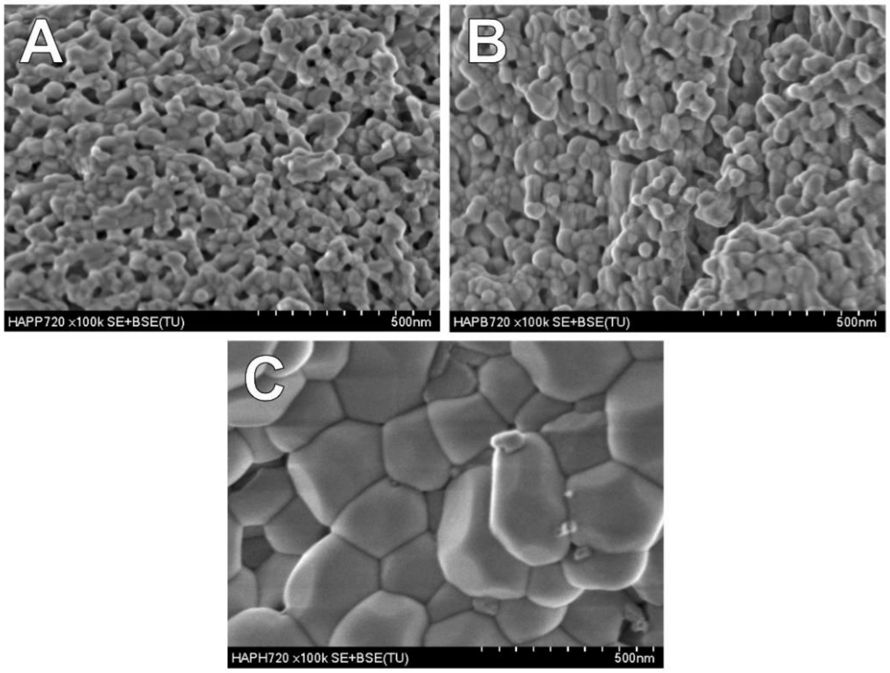

Figure 7. 2 Scanning electron microscopy images of (A) P-720, (B) B-720, and (C) H-720.

7.4. X-ray analysis

Figure 7.3 shows part of the X-ray diffraction pattern of the studied samples from 24.9 to 27° in a 2θ scale corresponding to the (002) crystalline orientation of the Powder diffraction file ICDD card No. 01-084-1998 for synthetic HAp. This peak was chosen because it does not overlap with peaks from other crystalline orientations. The FWHM of this peak was calculated for each one of the samples and it is showed in the inset of this figure. The raw samples exhibited broad peaks and after calcination their width decrease. Figure 7.1 shows that raw samples are constituted by ordered crystals, consequently their peak width are the result of elastic and inelastic diffraction contributions and are not due to a low crystalline quality (order) as have been previously pointed out (Andrés *et al*., 2017; Hammood *et al*., 2018; Querido *et al*., 2018). It is clear that if the raw crystals are nanometric and ordered, these have to influence the vibrational states of the IR and Raman spectra.

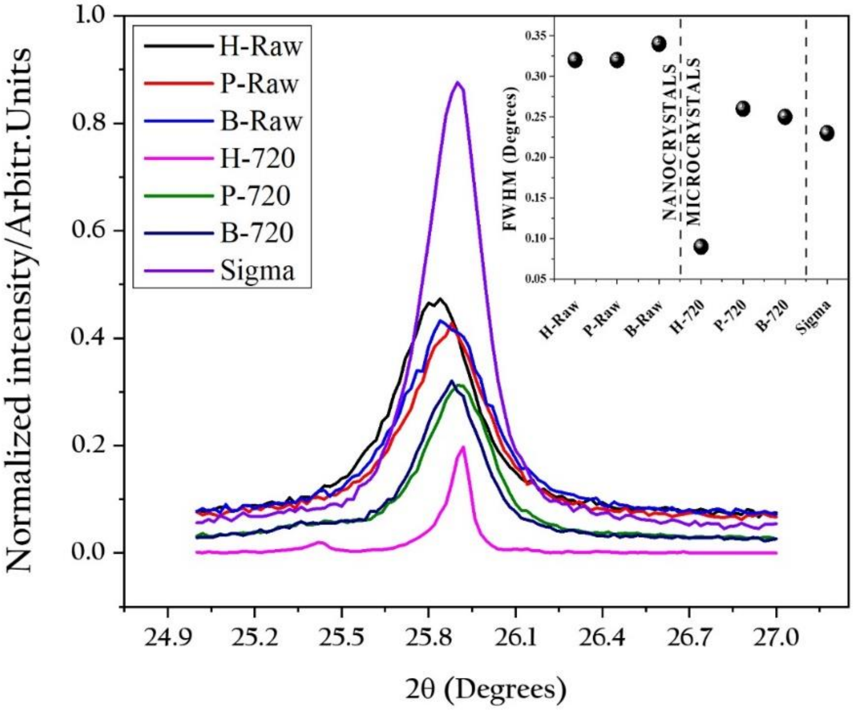

Figure 7. 3 X-ray diffraction patterns for raw, incinerated hydroxyapatites, and synthetic hydroxyapatite (Sigma-Aldrich). The insert shows the changes in the full width at half maximum for the studied samples.

7.5. IR vibrational analysis

Figure 7.4 A to D shows the IR bands located between 400 to 4000 cm^{-1} for raw and calcinated samples, and Sigma Aldrich. The letters correspond to the identification carried out in this work, and these values were compared with others found in the literature in Table 7.1. Figure 7.4 E shows the FWHM for raw and calcined samples, considering the band at 560 cm^{-1}. After calcination, the 560 cm^{-1} band becomes narrow and well defined. Some bands shown in Table 7.1 correspond to organic material and adhered water in the samples which disappear after calcination as H, I, J, K, and L bands (see Figure 7.4 C). Regarding the Sigma Aldrich sample, it does not exhibit any carbonate band then this sample is a non-carbonated hydroxyapatite that contains a carbonyl group. The A, B, and C bands are presented in the studied samples. However, the origin of these bands is not understood.

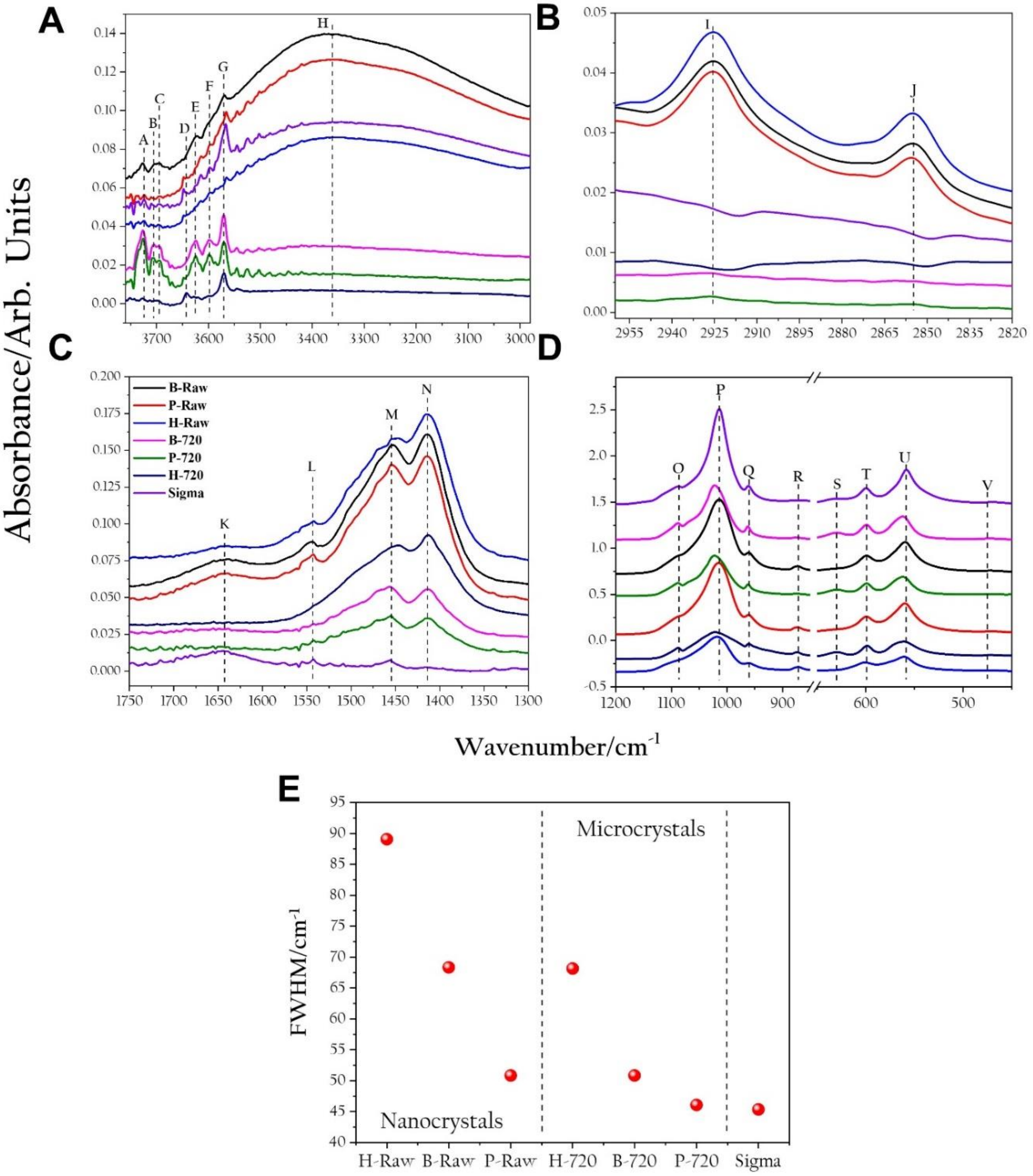

Figure 7. 4 Infrared spectra of raw and calcined samples from human, bovine, and porcine bones, as well as synthetic HAp, in the spectral ranges: (A) 3,700–3,000 cm^{-1}, (B) 2,955–2,820 cm^{-1}, (C) 1,750–1,300 cm^{-1}, (D) 1,200–450 cm^{-1}, and (E) full width at half maximum of 560 cm^{-1} band for all samples analyzed.

Table 7. 1 **Observed infrared band positions for raw bones, sintered hydroxyapatites, and Sigma-Aldrich.**

FT-IR Spectroscopy			
Functional Group	Wavenumber (cm^{-1})*	Wavenumber (cm^{-1})	Reference
ν O-H (HAp)	(D) 3645 ^{ab}	3642-44	Shaltout et al.,2011; Kebiroglu et al., 2017
ν -COOH	(G) 3570 ^{abc}	3571	Bahrololoom et al., 2009
ν O-H (Absorbed H_2O)	(H) 3360 ^{ac}	3367	Shaltout et al.,2011
ν C-H	(I) 2925^{a} (J) 2854^{a}	2923, 2850	Shaltout et al.,2011
Amide I (C=O)	(K) 1642 ^{ab}	1670 1642	Degirmenbasi et al., 2006 Tavakol et al., 2013
Amide II	(L) 1543	1547	Lin et al., 2017
ν_{3as} CO_3^{2-}	(M) 1454 ^{abc} (N) 1412 ^{ab}	1430, 1457 1417 1415-6, 1460-1	Tavakol et al., 2013 Bahrololoom et al., 2009 Shaltout et al.,2011
ν_{1s} CO_3^{2-}	(O) 1088^{abc}	1089	Samanta et al., 2016
ν_3 PO_4^{3-}	(O) 1088^{abc} (P) 1014^{abc}	1099 1043 1033-5	Tavakol et al., 2013 Shaltout et al.,2011 Kebiroglu et al., 2017
ν_1 PO_4^{3-}	(Q) 960^{abc}	960-3 978	Shaltout et al.,2011; Kebiroglu et al., 2017; Bahrololoom et al., 2009 Degirmenbasi et al., 2006
ν_{2as} CO_3^{2-}	(R) 872 ^{ab}	875 871-3	Tavakol et al., 2013 Shaltout et al.,2011; Bahrololoom et al., 2009
ν O-H Libration modes of HAp	(S) 630 ^{abc}	632-3	Kebiroglu et al., 2017 Degirmenbasi et al., 2006
ν_4 PO_4^{3-}	(T) 600 ^{abc} (U) 562 ^{abc}	572, 617 563, 602	Shaltout et al.,2011 Tavakol et al., 2013
ν_2 PO_4^{3-}	(V) 473 ^{abc}	476	Degirmenbasi et al., 2006

* This work. a.- Raw samples. b.- Calcined samples. c.- HAp from Sigma-Aldrich. ν = stretching.

7.6. Raman vibrational analysis

The Raman spectra of the two sets of samples, raw and calcined, which correspond to nano- and micro-crystals, are displayed in Figure 7.5, as for Sigma Aldrich hydroxyapatite. All found Raman bands are shown in Table 7.2. As can be observed from this figure, H-Raw, P-Raw, and B-Raw raw samples have lower intensities and wider band widths as compared to those for the corresponding calcined bone samples; the FWHM value for the synthetic HAp sample lies between the values for the micro and nano samples. After calcination, crystals grow by coalescence

(Londoño-Restrepo *et al.*, 2016), and the surface states decrease while the bulk states govern the Raman spectrum.

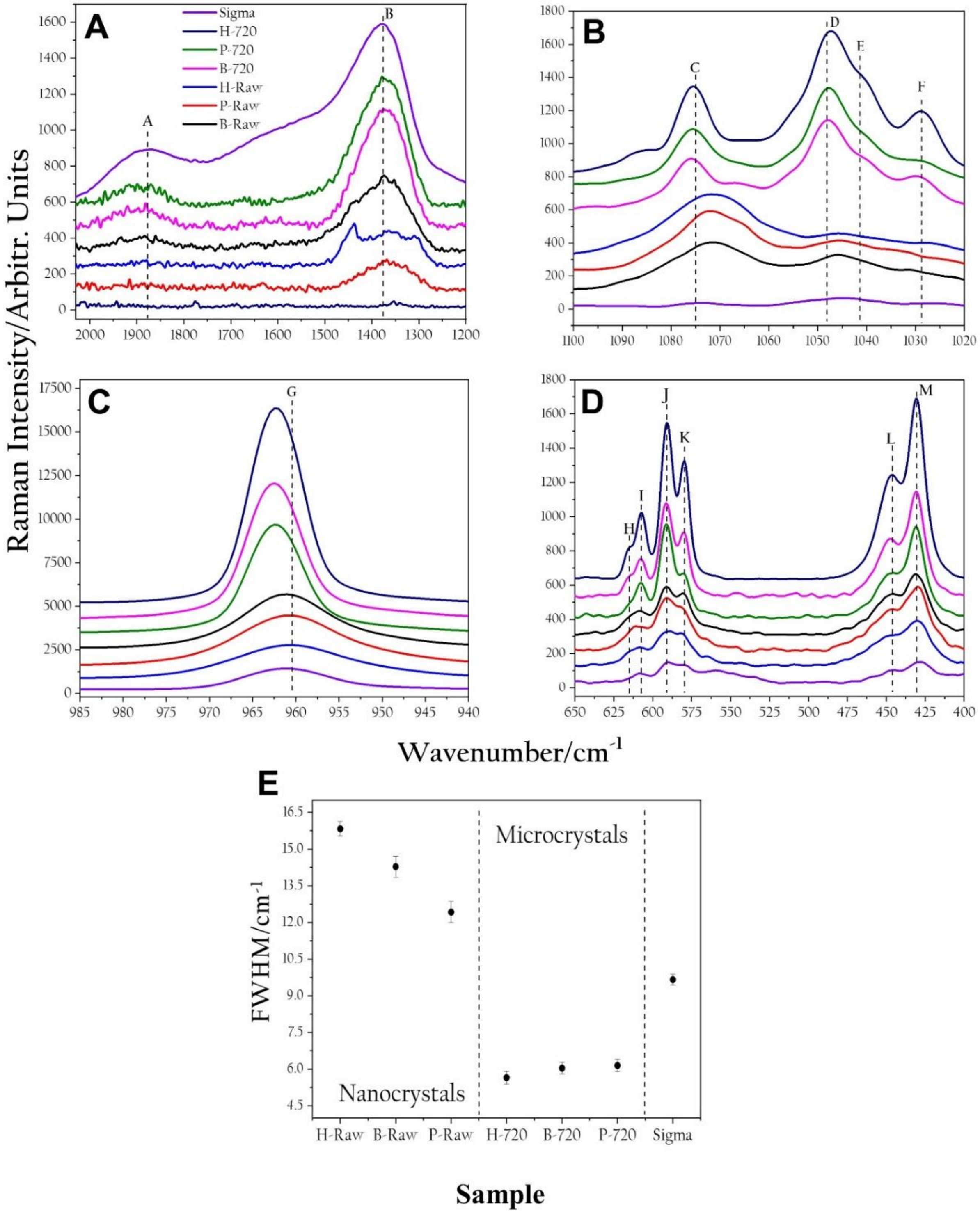

Figure 7. 5 Raman spectra of raw and calcined samples from human, bovine, and porcine bones, as well as synthetic hydroxyapatite, in the spectral ranges: (A) 2,000–1,200 cm^{-1}, (B) 1,100–1,020 cm^{-1}, (C) 985–940 cm^{-1}, (D) 650–400 cm^{-1}, and (E) full width at half maximum of 960 cm^{-1} band for all samples analyzed.

Table 7. 2 **Raman bands of raw and calcined hydroxyapatite as well as hydroxyapatite from Sigma Aldrich.**

RAMAN Spectroscopy			
Functional Group	Wavenumber (cm^{-1})*	Wavenumber (cm^{-1})	Reference
Proteoglycan	(B) 1377 ^{abc}	1375	Mandair & Morris, 2015
ν_3 PO_4^{3-}	(C) 1076 ^{abc}	1076	Awonusi & Morris, 2007; Szcześ et al., 2018
	(D) 1048^{b}	1045-8	Penel et al., 2005; Szcześ et al., 2018; Kumar et al., 2018
	(E) 1041 ^{b}	1035, 1041-3	Mandair & Morris, 2015; Kumar et al., 2018
	(F) 1028 ^{b}	1030	Londoño-Restrepo et al., 2016; Kumar et al., 2018
ν_1 PO_4^{3-}	(G) 960^{abc}	960-1 955-7	Londoño-Restrepo et al., 2016; Mandair & Morris, 2015; Penel et al., 2005; Crane et al., 2006
ν_4 PO_4^{3-}	(H) 614 ^{ab} (I) 607^{abc} (J) 591^{abc} (J) 579^{abc}	579, 591 581 587, 609	Londoño-Restrepo et al., 2016; Mandair & Morris, 2015 Kumar et al., 2018 Londoño-Restrepo et al., 2016; Penel et al., 2005
ν_2 PO_4^{3-}	(L) 446 ^{ab} (M) 430 ^{ab}	430-1, 447-50 425	Mandair & Morris, 2015; Penel et al., 2005 Londoño-Restrepo et al., 2016; Kumar et al., 2018

* This work. a.- Raw samples. b.- Calcined samples. c.- HAp from Sigma-Aldrich. ν = stretching.

7.7. Discussion

Results obtained from TEM analysis confirmed that hydroxyapatite crystals of raw bones are longitudinal nano-plates, which can be correlated with the well-known longitudinal and preferential growth of the bone (Londoño-Restrepo *et al.*, 2018). TEM analyses showed the presence of well-defined nanocrystals and the (112) and (002) planes for bovine bone, (211) for porcine, and (112) for human, thus indicating a high crystalline order. Patel *et al.* (2015) pointed out that raw bone powder from bovine is crystalline based on their TEM images. As was mentioned before, the nano-sized dimensions of the hydroxyapatite crystals from all these bones, have a strong influence on the vibrational properties of bone.

Biogenic hydroxyapatites are no pure as was demonstrated through ICP, but this is not a disadvantage since these element traces help to osteoinductivity when this material is used for medical applications. Ca levels for human samples are higher than for bovine and porcine due to the age of the bones where the samples were obtained; bovine and human samples correspond to adults while porcine is from young animals (5 months old). Other factors as diet, gender, and exercise can also modify their chemical composition (Aguilera-Barreiro *et al.*, 2013). The difference in Ca and P levels between raw bones and calcined samples is due to a concentration effect since raw bone also contain small quantities of organic material. This fact directly affects the Ca/P ratio that is 1.67 for pure hydroxyapatite. In the case of HAp from Sigma-Aldrich, it was found that its calcium value is the highest and its Ca/P ratio is higher than for a pure HAp. The minority elements in the bone can be located as substitutional or interstitial atoms. The structural and vibrational properties of biogenic HAp are affected by the presence of these ions because they modify the chemical environment which in turn modifies the dipolar moment and the polarizability. Here, it is worth noting that Sigma-Aldrich sample does not contain other minority elements.

As was shown in Figure 7.1, H-Raw, P-Raw, and B-Raw bones exhibit elongated nano-plates with sizes that vary from 5 to 30 nm length and from 5 to 7 nm width. It is well known that the calculations to obtain the vibrational states (bands) of a crystalline system assumes an infinite crystal size. However, in the case of nanocrystals, some atoms are located within the crystal, and their coordination number on average is the same, while atoms on the surface exhibit different coordination numbers. Considering this fact, it is expected that the characteristic bands for the vibrational states present in the Raman and infrared spectra of hydroxyapatites suffer changes in the position and width as compared with microcrystals.

During the annealing process P-Raw and B-Raw nanocrystals suffer a coalescence process increasing their size (Londoño-Restrepo *et al.*, 2016). So, crystal sizes range from 52 to 70 nm in length and 36 to 45 nm in width. The calcination process of the H-Raw sample does not follow the same trend, since in this case, the nanocrystals coalesce forming sub-micron crystals with a length of 190 nm and a width of 173 nm. The difference in size the P-Raw and B-Raw crystals reached after their annealing process compared to that obtained for H-Raw is related to their respective chemical composition and age. Rendon & Serna (1981) studied the effect of the crystal size on the infrared spectra of hematite formed between 250 to 600°C; they showed that the differences in the infrared spectra originated by variations in the size and shape of the particles. Through a detailed analysis of the IR bands, the bandwidth of B-Raw, P-Raw, and H-Raw samples exhibited broad bands in comparison to calcinated samples that showed narrow bands. The decrease of the bandwidth is originated in part by the growth of the crystals size and to the possible changes of the crystalline quality of these BIO-HAp (Aguilera-Barreiro *et al.*, 2013; Londoño-Restrepo *et al.*, 2016). Here, it is important to point out that if the crystal size increases, the number of vibrational states on the surface decreases, then the FWHM of the samples is not influenced by these states and becomes narrow and well defined. Furthermore, taking into consideration the arguments stated above on the difference in coordination number for atoms in the crystals and on the surface, the position and width of Raman and IR bands are expected to change when crystals of nano size and micro size are analyzed and compared.

The FWMH measured of the Raman spectra showed a clear difference between nano and micro-sized crystals. The model to calculate the Raman spectra of a material assumes that the crystal is infinite, however, advances in nanoscience and nanotechnology have made necessary to include finite size effects on the Raman and IR spectra to explain their features. The interpretation of the spectra plays a primary role in the case of nanoparticles as quantum dots (Ehbrecht *et al.*, 1995; Ehbrecht *et al.*, 1997). The analysis of the experimental Raman spectra is done considering the confinement effect due to the finite size of the nanoparticles. The broadening of Raman bands (phonons) is governed by factors such as varied sizes, orientation, and shapes of the nanoparticles.

Traditionally high FWHM values have been associated to crystals with low crystalline quality. However, in the case of biogenic hydroxyapatite nanocrystals, the high values they show are associated to size effects. Here, it is important to highlight that the decrease in the FWHM for ν_1 PO_4^{3-} after incineration process is due to an increase in the crystallites size as was demonstrated by Londoño-Restrepo *et al*., (2018) and measured in this work through SEM (see Figure 7.2). Thus, it is not necessarily the result of the improvement of the crystalline quality of the HAp crystals, as it is frequently mentioned in the literature.

7.8. Conclusions

Infrared and Raman spectroscopy were used to analyze the effects that the change in the crystal size has on the FWHM for raw and calcined bones. HRTEM images showed that H-Raw, P-Raw, and B-Raw are elongated nanoplates displaying a high crystalline order, as is opposed to common claims about the low crystalline quality that biogenic hydroxyapatites have. Besides, a calcination process of the raw samples at 720°C gave, as a result, the formation of microcrystals as was shown in the SEM images.

X-ray diffraction patterns showed broad peaks for raw samples and narrow peaks after calcination, that is the result of the growing process from nano to microcrystals, originating a decrease in the FWHM, which is not necessarily related to an increase in the crystalline quality as it has been pointed out in the literature before.

The infrared and Raman spectra of raw and calcined samples displayed marked differences. The Raman and IR broad bands found in raw samples are related to the nano size of the crystals and not to the low crystalline quality while the narrow bands correspond to the increase of the crystal size, bulk and surface phonon states govern the width of the bands. Thus, the calculation of crystalline quality in the nanocrystals using the FWHM of Raman, IR, and X-ray cannot be carried out.

CHAPTER 8

IN SITU STUDY OF BOVINE HAp DURING THE CALCINATION PROCESS

HAp from mammals has suitable crystal size, composition, structure, morphology, and porosity to be used as a replacement material. Moreover, at a crystallographic level, the complexity of its structure is higher due to the presence of ions traces and its different stoichiometry. For this purpose, incineration processes have been carried out as a method to obtain defatted and deproteinized BIO-HAp from mammalian bones. Intrinsic and extrinsic issues influence this process. The bone source, the mammal's age, diet, and physical activity are intrinsic parameters; while testing variables such as heating rate (Londoño-Restrepo *et al.*, 2016), sintering time (Ramirez-Gutierrez *et al.*, 2017), temperature (Ooi *et al.*, 2007; Herliansyah *et al.*, 2009), cooling rate (Ramirez-Gutierrez *et al.*, 2016), and atmosphere (Haberko *et al.*, 2009) are considered extrinsic variables that must be controlled. The complete removal of the organic material from the microparticles formed by crystalline nanometric hydroxyapatite is fundamental for clinical applications due to mainly two reasons: guaranteeing the safety of the patient and the suitable porosity that allows the flux of blood plasma drawn from the patient, which starts the bone regeneration process. Some methods consider organic material removal as a preliminary step before calcination by using acids, bases, or oxidizing agents (Haberko *et al.*, 2006; Czerniczyniec *et al.*, 2007), while other methods avoid this step and incinerate directly (Khoo *et al.*, 2015). It is worth noting that some of these processes can change the mineral phase as well. For that reason, the use of acids and bases must be controlled through low concentrations and few exposure times. Both methods, chemical removal and direct calcination have some disadvantages; in the former, chemical agents can affect not only the organic phase but also the mineral one. Whereas in the latter, some ions from the organic phase of the bone remain in the final HAp, changing its mineral content (Londoño-Restrepo *et al.*, 2018). Even though it is well known that for temperatures about

600°C, the organic phase is totally degraded (Londoño-Restrepo *et al.*, 2016; Ramirez-Gutierrez *et al.*, 2017), calcination processes above this temperature are commonly reported without considering changes in the inorganic phase of the bone.

Several testing temperatures ranging from 500 to 1400 °C have been reported as optimal to obtain BIO-HAp (Su-Hyang *et al.*, 2004; Goller *et al.*, 2006; Herliansyah *et al.*, 2009; Kusrini and Sontang 2012; Niakan *et al.*, 2017). Many of these works are supported on the high crystalline quality obtained for the samples tested; however, structural and morphological changes of the hydroxyapatite from mammalian bone have not been considered.

Physicochemical properties of BIO-HAp have been usually studied *ex situ*, i.e. samples are analized after thermal processing. Nonetheless, the understanding of these transformations is fundamental for many applications and it requires some *in situ* analysis as X-ray diffraction discerns structural changes as temperature changes. *In situ* analysis opens a new window for potential applications of BIO-HAp.

Shih *et al.* (2006) studied *in situ* using HT-XRD, the phase formation, crystal size, and the evolution of diffraction patterns from 25 to 1500°C using hydroxyapatite precursors. They found that the crystal size values (Scherrer equation), have no variations as the tested temperatures changed. Aarthy *et al.* (2019) explored the effect of the sintering time on naturally obtained hydroxyapatite by calcination from 600 to 900°C and 1100-1400°C. They determined crystallite sizes ranging from 15.1 to 22.9 nm using the (211) plane and Scherrer's equation. Nevertheless, their own SEM images revealed crystallites bigger than 2 μm for calcination at 1400 °C.

Nakamura *et al.* (1990) studied the thermal lattice expansion of calcined synthetic hydroxyapatite through high-temperature X-ray diffractometry from 25 to 1150 °C at 10°C/min heating rate. However, patterns were recorded every either 50 °C or 100 °C, and the actual effect of the heating rate was not explored. Fischer *et al.* (1983) also studied the lattice thermal expansion of a hydroxyapatite (Baker) between 22 and 1000 °C every 200 °C by high-temperature X-ray diffraction method, but they calcined the sample at 1200 °C for 4 h previously to the X-ray test which means that they could not analyze the behavior of hydroxyapatite during calcination because structural and morphological changes had already happened. Perdok *et al.* (1987) determined a and c values for synthetic hydroxyapatite prepared at 20, 192, 384, and 576 °C using a Guinier-Simon focusing scanning camera. They reported 9.487 Å and 6.929 Å for a and c, respectively. However, they omitted to mention the heating rate they used.

This section of the work aims to study the compositional, thermal, and morphological changes as well as *in situ* High Resolution X-ray diffraction of HAp from bovine femur bone during controlled calcination processes from 400 to 900 °C every 20 °C, to evaluate the time evolution of the XRD patterns for heating rates of 3, 6, and 9 °C/min as well as the changes of linear thermal expansion coefficient for a and c lattice parameters, and volume fraction.

8.1. Chemical composition of the bovine bone and BIO-hydroxyapatites

One of the main advantages of BIO-HAp with respect of HAp is the presence of traces of ions as already mentioned. The knowledge of the chemical composition of the bone before any thermal processing is fundamental to understand physicochemical transformations as a function of the such variables. Table 8.1 exhibits Ca/P atomic ratio and the mineral content of minority ions for raw bone as well as calcined samples at 700, 800 and 900 °C heated at 3, 6, and 9 °C.

Table 8. 1 Mineral content of Raw bovine bone powder and calcined hydroxyapatite at 700, 800, and 900 °C and heated at 3, 6, and 9 °C/min.

Sample		Ca/P	Na (mg/Kg)	Mg (mg/Kg)	Ba (mg/Kg)	Zn (mg/Kg)	S (mg/Kg)
Raw		1.40	4708 ± 250	4156 ± 230	175 ± 22	83 ± 5	665 ± 45
700 °C	3 °C/min	1.27	6362 ± 318	5433 ± 270	249 ± 12	114 ± 6	298 ± 15
	6 °C/min	1.27	6403 ± 255	6202 ± 310	268 ± 13	128 ± 6	287 ± 14
	9 °C/min	1.26	6309 ± 250	6273 ± 315	265 ± 13	128 ± 6	318 ± 16
800 °C	3 °C/min	1.26	6402 ± 256	6327 ± 300	242 ± 12	112 ± 6	372 ± 19
	6 °C/min	1.26	6346 ± 250	6262 ± 313	270 ± 14	127 ± 6	383 ± 19
	9 °C/min	1.25	6417 ± 260	6168 ± 308	248 ± 12	133 ± 6	359 ± 18
900 °C	3 °C/min	1.26	6331 ± 310	6183 ± 258	259 ± 13	126 ± 6	368 ± 18
	6 °C/min	1.26	6295 ± 315	6311 ± 289	278 ± 14	129 ± 6	389 ± 19
	9°C/min	1.26	6302 ± 265	6322 ± 283	271 ± 13	130 ± 6	402 ± 20

Regarding Ca/P atomic ratio, this value decreases for all calcined samples because of a concentration effect since remnants of the organic phase were completely removed (Londoño-Restrepo *et al.*, 2018). Although Ca/P ratio does not change as the sintering temperature increases, it is worth noting that these values near to 1.27 are lower than those found in pure stoichiometric hydroxyapatite (1.67) which indicates all samples are calcium deficient (Ishikawa *et al.*, 1993; Gross & Berndt, 1998; Wang *et al.*, 2017). There is also a concentration issue after calcination for the trace elements (Na, Mg, Ba, K, and Zn), but in the case of sulfur (S), it exhibits entirely different behavior.

8.2. Bone characterization

Figure 8.1 A shows a SEM image for a bone lamella taken at 100 000× which allowed to determine that this sample is a percolated granular system made of nano-crystal plates from 10 to 20 nm in diameter where crystals are aligned in the same crystallographic direction. Figure 8.1 B shows hydroxyapatite crystals after milling until obtaining a particle with 147 µm particle size where the oriented lamellar formation was wholly lost, but the percolative arrangement is still present because the tertiary porosity of the bone, which is in the nanoscale has not disappeared (Londoño-Restrepo *et al*., 2019b).

Figure 8.1 C to F shows HR-TEM images for clean bovine bone powder. According to this figure, BIO-HAp is formed by elongated nano polycrystalline plates. The FFT image (Figure 8.1 E) shows the most intense points that correspond to those 222, 210, 002, and 004 planes that were all identified according to the ICDD card No. 00-009-0432 and that correspond with the following plane spacing d_{hkl} 0.1993, 0.3634, 0.3433, and 0.1714 nm, respectively (Figure 8.1 C and D). Moreover, Figure 8.1 D TEM image revealed lattice fringes with an interplanar spacing of 0.20 and 0.34 nm, which correspond with ‹111› and ‹001› crystalline family of directions of HA. Although BIO-HAp crystals are commonly reported as poorly crystalline, the ordered atomic arrangement of these crystals is appreciated in this figure. Thus, that assertion has been misinterpreted because of the nanometric size of the crystals and the level of organic material present in the sample. Crystal size (2D) is 7 ± 1 nm width and 13 ± 2 nm length, which confirm the nanometric character of these crystals. Figure 8.1 F dark-field TEM image shows the presence of hydroxyapatite clusters formed by plate-like nanocrystals.

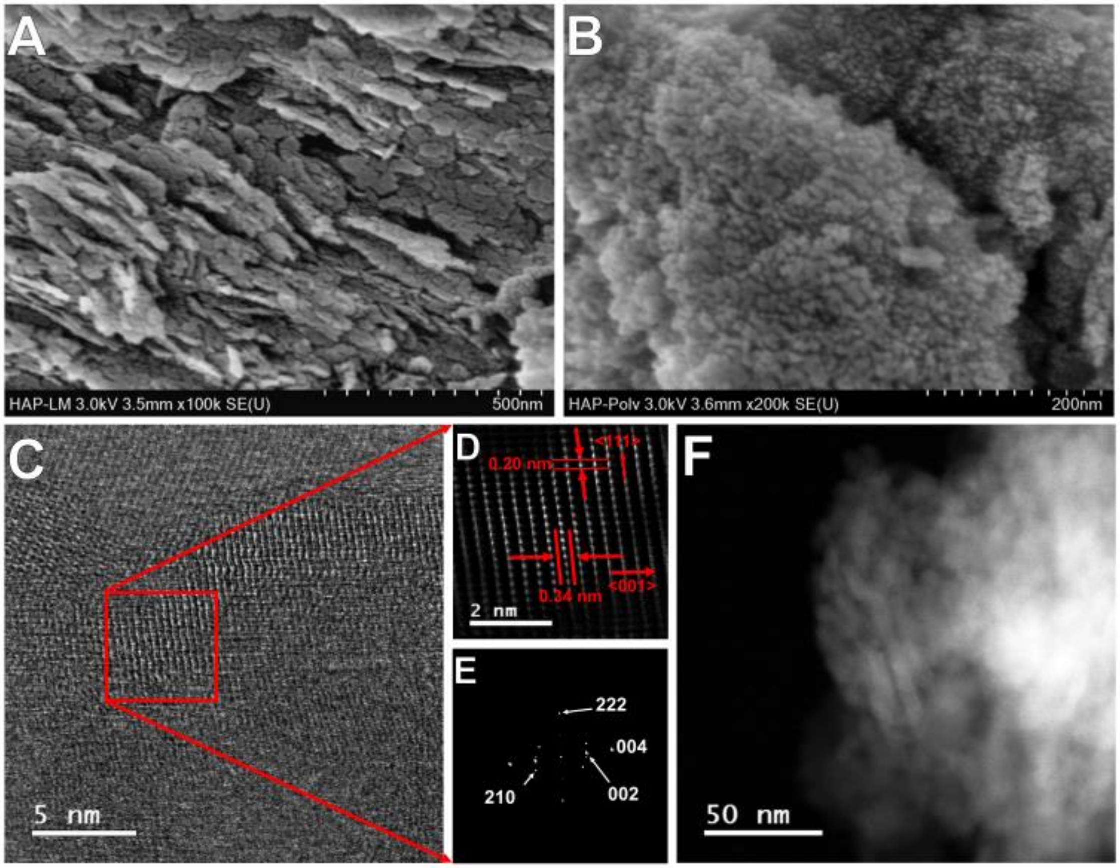

Figure 8. 1 (A) SEM image of a bone lamella taken at 100 000× and (B) SEM image for bovine bone powder taken at 200 000×. (C-D) HR-TEM image for hydroxyapatite from bovine bone where the interplanar distances were calculated. (E) FFT generated from the HR-TEM image and dots were indexed. (F) Dark-light HR-TEM image shows the morphology of hydroxyapatite crystals from bovine bone.

8.3. HR-SEM

Figure 8.2 shows HR-SEM images of raw BIO-HAp crystals (A; 100 000×) and calcined ones in a furnace from 500 to 820°C (B-R; 150 000×) every 20 °C at a heating rate of 6°C/min. Bone tertiary porosity is still present for samples calcined up 700 °C (Figure 8.2 L) when crystals have grown because of coalescence phenomenon and densification by surface diffusion (Bailliez & Nzihou, 2004) as a result of the highly reactive surface of that kind of crystals and the energy provided by the annealing temperature. Though this mechanism, hydroxyapatite crystals enhance their size as hexagonal rods with such as layers on their surface (Figure 8.2 R).

8.4. *In situ* X-ray analysis

Figure 8.3 shows the *in situ* HT-XRD patterns for clean bovine bone powder from 24 to 34° in 2θ scale as a function of the temperature from 400 to 900°C every 20°C for the three heating rates 3, 6 and 9 °C/min as well as clean bone without calcination. The following crystalline planes were found according to the ICDD card No. 00-009-0432 for a hexagonal lattice, in all cases without dependence on the heating rate: (002), (102), (120), (211), (112), (300), and (202). All patterns were taken from 5 to 80°, but only presented from 24 to 34° for graphical reasons.

Table 8.2 shows the lattice parameters of hydroxyapatite from bovine bone powder calcined from 400 to 900 °C at 3, 6, and 9 °C/min. Lattice parameters of this sample at room temperature were a = 9.443 Å and c = 6.893 Å, while for synthetic hydroxyapatite a and b have been reported as 9.418 and 6.884 Å, respectively, according to the ICCD card No. 00-009-0432. This lattice expansion may be due to the presence of substitutional ions and the presence of carbonate in the hydroxyapatite lattice.

TEC values for metals and HAp should be close over a wide range of temperatures to produce coatings with improved bonding strength (Nakamura *et al.*, 1990). Here, it is remarkable that the presence of the substitutional ions as Na, Mg, and K, induces higher lattice expansion (Ivanova *et al.*, 2001). Figure 8.4 A shows the thermal expansion percentage of a and c lattice parameters ($\Delta a/a$ and $\Delta c/c$) as a function of the heating rate. Two regions are observed for $\Delta a/a$ %, but in the case of $\Delta c/c$ %, a linear behavior is found. The percentage of thermal expansion in a-direction for samples calcined from 400 to 900 °C was: 0.14-1.09, 0.21-1.10, and 0.19-1.19% for hydroxyapatite calcined at 3, 6, and 9 °C/min, respectively. In the case of c-direction, this expansion was: 0.35-1.10, 0.38-1.13, and 0.42-1.19%, for each heating rate.

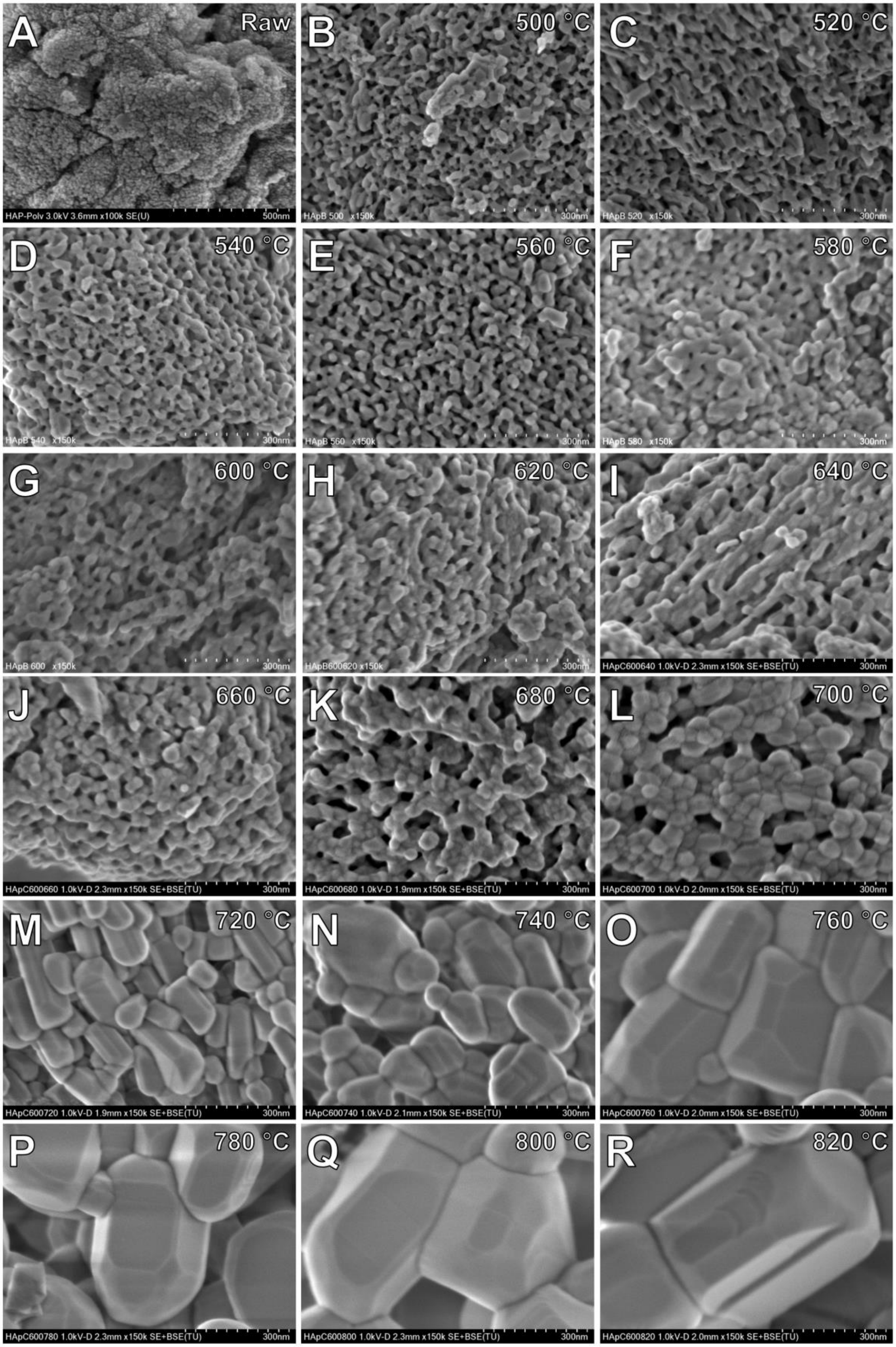

Figure 8. 2 (A) Raw bovine bone powder. (B-R) ex situ SEM images for hydroxyapatite crystals sintered from 500 to 820 °C.

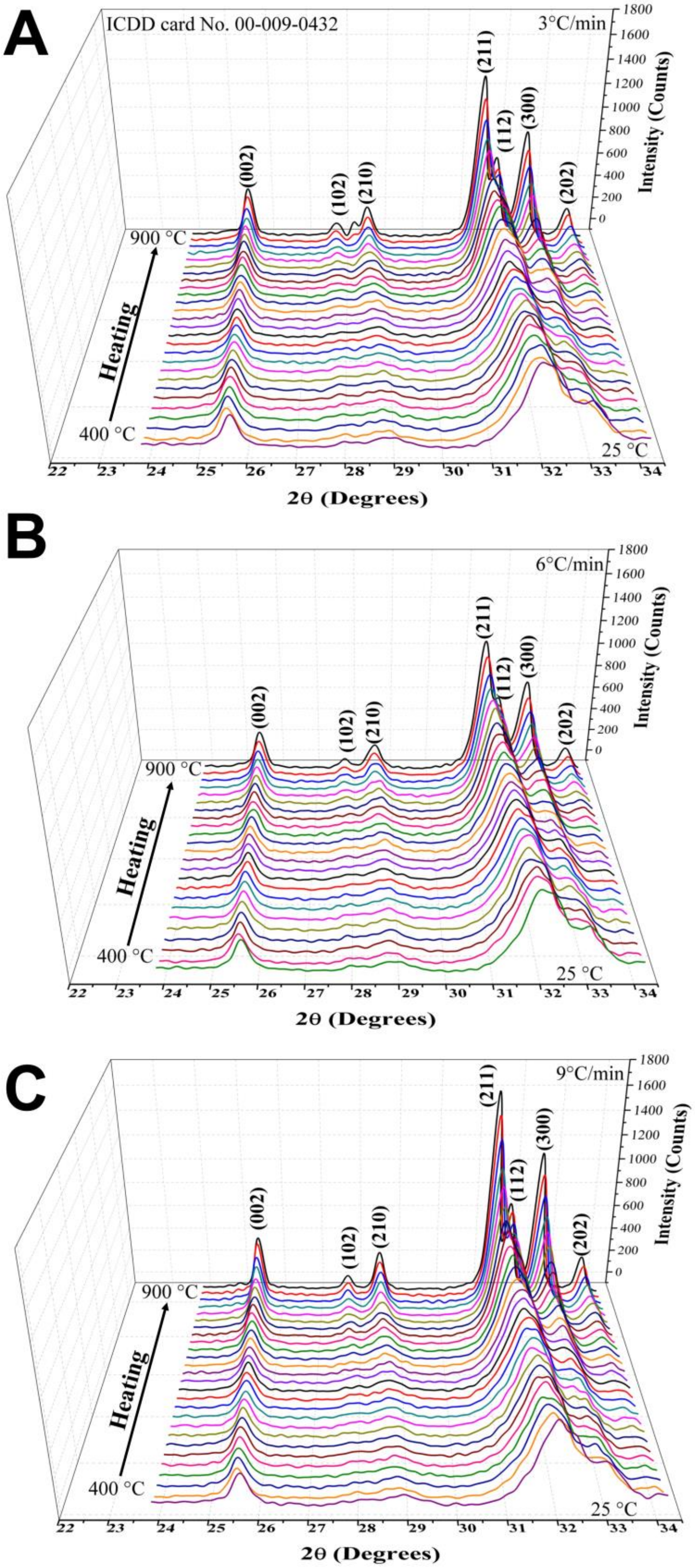

Figure 8. 3 *In situ* HT-XRD patterns for bovine bone powder calcined from 400 to 900 °C every 20 °C and heating rates of (A) 3 °C/min, (B) 6 °C/min, and (C) 9 °C/min.

Table 8. 2 Change of the *a* and *c* lattice parameters of hydroxyapatite throughout the HT-XRD experiment.

T (°C)	Lattice parameters					
	a (Å)			*c* (Å)		
	3 °C/min	6 °C/min	9 °C/min	3 °C/min	6 °C/min	9 °C/min
400	9.457	9.463	9.461	6.917	6.919	6.922
420	9.459	9.466	9.466	6.920	6.922	6.925
440	9.466	9.468	9.472	6.923	6.925	6.927
460	9.469	9.471	9.476	6.925	6.927	6.929
480	9.473	9.472	9.480	6.928	6.929	6.932
500	9.478	9.476	9.483	6.930	6.932	6.934
520	9.479	9.478	9.488	6.932	6.934	6.936
540	9.483	9.483	9.491	6.934	6.935	6.938
560	9.487	9.486	9.493	6.936	6.938	6.941
580	9.488	9.489	9.496	6.939	6.940	6.942
600	9.491	9.492	9.498	6.940	6.942	6.945
620	9.495	9.494	9.500	6.943	6.944	6.947
640	9.498	9.500	9.503	6.945	6.947	6.949
660	9.500	9.504	9.512	6.947	6.949	6.951
680	9.509	9.508	9.515	6.948	6.951	6.953
700	9.513	9.511	9.519	6.951	6.953	6.955
720	9.518	9.516	9.523	6.952	6.955	6.957
740	9.522	9.522	9.528	6.954	6.957	6.959
760	9.524	9.527	9.532	6.956	6.958	6.961
780	9.528	9.530	9.537	6.958	6.960	6.963
800	9.531	9.532	9.542	6.959	6.962	6.965
820	9.535	9.536	9.544	6.961	6.963	6.967
840	9.540	9.538	9.548	6.964	6.965	6.969
860	9.542	9.542	9.551	6.966	6.967	6.971
880	9.545	9.545	9.553	6.968	6.969	6.973
900	9.546	9.547	9.556	6.969	6.971	6.975

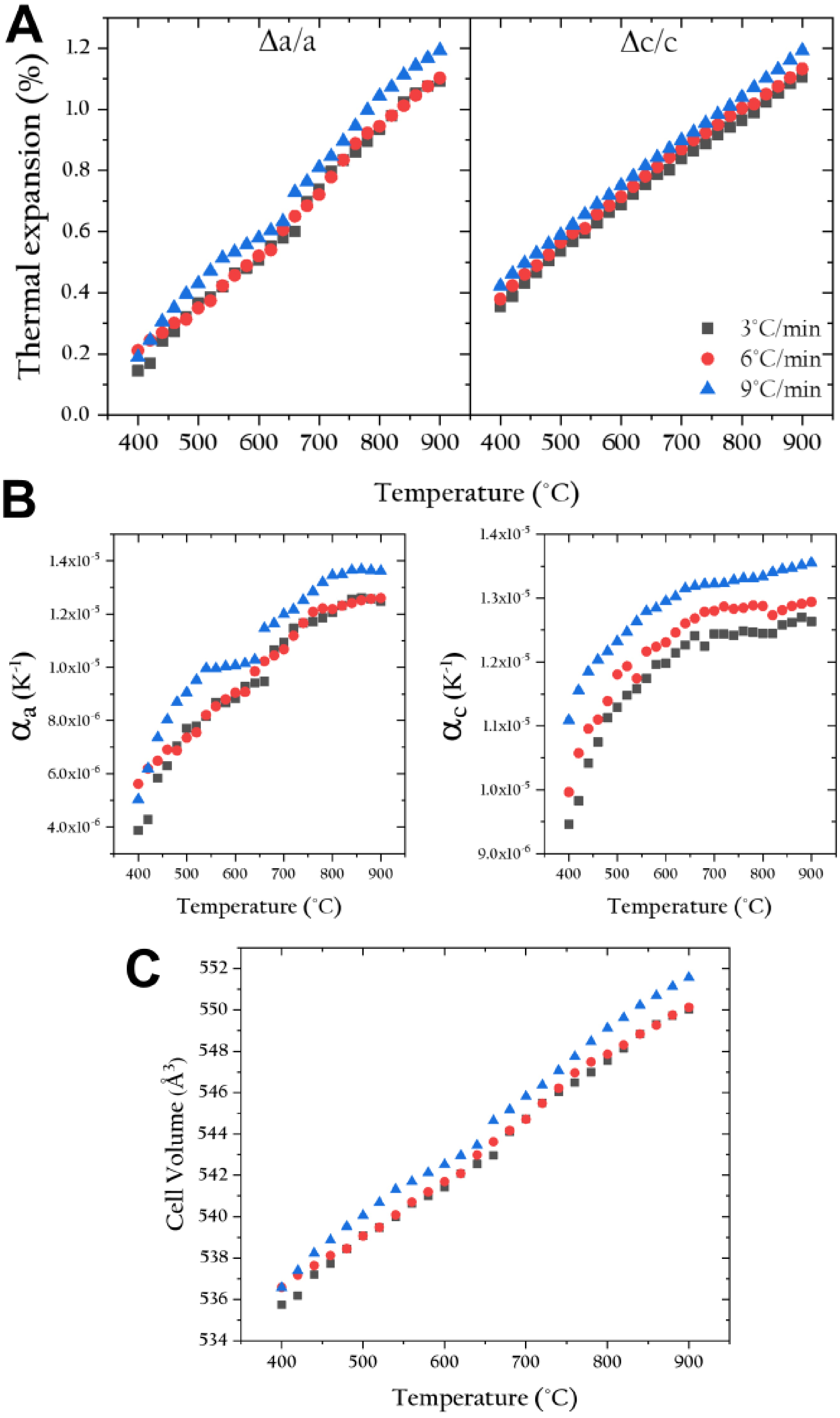

Figure 8. 4 (A) Percentage of thermal expansion for a and c direction of the hexagonal lattice of hydroxyapatite from bovine bone. (B) Thermal expansion coefficient for a and c lattice parameters. (C) Change in the cell volume as a function of the temperature and heating rate.

Figure 8.4 B the linear TEC for *a* (α_a) and *c* (α_c) lattice parameters from data raised from the HT-XRD patterns. In the case of α_a, four regions are identified based on the slope of the curves and values of α_a are shown in Table 8.3.

The first region from 400 to 520 °C is attributed to dehydration and loss of remaining organics. The second region starts at 540 °C and finishes at 640 °C. In this region, the slope decreases, and the dilatation was almost constant, which may be related to thermal expansion but not significant crystal growth. The third region corresponds to crystal growth and lattice expansion in which hydroxyapatite reaches micrometric sizes. This region starts at 660 °C and finishes at 820 °C. Finally, a fourth region is found from 840 to 900 °C, in which the material does not exhibit thermal expansion. In the case of thermal expansion coefficient for c direction (α_c), only three regions as a function of the slope can be observed: 400-460 °C, 480-660 °C, and 680-900 °C, and αc are shown in Table 8.4. Finally, Figure 8.4 C exhibits the volume increasing as a function of the temperature and heating rate. Samples incinerated into the temperature chamber of the diffractometer reached volume increases of 3.3, 3.3, and 3.6% for 3, 6, and 9 °C/min, respectively.

Table 8. 3 **Linear thermal expansion coefficient in a direction.**

Temperature range (°C)	Heating rate (°C/min)	α_a (K^{-1})
400-520	3	3.8×10^{-6} — 7.8×10^{-6}
	6	5.6×10^{-6} — 7.5×10^{-6}
	9	5.0×10^{-6} — 9.5×10^{-6}
540-640	3	8.2×10^{-6} — 9.4×10^{-6}
	6	8.2×10^{-6} — 9.8×10^{-6}
	9	9.9×10^{-6} — 10.0×10^{-6}
660-820	3	9.5×10^{-6} — 12.3×10^{-6}
	6	10.2×10^{-6} — 12.3×10^{-6}
	9	10.3×10^{-6} — 13.5×10^{-6}
840-900	3	12.5×10^{-6}
	6	12.6×10^{-6}
	9	13.6×10^{-6}

Table 8. 4 **Linear thermal expansion coefficient in *c* direction.**

Temperature range (°C)	Heating rate (°C/min)	α_c (K^{-1})
400-460	3	9.5×10^{-6} — 10.7×10^{-6}
	6	10.0×10^{-6} — 11.1×10^{-6}
	9	11.1×10^{-6} — 12.0×10^{-6}
480-660	3	11.1×10^{-6} — 12.4×10^{-6}
	6	11.4×10^{-6} — 12.7×10^{-6}
	9	12.2×10^{-6} — 13.2×10^{-6}
680-900	3	12.4×10^{-6} —12.6×10^{-6}
	6	12.7×10^{-6} — 12.9×10^{-6}
	9	13.2×10^{-6} — 13.5×10^{-6}

Changes in the crystallite size can be evaluated by analyzing the changes in the FWHM of a single peak. Figure 8.5 A shows the FWHM evaluated for the (002) peak for all HT-XRD patterns. Two regions of interest are indicated based on the behavior of the FWHM values (see HR-SEM images, Figure 8.2), Region I corresponds with hydroxyapatite nanocrystals while Region II is for micrometric crystals. In turn, Region II is divided into two sections: II-a and II-b. Part II-a corresponds to a sharp decreasing of the FWHM values while in section II-b they keep constant. The inelastic scattering contribution is evidenced by these large FWHM values around 0.4 degrees, which indicate the presence of nanocrystals. The sharp decrease of the FWHM when samples reach about 700 °C for the three heating rates indicates a remarkable change in the crystal size from nanometric to micrometric scale as was corroborated in Figure 8.2. Crystal growth shows a dependence on the heating rate after the event at 700 °C, the temperature in which higher heating rates produce higher crystal size increments.

On the other hand, the crystal size of BIO-HAp is commonly calculated using Scherrer's equation, but it has been indiscriminately used for all crystallite sizes. Hence, the calculations of crystallite size for all calcined samples were carried out only to prove that these values do not correspond to real values (Figure 8.5 B). In the case of clean bone powder, β and θ were determined for the (002) peak, and the crystal size was 19.93 nm, which does not agree with the dimensions found by TEM analysis. The effect of the crystalline size on the shape and width of XRD patterns was evaluated by a simulation done using PDF-4 software to be compared with samples calcined into the temperature chamber of the diffractometer at 400, 720, and 900 °C (Figure 8.5 C). Simulated patterns with crystallite sizes of 10, 16, and 25 nm matched with those for calcined samples, respectively. Here, it is worth noting that those values do not correspond to experimental crystallite sizes of the patterns of the calcined sample in the chamber at 400, 720, and 900 °C. It means that indeed, XRD peaks become narrow as long as crystallite size increases, but the crystallinity of the sample is also contributing to the peak width.

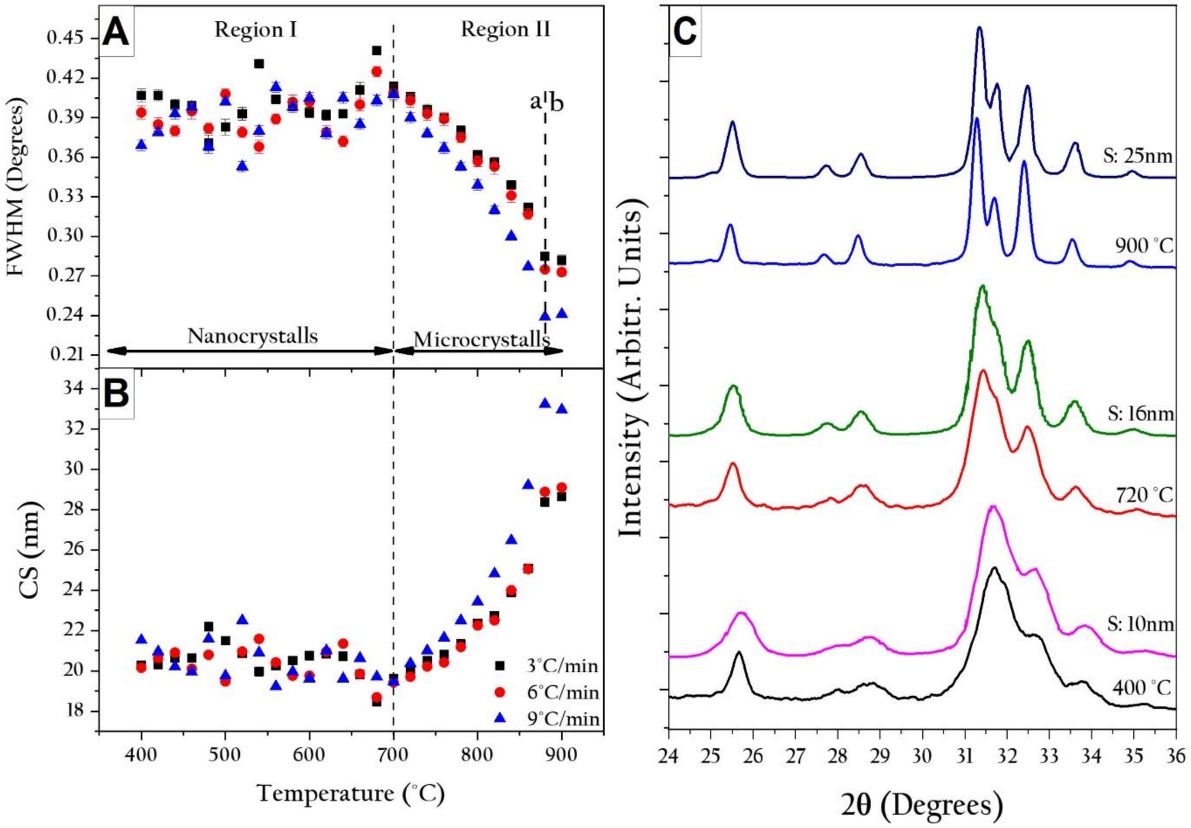

Figure 8. 5 (A) FWHM of (002) peak for all *in situ* HT-XRD patterns from 400 to 900 °C at 3, 6, and 9 °C/min. (B) Changes in the crystal size of the HAp calcinated from 400 to 900 °C at 3, 6, and 9 °C/min obtained by the Scherrer equation. (C) X-ray diffraction patterns for samples calcined at 400, 720, and 900 °C at 6 °C/min as well as simulated patterns using PDF-4 Software.

8.5. Thermal characterization

Bone is a composite material that is made up of organic and inorganic phases. Figure 8.6 exhibits the thermal behavior of defatted and deproteinized bone powder during a calcination process from room temperature to 900°C. Figure 8.6 A shows the DSC curve and its second derivative and Figure 8.6 B exhibits the TGA curve and its second derivative. The organic phase is the first one that disappears during any heating process at elevated temperatures. First, adsorbed water is lost, and it is observed as an endothermic process that starts at 55 °C and finishes at 105 °C in the DSC curve and represents 4.33% mass loss in the TGA curve. After that, lattice water and all organic material (fat and protein) remnant in the sample are degraded until 540°C in three steps according to TGA curve: fat and lattice water (105-245°C), collagen denaturation (245-353°C), and collagen degradation (353-512°C). These findings are in accordance with the reported in the literature (Ramanathan *et al.*, 2014). Moreover, the mass loss for this section (18.15%) is lower than that reported by Lozano *et al.* (2003) (30-35%), and Londoño-Restrepo *et al.*, (2016) (21.11%), which indicates that our cleaning process is more efficient to remove fat and protein. It has been also reported that its combustion produces emissions of CO_2, CN, SO_2, and NO_2 from 300 to 550 °C (Etok *et al.*, 2007). For this work, only the thermal changes that happen above 540

°C are of interest to understand transformations due to the mineral phase of the bone. From 540 to 900 °C, four endothermic events were found within the following ranges of temperature each one: 540-613°C, 613-725°C, 725-813°C, and 813-875°C. The first thermal event is related to the surface coalesce; the second one is the crystallization of the nano-hydroxyapatite. The third peak is due to a second coalescence and crystallization of microcrystals. Finally, carbonate lost happens.

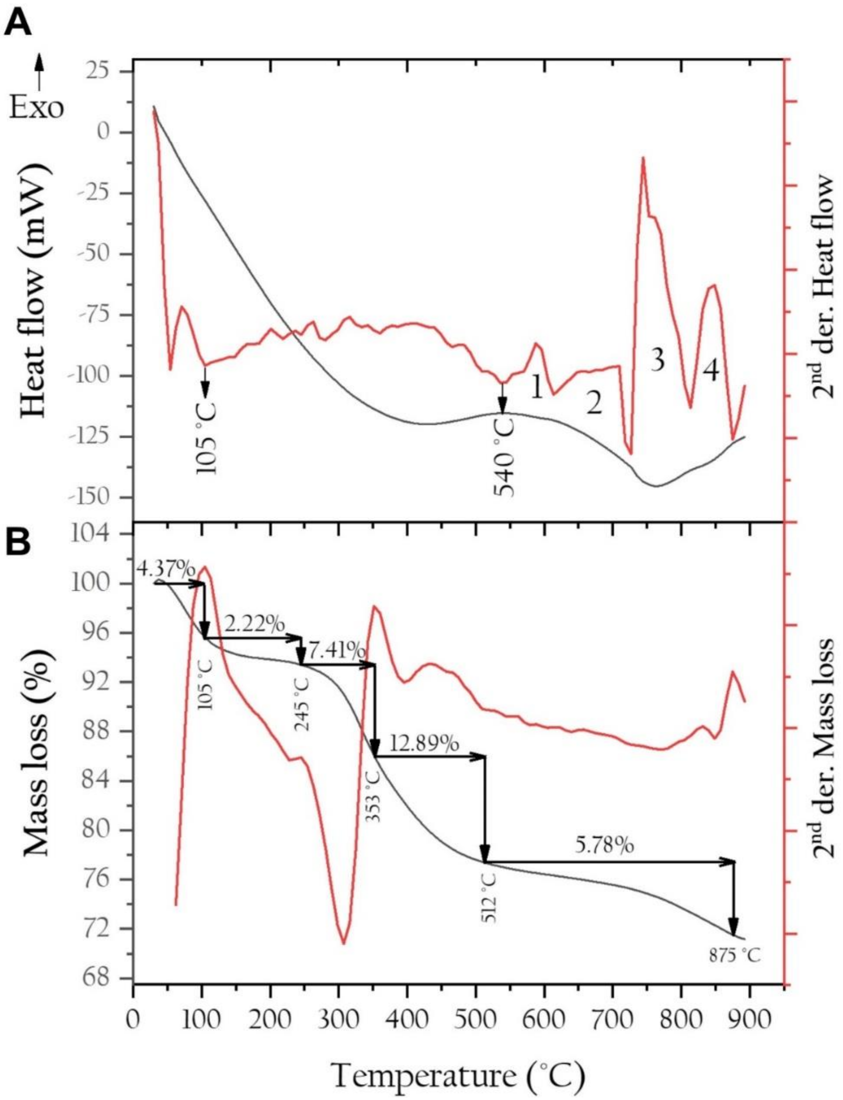

Figure 8. 6 (A) DSC thermogram and (B) TGA curve for cleaned bovine bone powder carried out at 9 °C/min.

8.6. Discussion

As has been shown in previous chapters, mineral content and Ca/P atomic ratio do not change as a function of the temperature. Increases of these values as shown in Table 8.1 corresponds to a concentration effect in which the organic phase removal produces an apparent increase of all minerals. However, the S decrease after calcination indicates that it is mainly present in the organic matrix. It means, the decrease of the S content is due to collagen and non-collagen proteins are the primary sources of that element in mammalian bones, and they are degraded below 700 °C. It is worth highlighting that at the testing temperature and heating rate do not affect the mineral content for the samples calcined up 900 °C. All these minerals play significant role in bone regeneration because of their ability to induce a biological response for bone remodeling (Barrère *et al.*, 2006). As it is well known, the values for minerals found in this work, of course, can change as a result of the diet, age, sex, among others (Aguilera-Barreiro *et al.*, 2013).

The study of bone morphology is fundamental for bone tissue engineering because, for clinical purposes, any HAp must-have properties close to those belonging to the mineral phase of the host bone tissue as crystal size, morphology, and structure (Londoño-Restrepo *et al.*, 2019a). For example, the alignment of HAp nano-crystals in *c*-direction can obey to physiological requirements to improve the mechanical properties of the bone, but this arrangement is lost after the milling process; however, the porosity is not completely lost. According to Londoño-Restrepo *et al.* (2019b), bovine cortical bone has three kinds of porosities based on their size and function: primary, secondary, and tertiary. Haversian and Volkmann canals give bone primary porosity or vascular porosity (VP). Secondary porosity or lacunar-canalicular porosity (LCP) is referred to osteocyte lacunae where bone cells are accommodated into the bone, and canaliculi throughout osteocytes are communicated with blood vessels for the diffusion of oxygen, nutrients, extracellular fluids, and expelling cellular waste. Finally, tertiary porosity is due to the arrangement of hydroxyapatite crystals in collagen gaps, and it is known as collagen-apatite porosity (CAP). Until now, there is no material that has been able to emulate all this complex porous system. Here, it is very important to recall that during a thermal process, that involves elevated temperatures, hydroxyapatite nanocrystals can easily change their size, shape, and quality because of their large surface area and reactive surface (Weber Jr *et al.*, 1992; Penn & Banfield, 1999; Bailliez & Nzihou, 2004).

Calcination process provides enough energy to the sample not only to remove the organic phase, but also to grows hydroxyapatite crystals by coalescence phenomena. It is noteworthy that this coalescence does not involve crystal melting, which is near to 1500 °C for hydroxyapatite. Non-calcined hydroxyapatite crystals are randomly located, but they use the thermal energy to align themselves, as can be seen in Figure 8.2 I, and then surface coalescence happened between adjacent crystals which form areas of contact then, few crystals become into elongated and faceted crystals. This cyclic behavior conducts to micron faceted crystals as which are observed for 720°C (Figure 8.2 M). Here, it is worth noting that from 720 °C all samples have lost the tertiary porosity, which is naturally present in mammalian bones and necessary for blood irrigation and vascularization, because of the densification of the material. Thus, these BIO-HAp are not suitable for medical applications as guided bone regeneration, which does not mean that they cannot be used for further applications.

Bone grafts aim to promote bone regeneration inducing the normal bone remodeling process, it means that the material should be broken down by bone cells to create new bone. The speed of this process depends on the phase composition. Formation of other phases as is commonly reported in the literature (Shih *et al.*, 2006) was not found in this work, which could be due to this event happens during the cooling step in which the sample is more in touch with air (Ramirez-

Gutierrez *et al.*, 2016). Another factor that can promote the presence of other phases is an unsuitable sample pre-cleaning process before calcination since, as it was demonstrated, the organic phase has minerals that can react to form undesirable products (Londoño-Restrepo *et al.*, 2018).

Unfortunately, hydroxyapatite without organic phase does not have enough mechanical properties to be used directly as large bone substitute pieces. This is why metal prosthesis is needed, but they need coating with materials that avoid oxidation like hydroxyapatite. Coating process involves high temperatures in which not only metal material structure is expanded, but also the coating material. In Table 8.2, it is possible to see that the higher heating rate, the higher the lattice parameter. The increment of these lattice parameters as a function of the temperature and the heating rate revealed higher values than those reported by Nakamura *et al.* (1990) which carried out X-ray diffraction patterns on synthetic hydroxyapatite from 25 to 1150 °C every 50 °C at 10 °C/min. The heating rate directly influences the lattice parameter, but despite their higher heating rate, a and c values reported in this work were higher. Again, this fact may obey to the presence of mineral traces in hydroxyapatite from bovine bone as revealed ICP. Even though linear TEC values for bovine hydroxyapatite could result in higher values above 900 °C, it is not recommended reaching these temperatures because of the dehydroxylation of hydroxyapatite (Londoño-Restrepo *et al.*, 2018).

As mentioned before, BIO-HAp crystals exhibit ordered atomic arrangement although the presence of the mineral traces. For that reason, broad XRD peaks are not originated by poorly crystalline quality as reported (Gamsjaeger *et al.*, 2011). Moreover, dark-field HR-TEM image demonstrated the nanocrystalline character of bovine BIO-HAp, and elastic and inelastic scattering signals reach the detector in the case of nanocrystals, thus X-ray peaks become wider. Thus, FWHM cannot be used as an order parameter to determine only the contribution of the crystalline quality to the peak width.

According to Figure 8.5 B, the maximum crystallite size is close to 33 nm, although, SEM images demonstrate the micrometric size of BIO-HAp crystals after 720 °C (Figure 8.2). This is due to Scherrer equation is limited to crystal sizes from 100 to 200 nm, thus, calculating crystal sizes smaller than this range has the problem of separating the peak broadening due to the crystallite size from other factors as inelastic scattering (Londoño-Restrepo *et al.*, 2019a; Holzwarth & Gibson, 2011). Shih *et al.* (2006) calculated the crystallite size of hydroxyapatite powder synthesized at 75 °C and heated from 25 to 400-1500 °C and reported an increasing trend from 31 to 48 nm; this last crystallite size value was reached for sample heated over 700 °C. However, it is clear that hydroxyapatite reaches higher crystallite sizes after calcination at high temperatures as was demonstrated by SEM. Recently, Londoño-Restrepo *et al.*, (2019a) proved that hydroxyapatite crystals from bovine bone are not only well-ordered but also nanometric which is the reason why patterns for this kind of sample exhibits broad peaks that become narrower when crystals are in the micrometric scale. To sum up, the decreasing of the FWHM values is mainly due to crystal growth instead of a crystalline quality improving.

Endothermic peaks are connected to events that require energy to happen. After all organic material has been removed, hydroxyapatite crystals use the energy provided to grown; thus, the first thermal event is related to the surface coalesce as mentioned earlier in which these crystals remain as nanocrystals as can be observed in Figure 8.2 (D-H) and that is also supported by their broad X-ray peaks which are characteristic of nanometric crystals. The second thermal event is due to the crystallization of the nano-hydroxyapatite that are aligned until becoming shapes as hexagonal bars (see Figure 8.2 (I-M)). This structural event is clearly shown as a sharp FWHM decrease in Figure 8.5 A and represents the tough transition from nano to micro sizes. The third event is related to a second coalescence and crystallization of microcrystals (see Figure 8.2 (N-R)). Again, this event is evident in the X-ray diffraction patterns but now as a FWHM decrease. Finally, the fourth event (813-875 °C), is due to carbonate loss. All these events are closely related to TEC findings.

8.6. Conclusions

Hydroxyapatite from bovine bone powder is composed by ordered crystalline nanoplates which exhibit broad diffracted peaks according to HR-TEM and XRD characterizations. This means that crystalline nano-hydroxyapatite produce these peaks from inelastic X-ray scattering originated by nanocrystals whose behavior is like diffraction centers instead of poor crystalline quality as is commonly reported. This indicates the existence of a multistep process governed by coalescence phenomena as demonstrated by HR-SEM images.

Crystal structure of synthetic HAp has been described and accepted by ICDD as a hexagonal or monoclinic structure. However, due to ion inclusions in the HAp molecule, it is necessary to properly define the structure of bovine HAp.

Decreasing FWHM of the X-ray patterns from broad to narrow peaks after the sample reaches 700 °C for all heating rates, confirms SEM observations. This finding is also supported by the shape of the patterns displayed by PDF-4 software for synthetic hydroxyapatite with different crystallite sizes.

Thermal expansion is a not linear function of the temperature that shows increase in the lattice volume; theoretical calculations of this property may open a new window to further understand coalescence phenomena in this material.

To avoid nano to micro thermal transition; bovine HAp should not be calcinated up to 700 °C.

Further analysis is necessary to determine whether carbonate and substitutional ions in the hydroxyapatite lattice promotes higher thermal expansion.

CHAPTER 9

CONCLUSIONS

- Calcination process no only produce organic phase removal but also crystal growth. For all studied heating rates, there is a limit of temperature (700 °C) in which physicochemical properties of HAp change. Moreover, incineration above 700 °C also promotes formation of other phases as MgO.
- Trabecular bone exhibits a complex architecture with three kinds of porosities that must be take into account for designing and fabrication of artificial scaffolds.
- HR-TEM and HR-SEM demonstrated that the mineral phase of bovine bone is composed by nano-crystalline hydroxyapatite like plates that are aligned in *c*-direction. These characteristics makes that its X-ray diffraction patterns exhibits broad peaks instead of narrow ones –as is common in crystalline materials.
- The Raman and IR broad bands found in raw samples are related to the nano size of the crystals and not to the low crystalline quality while the narrow bands correspond to the increase of the crystal size, bulk and surface phonon states govern the width of the bands. Thus, the calculation of crystalline quality in the nanocrystals using the FWHM of Raman, IR, and X-ray cannot be related to crystalline quality in the case of nano hydroxyapatite.
- Scherrer equation cannot be used to determine the crystal size for samples calcined above 700 °C.
- Tissue engineering has established some requirements for bone replacing materials such as biocompatibility, biodegradability, and mechanical properties; however, it is concluded that nanometric sizes and hierarchical porosities must be included in these requisites.
- Calcination process involves several changes in hydroxyapatite; therefore, choosing the thermal profile of the process is imperative to guarantee the complete organic phase

removal but avoiding the loss of tertiary porosity because of crystal growth and morphological changes. Although calcinations until 1400 °C are commonly reported, the dehydroxylation process starts around 900 °C, in which hydroxyapatite turns into a mix of calcium phosphates; thus, it is not recommended reaching that temperatures. Even though calcination at 900 °C assures complete phase removal, at this temperature, tertiary porosity is lost and MgO is formed; thus, this temperature is neither recommended. There is a narrow range of temperatures in which there is only hydroxyapatite and its tertiary porosity is still present: 540-700 °C.

- Thermal expansion is a not linear function of the temperature that shows increase in the lattice volume; theoretical calculations of this property may open a new window to further understand coalescence phenomena in this material.

BIBLIOGRAPHY

Aarthy, S., Thenmuhil, D., Dharunya, G., & Manohar, P. (2019). Exploring the effect of sintering temperature on naturally derived hydroxyapatite for bio-medical applications. Journal of Materials Science: Materials in Medicine, 30(2), 21.

Abdulkareem, E. H., Memarzadeh, K., Allaker, R. P., Huang, J., Pratten, J., & Spratt, D. (2015). Anti-biofilm activity of zinc oxide and hydroxyapatite nanoparticles as dental implant coating materials. Journal of dentistry, 43(12), 1462-1469.

Aguilera-Barreiro, M. D. L. A., Rivera-Márquez, J. A., Trujillo-Arriaga, H. M., Tamayo y Orozco, J. A., Barreira-Mercado, E., & Rodríguez-García, M. E. (2013). Intake of dehydrated nopal (Opuntia ficus indica) improves bone mineral density and calciuria in adult Mexican women. Food & nutrition research, 57(1), 19106-19120.

Akram, M., et al. (2014). Extracting hydroxyapatite and its precursors from natural resources. Journal of Materials Science, 49(4), 1461-1475.

Aldazábal Martínez, C., Refulio Zelada, Z., & Huamaní Mamani, J. O. (2013). Regeneración ósea guiada para implantes dentales posexodoncia.

Andrés, N. C., et al. (2017). Manipulation of Mg2+–Ca2+ switch on the development of bone mimetic hydroxyapatite. ACS applied materials & interfaces, 9(18), 15698-15710.

Aquilano, D., Bruno, M., Rubbo, M., Massaro, F. R., & Pastero, L. (2014). Low symmetry polymorph of hydroxyapatite. Theoretical equilibrium morphology of the monoclinic Ca5 (OH)(PO4) 3. Crystal Growth & Design, 14(6), 2846-2852.

Awonusi, A., Morris, M. D., & Tecklenburg, M. M. (2007). Carbonate assignment and calibration in the Raman spectrum of apatite. Calcified tissue international, 81(1), 46-52.

Bae, W. C., Chen, P. C., Chung, C. B., Masuda, K., D'Lima, D., & Du, J. (2012). Quantitative ultrashort echo time (UTE) MRI of human cortical bone: correlation with porosity and biomechanical properties. Journal of Bone and Mineral Research, 27(4), 848-857.

Bahrololoom, M. E., Javidi, M., Javadpour, S., & Ma, J. (2009). Characterisation of natural hydroxyapatite extracted from bovine cortical bone ash. J. Ceram. Process. Res, 10(2), 129-138.

Bailliez, S., & Nzihou, A. (2004). The kinetics of surface area reduction during isothermal sintering of hydroxyapatite adsorbent. Chemical Engineering Journal, 98(1-2), 141-152.

Bala, Y., Depalle, B., Douillard, T., Meille, S., Clément, P., Follet, H., ... & Boivin, G. (2011). Respective roles of organic and mineral components of human cortical bone matrix in micromechanical behavior: an instrumented indentation study. Journal of the mechanical behavior of biomedical materials, 4(7), 1473-1482.

Barakat, N. A., Khil, M. S., Omran, A. M., Sheikh, F. A., & Kim, H. Y. (2009). Extraction of pure natural hydroxyapatite from the bovine bones bio waste by three different methods. Journal of materials processing technology, 209(7), 3408-3415.

Barrère, F., van Blitterswijk, C. A., & de Groot, K. (2006). Bone regeneration: molecular and cellular interactions with calcium phosphate ceramics. International journal of nanomedicine, 1(3), 317.

Behari, J., (2009). Elements of Bone Biophysics, in Biophysical Bone Behavior: Principles and Applications, John Wiley & Sons, Ltd, Chichester, UK.

Bose, S., Roy, M., & Bandyopadhyay, A. (2012). Recent advances in bone tissue engineering scaffolds. Trends in biotechnology, 30(10), 546-554.

Boskey, A. (2003). Bone mineral crystal size. Osteoporosis international, 14(5), 16-21.

Boskey, A.L., (2004). The Organic and Inorganic Matrices, in Bone Tissue Engineering, CRC Press, LLC, Florida, EE.UU.

Britz, H. M., Jokihaara, J., Leppänen, O. V., Järvinen, T., & Cooper, D. M. L. (2010). 3D visualization and quantification of rat cortical bone porosity using a desktop micro-CT system: a case study in the tibia. Journal of microscopy, 240(1), 32-37.

Brzezińska-Miecznik, J., Haberko, K., Sitarz, M., Bućko, M. M., & Macherzyńska, B. (2015). Hydroxyapatite from animal bones–Extraction and properties. Ceramics International, 41(3), 4841-4846.

Campa Molina J., et al., (2007). Biomateriales: Fundamentos, técnicas y aplicaciones. Universidad de Guadalajara, México.

Cardoso, L., Fritton, S. P., Gailani, G., Benalla, M., & Cowin, S. C. (2013). Advances in assessment of bone porosity, permeability and interstitial fluid flow. Journal of biomechanics, 46(2), 253-265.

Clark, P., Denova-Gutiérrez, E., Razo, C., Rios-Blancas, M. J., & Lozano, R. (2018). The burden of musculoskeletal disorders in Mexico at national and state level, 1990–2016: estimates from the global burden of disease study 2016. Osteoporosis International, 29(12), 2745-2760.

Crane, N. J., Popescu, V., Morris, M. D., Steenhuis, P., & Ignelzi Jr, M. A. (2006). Raman spectroscopic evidence for octacalcium phosphate and other transient mineral species deposited during intramembranous mineralization. Bone, 39(3), 434-442.

Cullity, B.D. Stock, S.R. Elements of X-ray Diffraction, (third ed.), New York (Prentice Hall, 2001).

Czerniczyniec, M., Farías, S., Magallanes, J., & Cicerone, D. (2007). Arsenic (V) adsorption onto biogenic hydroxyapatite: solution composition effects. Water, air, and soil pollution, 180(1-4), 75-82.

De Mul, F. F. M., Otto, C., Greve, J., Arends, J., & Ten Bosch, J. J. (1988). Calculation of the Raman line broadening on carbonation in synthetic hydroxyapatite. Journal of Raman spectroscopy, 19(1), 13-21.

Degirmenbasi, N., Kalyon, D. M., & Birinci, E. (2006). Biocomposites of nanohydroxyapatite with collagen and poly (vinyl alcohol). Colloids and Surfaces B: Biointerfaces, 48(1), 42-49.

Diaz, E.M. (1996). Osteocalcina: Evaluación de diferentes ensayos utilizados para su medida. Aplicación al estudio de las formas inmunorreactivas presentes en el medio de cultivo de osteoblastos humanos y circulantes en suero. Tesis doctoral. Universidad complutense de Madrid, España.

Doğan, İ., & van de Sanden, M. C. (2013). Direct characterization of nanocrystal size distribution using Raman spectroscopy. Journal of Applied Physics, 114(13), 134310.

Ehbrecht, M., Ferkel, H., Huisken, F., Holz, L., Polivanov, Y. N., Smirnov, V. V., ... & Schmidt, R. (1995). Deposition and analysis of silicon clusters generated by laser-induced gas phase reaction. Journal of applied physics, 78(9), 5302-5306.

Ehbrecht, M., Kohn, B., Huisken, F., Laguna, M. A., & Paillard, V. (1997). Photoluminescence and resonant Raman spectra of silicon films produced by size-selected cluster beam deposition. Physical Review B, 56(11), 6958.

Elliott, J. C. (2013). Structure and chemistry of the apatites and other calcium orthophosphates (Vol. 18). Elsevier.

Eslami, N., Mahmoodian, R., Hamdi, M., Khatir, N. M., Herliansyah, M. K., & Rafieerad, A. R. (2017). Study the synthesis, characterization and immersion of dense and porous bovine hydroxyapatite structures in Hank's balanced salt solution. JOM, 69(4), 691-698.

Etok, S. E., Valsami-Jones, E., Wess, T. J., Hiller, J. C., Maxwell, C. A., Rogers, K. D., ... & Buckley, M. (2007). Structural and chemical changes of thermally treated bone apatite. Journal of Materials Science, 42(23), 9807-9816.

Faber, J., & Fawcett, T. (2002). The powder diffraction file: present and future. Acta Crystallographica Section B: Structural Science, 58(3), 325-332.

Feldkamp, L. A., Davis, L. C., & Kress, J. W. (1984). Practical cone-beam algorithm. Josa a, 1(6), 612-619.

Figueiredo, M., Fernando, A., Martins, G., Freitas, J., Judas, F., & Figueiredo, H. (2010). Effect of the calcination temperature on the composition and microstructure of hydroxyapatite derived from human and animal bone. Ceramics international, 36(8), 2383-2393.

Fihri, A., Len, C., Varma, R. S., & Solhy, A. (2017). Hydroxyapatite: A review of syntheses, structure and applications in heterogeneous catalysis. Coordination Chemistry Reviews, 347, 48-76.

Fischer, G. R., Bardhan, P., & Geiger, J. E. (1983). The lattice thermal expansion of hydroxyapatite. Journal of materials science letters, 2(10), 577-578.

France, C. A., Thomas, D. B., Doney, C. R., & Madden, O. (2014). FT-Raman spectroscopy as a method for screening collagen diagenesis in bone. Journal of archaeological Science, 42, 346-355.

Fratzl, P., Gupta, H. S., Paschalis, E. P., & Roschger, P. (2004). Structure and mechanical quality of the collagen–mineral nano-composite in bone. Journal of materials chemistry, 14(14), 2115-2123.

Freeman, J. J., Wopenka, B., Silva, M. J., & Pasteris, J. D. (2001). Raman spectroscopic detection of changes in bioapatite in mouse femora as a function of age and in vitro fluoride treatment. Calcified Tissue International, 68(3), 156-162.

Gamsjaeger, S., Buchinger, B., Zwettler, E., Recker, R., Black, D., Gasser, J. A., ... & Paschalis, E. P. (2011). Bone material properties in actively bone-forming trabeculae in postmenopausal women with osteoporosis after three years of treatment with once-yearly zoledronic acid. Journal of Bone and Mineral Research, 26(1), 12-18.

Gao, Y., Zhao, X., Yin, P., & Gao, F. (2016). Size-dependent Raman shifts for nanocrystals. Scientific reports, 6, 20539.

Gerhardt, L. C., Jell, G. M. R., & Boccaccini, A. R. (2007). Titanium dioxide (TiO_2) nanoparticles filled poly (D, L lactid acid)(PDLLA) matrix composites for bone tissue engineering. Journal of Materials Science: Materials in Medicine, 18(7), 1287-1298.

Giesen, E. B. W., Ding, M., Dalstra, M., & Van Eijden, T. M. G. J. (2001). Mechanical properties of cancellous bone in the human mandibular condyle are anisotropic. Journal of biomechanics, 34(6), 799-803.

Giraldo-Betancur, A. L., Espinosa-Arbelaez, D. G., del Real-López, A., Millan-Malo, B. M., Rivera-Muñoz, E. M., Gutierrez-Cortez, E., ... & Rodriguez-García, M. E. (2013). Comparison of physicochemical properties of bio and commercial hydroxyapatite. Current Applied Physics, 13(7), 1383-1390.

Glimcher, M. J. (2006). Bone: nature of the calcium phosphate crystals and cellular, structural, and physical chemical mechanisms in their formation. Reviews in mineralogy and geochemistry, 64(1), 223-282.

Goller, G., Oktar, F. N., Agathopoulos, S., Tulyaganov, D. U., Ferreira, J. M. F., Kayali, E. S., & Peker, I. (2006). Effect of sintering temperature on mechanical and microstructural properties of bovine hydroxyapatite (BHA). Journal of sol-gel science and technology, 37(2), 111-115.

Gómez Ortega, J. L., & Elizondo Villarreal, N. (2004). Visualización cristalografica de la hidroxiapatita. Ingenierías, 7(24), 46-50.

Gong, B., & Morris, M. D. (2015). Raman spectroscopy monitors adverse bone sequelae of cancer radiotherapy. Chinese Chemical Letters, 26(4), 401-406.

Gouadec, G., & Colomban, P. (2007). Raman Spectroscopy of nanomaterials: How spectra relate to disorder, particle size and mechanical properties. Progress in crystal growth and characterization of materials, 53(1), 1-56.

Gross, K. A., & Berndt, C. C. (1998). Thermal processing of hydroxyapatite for coating production. Journal of Biomedical Materials Research, 39(4), 580-587.

Haberko, K., Bućko, M. M., Brzezińska-Miecznik, J., Haberko, M., Mozgawa, W., Panz, T., ... & Zarębski, J. (2006). Natural hydroxyapatite—its behaviour during heat treatment. Journal of the European Ceramic Society, 26(4-5), 537-542.

Haberko, K., Bućko, M. M., Mozgawa, W., Pyda, A., Brzezińska-Miecznik, J., & Carpentier, J. (2009). Behaviour of bone origin hydroxyapatite at elevated temperatures and in O_2 and CO_2 atmospheres. Ceramics International, 35(6), 2537-2540.

Hammood, A. S., Hassan, S. S., & Alkhafagy, M. T. (2017). Access to optimal calcination temperature for nanoparticles synthesis from hydroxyapatite bovine femur bone waste. Nano Biomedicine Engineering, 3(9), 228-235.

Heinl, P., Müller, L., Körner, C., Singer, R. F., & Müller, F. A. (2008). Cellular Ti–6Al–4V structures with interconnected macro porosity for bone implants fabricated by selective electron beam melting. Acta biomaterialia, 4(5), 1536-1544.

Heredia, A., Colin-Garcia, M., Peña-Rico, M. A., Beltrán, L. F. A., Grácio, J., Contreras-Torres, F. F., ... & Basiuk, V. A. (2013). Thermal, infrared spectroscopy and molecular modeling characterization of bone: An insight in the apatite-collagen type I interaction. Advances in Biological Chemistry, 3(02), 215.

Herliansyah, M. K., Hamdi, M., Ide-Ektessabi, A., Wildan, M. W., & Toque, J. A. (2009). The influence of sintering temperature on the properties of compacted bovine hydroxyapatite. Materials Science and Engineering: C, 29(5), 1674-1680.

Hickey, D. J., Ercan, B., Sun, L., & Webster, T. J. (2015). Adding MgO nanoparticles to hydroxyapatite–PLLA nanocomposites for improved bone tissue engineering applications. Acta biomaterialia, 14, 175-184.

Hoang, Q. Q., Sicheri, F., Howard, A. J., & Yang, D. S. (2003). Bone recognition mechanism of porcine osteocalcin from crystal structure. Nature, 425(6961), 977.

Holzwarth, U., & Gibson, N. (2011). The Scherrer equation versus the'Debye-Scherrer equation'. Nature nanotechnology, 6(9), 534.

Ishikawa, K., Ducheyne, P., & Radin, S. (1993). Determination of the Ca/P ratio in calcium-deficient hydroxyapatite using X-ray diffraction analysis. Journal of Materials Science: Materials in Medicine, 4(2), 165-168.

Ivanova, T. I., Frank-Kamenetskaya, O. V., Kol'tsov, A. B., & Ugolkov, V. L. (2001). Crystal structure of calcium-deficient carbonated hydroxyapatite. Thermal decomposition. Journal of Solid State Chemistry, 160(2), 340-349.

Jaber, H. L., Hammood, A. S., & Parvin, N. (2018). Synthesis and characterization of hydroxyapatite powder from natural Camelus bone. Journal of the Australian Ceramic Society, 54(1), 1-10.

Joschek, S., Nies, B., Krotz, R., & Göpferich, A. (2000). Chemical and physicochemical characterization of porous hydroxyapatite ceramics made of natural bone. Biomaterials, 21(16), 1645-1658.

Kabekkodu, S. N., Faber, J., & Fawcett, T. (2002). New Powder Diffraction File (PDF-4) in relational database format: advantages and data-mining capabilities. Acta Crystallographica Section B: Structural Science, 58(3), 333-337.

Kebiroglu, M. H., Orek, C., Bulut, N., Kaygili, O., Keser, S., & Ates, T. (2017). Temperature dependent structural and vibrational properties of hydroxyapatite: A theoretical and experimental study. Ceramics International, 43(17), 15899-15904.

Khoo, W., Nor, F. M., Ardhyananta, H., & Kurniawan, D. (2015). Preparation of natural hydroxyapatite from bovine femur bones using calcination at various temperatures. Procedia Manufacturing, 2, 196-201.

Kim, S. H., Shin, J. W., Park, S. A., Kim, Y. K., Park, M. S., Mok, J. M., ... & Lee, J. W. (2004). Chemical, structural properties, and osteoconductive effectiveness of bone block derived from porcine cancellous bone. Journal of Biomedical Materials Research Part B: Applied Biomaterials, 68(1), 69-74.

Kumar, G. S., Karunakaran, G., Girija, E. K., Kolesnikov, E., Van Minh, N., Gorshenkov, M. V., & Kuznetsov, D. (2018). Size and morphology-controlled synthesis of mesoporous hydroxyapatite nanocrystals by microwave-assisted hydrothermal method. Ceramics International, 44(10), 11257-11264.

Kusrini, E., & Sontang, M. (2012). Characterization of x-ray diffraction and electron spin resonance: Effects of sintering time and temperature on bovine hydroxyapatite. Radiation Physics and Chemistry, 81(2), 118-125.

Laven, P. (2010). Separating diffraction from scattering: the million-dollar challenge. Journal of Nanophotonics, 4(1), 041593.

LeGeros, R. Z. (2002). Properties of osteoconductive biomaterials: calcium phosphates. Clinical Orthopaedics and Related Research (1976-2007), 395, 81-98.

Li, G. H., Ding, K., Chen, Y., Han, H. X., & Wang, Z. P. (2000). Photoluminescence and Raman scattering of silicon nanocrystals prepared by silicon ion implantion into SiO_2 films. Journal of Applied Physics, 88(3), 1439-1442.

Li, Z., Thompson, B. C., Dong, Z., & Khor, K. A. (2016). Optical and biological properties of transparent nanocrystalline hydroxyapatite obtained through spark plasma sintering. Materials Science and Engineering: C, 69, 956-966.

Lin, Z., Hu, R., Zhou, J., Ye, Y., Xu, Z., & Lin, C. (2017). A further insight into the adsorption mechanism of protein on hydroxyapatite by FTIR-ATR spectrometry. Spectrochimica Acta Part A: Molecular and Biomolecular Spectroscopy, 173, 527-531.

Lindahl, O. (1976). Mechanical properties of dried defatted spongy bone. Acta Orthopaedica Scandinavica, 47(1), 11-19.

Londoño-Restrepo, S. M., Jeronimo-Cruz, R., Millán-Malo, B. M., Rivera-Muñoz, E. M., & Rodriguez-García, M. E. (2019a). Effect of the Nano Crystal Size on the X-ray Diffraction Patterns of Biogenic Hydroxyapatite from Human, Bovine, and Porcine Bones. Scientific reports, 9(1), 5915.

Londoño-Restrepo, S. M., Jeronimo-Cruz, R., Rubio-Rosas, E., & Rodriguez-García, M. E. (2018). The effect of cyclic heat treatment on the physicochemical properties of bio hydroxyapatite from bovine bone. Journal of Materials Science: Materials in Medicine, 29(5), 52.

Londoño-Restrepo, S. M., Ramirez-Gutierrez, C. F., del Real, A., Rubio-Rosas, E., & Rodriguez-García, M. E. (2016). Study of bovine hydroxyapatite obtained by calcination at low heating rates and cooled in furnace air. Journal of materials science, 51(9), 4431-4441.

Londoño-Restrepo, S. M., Ramirez-Gutierrez, C. F., Villarraga-Gómez, H., & Rodriguez-García, M. E. (2019b). Study of microstructural, structural, mechanical, and vibrational properties of defatted trabecular bovine bones: natural sponges. In Materials for Biomedical Engineering (pp. 441-485). Elsevier.

Lozano, L. F., Pena-Rico, M. A., Heredia, A., Ocotlan-Flores, J., Gomez-Cortes, A., Velazquez, R., ... & Bucio, L. (2003). Thermal analysis study of human bone. Journal of materials science, 38(23), 4777-4782.

Maiti, N. C., Apetri, M. M., Zagorski, M. G., Carey, P. R., & Anderson, V. E. (2004). Raman spectroscopic characterization of secondary structure in natively unfolded proteins: α-synuclein. Journal of the American Chemical Society, 126(8), 2399-2408.

Mandair, G. S., & Morris, M. D. (2015). Contributions of Raman spectroscopy to the understanding of bone strength. BoneKEy reports, 4.

Matsunaga, K., & Murata, H. (2009). Formation energies of substitutional sodium and potassium in hydroxyapatite. Materials transactions, 0902090667-0902090667.

Méndez-Lozano, N., Velázquez-Castillo, R., Rivera-Muñoz, E. M., Bucio-Galindo, L., Mondragón-Galicia, G., Manzano-Ramírez, A., ... & Apátiga-Castro, L. M. (2017). Crystal growth and structural analysis of hydroxyapatite nanofibers synthesized by the hydrothermal microwave-assisted method. Ceramics International, 43(1), 451-457.

Meneghini, C., Dalconi, M. C., Nuzzo, S., Mobilio, S., & Wenk, R. H. (2003). Rietveld refinement on X-ray diffraction patterns of bioapatite in human fetal bones. Biophysical journal, 84(3), 2021-2029.

Miranda, M. A. R., & Sasaki, J. M. (2018). The limit of application of the Scherrer equation. Acta Crystallographica Section A: Foundations and Advances, 74(1), 54-65.

Monshi, A., Foroughi, M. R., & Monshi, M. R. (2012). Modified Scherrer equation to estimate more accurately nano-crystallite size using XRD. World journal of nano science and engineering, 2(3), 154-160.

Morris, M. D., & Mandair, G. S. (2011). Raman assessment of bone quality. Clinical Orthopaedics and Related Research®, 469(8), 2160-2169.

Movasaghi, Z., Rehman, S., Rehman, I.U., (2007). Raman spectroscopy of biological tissues. Applied spectroscopy Reviews, 42(5), 493-541.

Muniz, F. T. L., Miranda, M. A. R., Morilla dos Santos, C., & Sasaki, J. M. (2016). The Scherrer equation and the dynamical theory of X-ray diffraction. Acta Crystallographica Section A: Foundations and Advances, 72(3), 385-390.

Murugan, R., & Ramakrishna, S. (2004). Bioresorbable composite bone paste using polysaccharide based nano hydroxyapatite. Biomaterials, 25(17), 3829-3835.

Nakamura, S., Otsuka, R., Aoki, H., Akao, M., Miura, N., & Yamamoto, T. (1990). Thermal expansion of hydroxyapatite-β-tricalcium phosphate ceramics. Thermochimica acta, 165(1), 57-72.

Nasiri-Tabrizi, B., Fahami, A., & Ebrahimi-Kahrizsangi, R. (2013). Effect of milling parameters on the formation of nanocrystalline hydroxyapatite using different raw materials. Ceramics International, 39(5), 5751-5763.

Nasiri-Tabrizi, B., Fahami, A., & Ebrahimi-Kahrizsangi, R. (2014). A comparative study of hydroxyapatite nanostructures produced under different milling conditions and thermal treatment of bovine bone. Journal of Industrial and Engineering Chemistry, 20(1), 245-258.

Needham, F., & Faber, J. (2003). Total pattern analysis using the new organic powder diffraction file: PDF-4/Organics. Am. Pharm. Rev., 6(4), 10-12.

Niakan, A., Ramesh, S., Ganesan, P., Tan, C. Y., Purbolaksono, J., Chandran, H., & Teng, W. D. (2015). Sintering behaviour of natural porous hydroxyapatite derived from bovine bone. Ceramics International, 41(2), 3024-3029.

Niakan, A., Ramesh, S., Naveen, S. V., Mohan, S., & Kamarul, T. (2017). Osteogenic priming potential of bovine hydroxyapatite sintered at different temperatures for tissue engineering applications. Materials Letters, 197, 83-86.

O'Brien, F. J. (2011). Biomaterials & scaffolds for tissue engineering. Materials today, 14(3), 88-95.

Olszta, M. J., Cheng, X., Jee, S. S., Kumar, R., Kim, Y. Y., Kaufman, M. J., ... & Gower, L. B. (2007). Bone structure and formation: A new perspective. Materials Science and Engineering: R: Reports, 58(3-5), 77-116.

Ooi, C. Y., Hamdi, M., & Ramesh, S. (2007). Properties of hydroxyapatite produced by annealing of bovine bone. Ceramics international, 33(7), 1171-1177.

Palacio-Mancheno, P. E., Larriera, A. I., Doty, S. B., Cardoso, L., & Fritton, S. P. (2014). 3D Assessment of Cortical Bone Porosity and Tissue Mineral Density Using High-Resolution µCT: Effects of Resolution and Threshold Method. Journal of Bone and Mineral Research, 29(1), 142-150.

Paschalis, E. P., Mendelsohn, R., & Boskey, A. L. (2011). Infrared assessment of bone quality: a review. Clinical Orthopaedics and Related Research®, 469(8), 2170-2178.

Pastero, L., Bruno, M., & Aquilano, D. (2018). Habit Change of Monoclinic Hydroxyapatite Crystals Growing from Aqueous Solution in the Presence of Citrate Ions: The Role of 2D Epitaxy. Crystals, 8(8), 308.

Patel, S., Wei, S., Han, J., & Gao, W. (2015). Transmission electron microscopy analysis of hydroxyapatite nanocrystals from cattle bones. Materials Characterization, 109, 73-78.

Penel, G., Delfosse, C., Descamps, M., & Leroy, G. (2005). Composition of bone and apatitic biomaterials as revealed by intravital Raman microspectroscopy. Bone, 36(5), 893-901.

Penn, R. L., & Banfield, J. F. (1999). Morphology development and crystal growth in nanocrystalline aggregates under hydrothermal conditions: Insights from titania. Geochimica et cosmochimica acta, 63(10), 1549-1557.

Perdok, W. G., Christoffersen, J., & Arends, J. (1987). The thermal lattice expansion of calcium hydroxyapatite. Journal of crystal growth, 80(1), 149-154.

Peters, F., Schwarz, K., & Epple, M. (2000). The structure of bone studied with synchrotron X-ray diffraction, X-ray absorption spectroscopy and thermal analysis. Thermochimica Acta, 361(1-2), 131-138.

Piga, G., Malgosa, A., Thompson, T. J. U., & Enzo, S. (2008). A new calibration of the XRD technique for the study of archaeological burned human remains. Journal of Archaeological Science, 35(8), 2171-2178.

Poumarat, G., & Squire, P. (1993). Comparison of mechanical properties of human, bovine bone and a new processed bone xenograft. Biomaterials, 14(5), 337-340.

Punnett, L., & Wegman, D. H. (2004). Work-related musculoskeletal disorders: the epidemiologic evidence and the debate. Journal of electromyography and kinesiology, 14(1), 13-23.

Querido, W., Ailavajhala, R., Padalkar, M., & Pleshko, N. (2018). Validated approaches for quantification of bone mineral crystallinity using transmission Fourier transform infrared (FT-IR), attenuated total reflection (ATR) FT-IR, and Raman Spectroscopy. Applied spectroscopy, 72(11), 1581-1593.

Ramanathan, G., Singaravelu, S., Raja, M. D., Sobhana, S. S., & Sivagnanam, U. T. (2014). Extraction and characterization of collagen from the skin of Arothron stellatus fish—A novel source of collagen for tissue engineering. Journal of Biomaterials and Tissue Engineering, 4(3), 203-209.

Ramesh, S., Loo, Z. Z., Tan, C. Y., Chew, W. K., Ching, Y. C., Tarlochan, F., ... & Sarhan, A. A. (2018). Characterization of biogenic hydroxyapatite derived from animal bones for biomedical applications. Ceramics International, 44(9), 10525-10530.

Ramirez-Gutierrez, C. F., Londoño-Restrepo, S. M., Del Real, A., Mondragón, M. A., & Rodriguez-García, M. E. (2017). Effect of the temperature and sintering time on the thermal, structural, morphological, and vibrational properties of hydroxyapatite derived from pig bone. Ceramics International, 43(10), 7552-7559.

Ramirez-Gutierrez, C. F., Mosquera-Mosquera, J. C., & Rodriguez-Garcia, M. E. (2014). Study of percolation and modeling of the order–disorder transition for zincblende–diamond structures:

Percolation and the existence of a unique band of events. Computational Condensed Matter, 1, 58-64.

Ramirez-Gutierrez, C. F., Palechor-Ocampo, A. F., Londoño-Restrepo, S. M., Millán-Malo, B. M., & Rodriguez-García, M. E. (2016). Cooling rate effects on thermal, structural, and microstructural properties of bio-hydroxyapatite obtained from bovine bone. Journal of Biomedical Materials Research Part B: Applied Biomaterials, 104(2), 339-344.

Raynaud, S., Champion, E., Bernache-Assollant, D., & Thomas, P. (2002). Calcium phosphate apatites with variable Ca/P atomic ratio I. Synthesis, characterisation and thermal stability of powders. Biomaterials, 23(4), 1065-1072.

Rendon, J. L., & Serna, C. J. (1981). IR spectra of powder hematite: effects of particle size and shape. Clay Minerals, 16(4), 375-382.

Rey, C., Marsan, O., Combes, C., Drouet, C., Grossin, D., & Sarda, S. (2014). Characterization of calcium phosphates using vibrational spectroscopies. In Advances in Calcium Phosphate Biomaterials (pp. 229-266). Springer, Berlin, Heidelberg.

Rivera-Muñoz, E. M. Hydroxyapatite-based materials: synthesis and characterization, in: R. Fazel-Rezai (Ed.), Biomedical Engineering-Frontiers and Challenges, IntechOpen, Croatia, 2011, pp. 75-98.

Rodriguez, A. G., Slichter, C. K., Acosta, F. L., Rodriguez-Soto, A. E., Burghardt, A. J., Majumdar, S., & Lotz, J. C. (2011). Human disc nucleus properties and vertebral endplate permeability. Spine, 36(7), 512.

Rujitanapanich, S., Kumpapan, P., & Wanjanoi, P. (2014). Synthesis of hydroxyapatite from oyster shell via precipitation. Energy Procedia, 56, 112-117.

Sadat-Shojai, M., Khorasani, M. T., Dinpanah-Khoshdargi, E., & Jamshidi, A. (2013). Synthesis methods for nanosized hydroxyapatite with diverse structures. Acta biomaterialia, 9(8), 7591-7621.

Samanta, A., Chanda, D. K., Das, P. S., Ghosh, J., Dey, A., Das, S., & Mukhopadhyay, A. K. (2016). Synthesis of mixed calcite–calcium oxide nanojasmine flowers. Ceramics International, 42(2), 2339-2348.

Sathyavathi, R., Saha, A., Soares, J. S., Spegazzini, N., McGee, S., Dasari, R. R., ... & Barman, I. (2015). Raman spectroscopic sensing of carbonate intercalation in breast microcalcifications at stereotactic biopsy. Scientific reports, 5, 9907.

Scardi, P. (2008). Recent advancements in Whole Powder Pattern Modelling. Zeitschrift für Kristallographie / Supplements, 27, 101-111.

Schneider, P., Meier, M., Wepf, R., & Müller, R. (2011). Serial FIB/SEM imaging for quantitative 3D assessment of the osteocyte lacuno-canalicular network. Bone, 49(2), 304-311.

Shaltout, A. A., Allam, M. A., & Moharram, M. A. (2011). FTIR spectroscopic, thermal and XRD characterization of hydroxyapatite from new natural sources. Spectrochimica Acta Part A: Molecular and Biomolecular Spectroscopy, 83(1), 56-60.

Shih, W. J., Wang, J. W., Wang, M. C., & Hon, M. H. (2006). A study on the phase transformation of the nanosized hydroxyapatite synthesized by hydrolysis using in situ high temperature X-ray diffraction. Materials Science and Engineering: C, 26(8), 1434-1438.

Siano, F., Sciammaro, L., Volpe, M. G., Mamone, G., Puppo, M. C., & Picariello, G. (2018). Integrated Analytical Methods to Characterize Lipids from Prosopis spp. and Ceratonia siliqua Seed Germ Flour. Food analytical methods, 11(12), 3471-3480.

Sirenko, A. A., Fox, J. R., Akimov, I. A., Xi, X. X., Ruvimov, S., & Liliental-Weber, Z. (2000). In situ Raman scattering studies of the amorphous and crystalline Si nanoparticles. Solid state communications, 113(10), 553-558.

Sobczak, A., Kowalski, Z., & Wzorek, Z. (2009). Preparation of hydroxyapatite from animal bones. Acta Bioeng. Biomech, 11(4), 31-36.

Sobczak-Kupiec, A., & Wzorek, Z. (2012). The influence of calcination parameters on free calcium oxide content in natural hydroxyapatite. Ceramics International, 38(1), 641-647.

Sobczak-Kupiec, A., Wzorek, Z., Kijkowska, R., & Kowalski, Z. (2013). Effect of calcination conditions of pork bone sludge on behaviour of hydroxyapatite in simulated body fluid. Bulletin of Materials Science, 36(4), 755-764.

Sofronia, A. M., Baies, R., Anghel, E. M., Marinescu, C. A., & Tanasescu, S. (2014). Thermal and structural characterization of synthetic and natural nanocrystalline hydroxyapatite. Materials Science and Engineering: C, 43, 153-163.

Suvorova, E. I., Petrenko, P. P., & Buffat, P. A. (2007). Scanning and transmission electron microscopy for evaluation of order/disorder in bone structure. Scanning: The Journal of Scanning Microscopies, 29(4), 162-170.

Swamy, V., Kuznetsov, A., Dubrovinsky, L. S., Caruso, R. A., Shchukin, D. G., & Muddle, B. C. (2005). Finite-size and pressure effects on the Raman spectrum of nanocrystalline anatase TiO_2. Physical Review B, 71(18), 184302.

Syamchand, S. S., & Sony, G. (2015). Multifunctional hydroxyapatite nanoparticles for drug delivery and multimodal molecular imaging. Microchimica Acta, 182(9-10), 1567-1589.

Szcześ, A., Yan, Y., Chibowski, E., Hołysz, L., & Banach, M. (2018). Properties of natural and synthetic hydroxyapatite and their surface free energy determined by the thin-layer wicking method. Applied Surface Science, 434, 1232-1238.

Tabor, Z. (2007). Estimating structural properties of trabecular bone from gray-level low-resolution images. Medical engineering & physics, 29(1), 110-119.

Tagaya, M., Ikoma, T., Hanagata, N., Chakarov, D., Kasemo, B., & Tanaka, J. (2010). Reusable hydroxyapatite nanocrystal sensors for protein adsorption. Science and technology of advanced materials, 11(4), 045002.

Tavakol, S., Nikpour, M. R., Amani, A., Soltani, M., Rabiee, S. M., Rezayat, S. M., ... & Jahanshahi, M. (2013). Bone regeneration based on nano-hydroxyapatite and hydroxyapatite/chitosan nanocomposites: an in vitro and in vivo comparative study. Journal of nanoparticle research, 15(1), 1373.

Thuault, A., Savary, E., Hornez, J. C., Moreau, G., Descamps, M., Marinel, S., & Leriche, A. (2014). Improvement of the hydroxyapatite mechanical properties by direct microwave sintering in single mode cavity. Journal of the European Ceramic Society, 34(7), 1865-1871.

Tommasini, S. M., Trinward, A., Acerbo, A. S., De Carlo, F., Miller, L. M., & Judex, S. (2012). Changes in intracortical microporosities induced by pharmaceutical treatment of osteoporosis as detected by high resolution micro-CT. Bone, 50(3), 596-604.

Tonsuaadu, K., Gross, K. A., Plūduma, L., & Veiderma, M. (2011). A review on the thermal stability of calcium apatites. Journal of Thermal Analysis and Calorimetry, 110(2), 647-659.

Trębacz, H., & Wójtowicz, K. (2005). Thermal stabilization of collagen molecules in bone tissue. International journal of biological macromolecules, 37(5), 257-262.

Trombe, J. C., & Montel, G. (1978). Some features of the incorporation of oxygen in different oxidation states in the apatitic lattice—I On the existence of calcium and strontium oxyapatites. Journal of Inorganic and Nuclear Chemistry, 40(1), 15-21.

Ural, A., & Vashishth, D. (2007). Effects of intracortical porosity on fracture toughness in aging human bone: a μCT-based cohesive finite element study. Journal of Biomechanical Engineering, 129(5), 625-631.

Usami, K., Xiao, K., & Okamoto, A. (2018). Efficient Ketose Production by a Hydroxyapatite Catalyst in a Continuous Flow Module. ACS Sustainable Chemistry & Engineering, 7(3), 3372-3377.

Vallet-Regi, M., & González-Calbet, J. M. (2004). Calcium phosphates as substitution of bone tissues. Progress in solid state chemistry, 32(1-2), 1-31.

Villarraga-Gómez, H., Lee, C., & Smith, S. T. (2018). Dimensional metrology with X-ray CT: A comparison with CMM measurements on internal features and compliant structures. Precision Engineering, 51, 291-307.

Wachter, N. J., Augat, P., Krischak, G. D., Sarkar, M. R., Mentzel, M., Kinzl, L., & Claes, L. (2001). Prediction of strength of cortical bone in vitro by microcomputed tomography. Clinical Biomechanics, 16(3), 252-256.

Wang, M., Wang, Q., Lu, X., Wang, K., & Ren, F. (2017). Computer simulation of ions doped hydroxyapatite: A brief review. Journal of Wuhan University of Technology-Mater. Sci. Ed., 32(4), 978-987.

Wang, X., & Ni, Q. (2003). Determination of cortical bone porosity and pore size distribution using a low field pulsed NMR approach. Journal of Orthopaedic Research, 21(2), 312-319.

Weber Jr, W. J., McGinley, P. M., & Katz, L. E. (1992). A distributed reactivity model for sorption by soils and sediments. 1. Conceptual basis and equilibrium assessments. Environmental science & technology, 26(10), 1955-1962.

Wilson, E. E., Awonusi, A., Morris, M. D., Kohn, D. H., Tecklenburg, M. M., & Beck, L. W. (2006). Three structural roles for water in bone observed by solid-state NMR. Biophysical journal, 90(10), 3722-3731.

Woodard, J. R., Hilldore, A. J., Lan, S. K., Park, C. J., Morgan, A. W., Eurell, J. A. C., ... & Johnson, A. J. W. (2007). The mechanical properties and osteoconductivity of hydroxyapatite bone scaffolds with multi-scale porosity. Biomaterials, 28(1), 45-54.

Wopenka, B., & Pasteris, J. D. (2005). A mineralogical perspective on the apatite in bone. Materials Science and Engineering: C, 25(2), 131-143.

Xin, R., Leng, Y., & Wang, N. (2010). HRTEM study of the mineral phases in human cortical bone. Advanced Engineering Materials, 12(9), B552-B557.

Zhu, G., Zhu, X., Fan, Q., & Wan, X. (2011). Raman spectra of amino acids and their aqueous solutions. Spectrochimica Acta Part A: Molecular and Biomolecular Spectroscopy, 78(3), 1187-1195.

APENDIX A

PUBLICATIONS DURING PhD STUDIES

- **PAPER I: The effect of cyclic heat treatment on the physicochemical properties of bio hydroxyapatite from bovine bone.** Journal of Materials Science: Materials in Medicine (2018) https://doi.org/10.1007/s10856-018-6061-5
- **PAPER II: Effect of the Nano Crystal Size on the X-ray Diffraction Patterns of Biogenic Hydroxyapatite from Human, Bovine, and Porcine Bones.** Scientific reports (2019) https://doi.org/10.1038/s41598-019-42269-9
- **PAPERIII: Effect of the crystal size on the infrared and Raman spectra of bio hydroxyapatite of human, bovine, and porcine bones.** Journal of Raman Spectroscopy (2019) https://doi.org/10.1002/jrs.5614
- **PAPER IV: *In situ* study of hydroxyapatite from cattle during a controlled calcination process using HT-XRD.** Materials Science and Engineering: C (2019) https://doi.org/10.1016/j.msec.2019.110020
- **CHAPTER of BOOK: Study of microstructural, structural, mechanical, and vibrational properties of defatted trabecular bovine bones: natural sponges. In: Materials for Biomedical Engineering: Hydrogels and Polymer-Based Scaffolds.** Elsevier (2019) https://doi.org/10.1016/B978-0-12-816901-8.00014-6

APENDIX B

FURTHER PUBLICATIONS

- **PAPER I: Effect of the temperature and sintering time on the thermal, structural, morphological, and vibrational properties of hydroxyapatite derived from pig bone.** Ceramics International (2017) http://dx.doi.org/10.1016/j.ceramint.2017.03.046
- **PAPER II: Morphological, structural, thermal, compositional, vibrational, and pasting characterization of white, yellow, and purple Arracacha Lego-like starches and flours (Arracacia xanthorrhiza).** International Journal of Biological Macromolecules (2018) https://doi.org/10.1016/j.ijbiomac.2018.03.021